Title

Perovskite Oxide Materials for Solar Thermochemical Hydrogen Production from Water Splitting through Chemical Looping.

Journal

ACS Catalysis, 14(19)

ISSN

2155-5435

Authors

Liu, Cijie

Park, Jiyun

De Santiago, Héctor

et al.

Publication Date

2024-10-04

DOI

10.1021/acscatal.4c03357

Peer reviewed

ACS Catalysis

pubs.acs.org/acscatalysis
Review

Perovskite Oxide Materials for Solar Thermochemical Hydrogen Production from Water Splitting through Chemical Looping

Cijie Liu, Jiyun Park, Héctor A. De Santiago, Boyuan Xu, Wei Li,* Dawei Zhang, Lingfeng Zhou, Yue Qi,* Jian Luo,* and Xingbo Liu*

Cite This: ACS Catal. 2024, 14, 14974−15013

ABSTRACT: Solar-driven thermochemical hydrogen (STCH) production represents a sustainable approach for converting solar energy into hydrogen (H_2) as a clean fuel. This technology serves as a crucial feedstock for synthetic fuel production, aligning with the principles of sustainable energy. The efficiency of the conversion process relies on the meticulous tuning of the properties of active materials, mostly commonly perovskite and fluorite oxides. This Review conducts a comprehensive review encompassing experimental, computational, and thermodynamic and kinetic property studies, primarily assessing the utilization of perovskite oxides in two-step thermochemical reactions and identifying essential attributes for future research endeavors. Furthermore, this Review delves into the application of machine learning (ML) and density functional theory (DFT) for predicting and classifying the thermochemical properties of perovskite materials. Through the integration of experimental investigations, computational modeling, and ML methodologies, this Review aspires to expedite the screening and optimization of perovskite oxides, thus enhancing the efficiency of STCH processes. The overarching objective is to propel the advancement and practical integration of STCH systems, contributing significantly to the realization of a sustainable and carbon-neutral energy landscape.

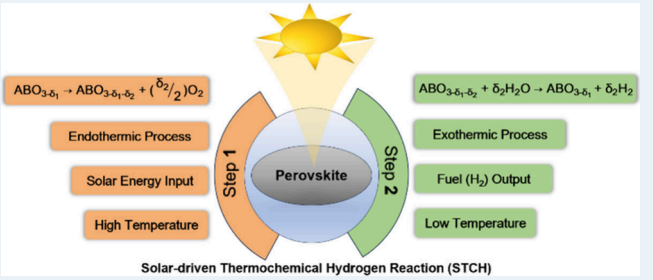

KEYWORDS: *chemical looping, solar-driven thermochemical hydrogen (STCH), thermodynamics and kinetics, renewable energy*

1. INTRODUCTION

Solar energy has emerged as a crucial and indispensable energy source, owing to its renewable, abundant, inexhaustible, and environmentally friendly attributes.[1−4] However, the intermittent nature of solar energy, confined to daylight hours and contingent on weather conditions, poses a challenge to its wide utilization.[5,6] To overcome this limitation, researchers are dedicatedly working on the development of efficient energy conversion technologies that facilitate the maximum usage of solar energy even during nonsolar periods.[7−9] Currently, diverse technologies, encompassing both artificial and natural photosynthesis and photoelectrochemistry (PEC), are being explored for hydrogen production through water (H_2O) splitting (WS), carbon monoxide (CO) generation through carbon dioxide (CO_2) splitting (CDS), and the synthesis of versatile fuels from biomass.[10,11] Particularly intriguing are technologies that enable the efficient dissociation of H_2O and CO_2 through endothermic processes, where the product of H_2 and CO can be further transformed into organic oxygenates and various liquid hydrocarbons.[12−14] Another technology rapidly gaining attention is the conversion of solar energy into fuel through solar-driven thermochemical processes.[15,16]

The traditional solar thermochemical technique entails a two-phase redox cycle utilizing ceria or perovskite materials, involving high-temperature reduction followed by oxidation. This Review delineates two main types of thermochemical cycles: multistep and two-step, with specific examples, as illustrated in Figure 1. The magnesium−chlorine (MgCl) cycle is a multistep hybrid process incorporating both electricity and heat to split water, comprising one electrolytic step and two thermochemical steps.[17] An example of the multistep thermal-only type includes manganese oxide−sodium hydroxide (MnO-NaOH), first investigated in 1999 by Sturzenegger et al.[18] However, challenges related to multiple stages, such as high reduction temperatures, significant temperature fluctuations, and complex system integration, have stimulated the exploration of simpler two-step redox reactions utilizing basic metal oxides.[19] Two-step redox metal oxides are classified into

Received: June 7, 2024
Revised: August 22, 2024
Accepted: September 6, 2024
Published: September 25, 2024

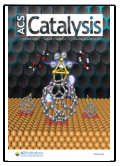

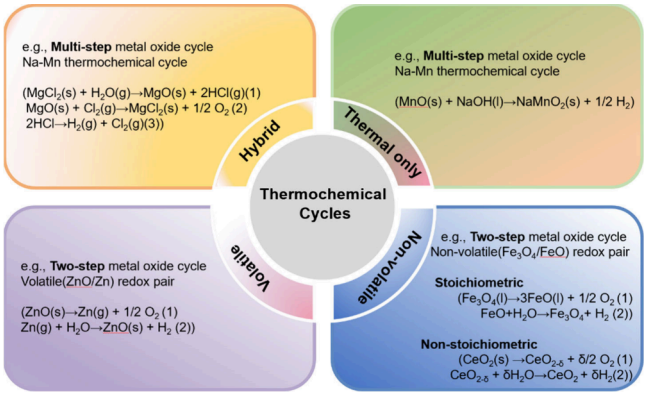

Figure 1. Examples of different types of thermochemical reactions.

volatile and nonvolatile categories. The former underwent extensive investigation from 2000 to 2010, presenting challenges in recovering condensed metallic gas species (e.g., Zn, Sn) in colder reactor sections.[20,21] The nonvolatile category encompasses stoichiometric and nonstoichiometric metal oxides. However, stoichiometric examples like iron oxide often encounter sintering issues leading to the formation of a deactivation layer of Fe_3O_4.[22] In the nonstoichiometric series, ceria stands out for its rapid oxidation kinetics, with 500 cycle reactions demonstrating promise. Despite its advantages, ceria has drawbacks, including a low degree of nonstoichiometry and the need for high reduction temperatures.[12] CeO_2 and CeO_2-based fluorite oxides have been widely reported, with CeO_2 commonly used as the benchmark material.[23,24] Herein, perovskite is considered a promising candidate due to its requirement of a low reduction temperature and large compositional design space. Additionally, perovskite exhibits significant nonstoichiometry, fast oxidation kinetics in most cases, and the ability to undergo testing across hundreds of cycles.[25]

The two-step thermochemical water-splitting method is universally recognized as a thermodynamically viable and potentially highly efficient process for generating "solar fuels".[26] Unlike other methods that depend on photon-to-electron conversion, such as electrolysis, this technology operates at elevated temperatures and has the advantage of utilizing the entire solar spectrum.[27] Chemical looping refers to a process used in solar thermochemical systems for energy conversion and storage.[28] Thermochemical reactions in this context comprise two processes: Process 1 involves the reduction of perovskite oxide under solar energy (eq 1), with the production of oxygen (O_2). Process 2 encompasses the reoxidation of the reduced perovskite oxide, leading to the evolution of fuel (H_2) (eq 2). The specific steps are illustrated in Figure 2 by considering perovskite oxide (ABO_3) in the context of solar-driven thermochemical hydrogen production.

$$ABO_{3-\delta_1} \rightarrow ABO_{3-\delta_1-\delta_2} + (\delta_2/2)O_2 \quad (1)$$

$$ABO_{3-\delta_1-\delta_2} + \delta_2 H_2O \rightarrow ABO_{3-\delta_1} + \delta_2 H_2 \quad (2)$$

Here, δ_1 represents the initial reduction extent and δ_2 denotes the additional reduction extent due to heating during process 1.

Solar thermochemical hydrogen (STCH) production has been extensively reviewed in the literature. Various reviews have covered the basic theory of thermodynamics and kinetics, different types of materials, and various reactor technologies.[29−33] For example, Aldo Steinfeld's group reviewed the use of concentrated solar radiation for high-temperature process heat, the thermodynamics of various metal oxide redox reactions, and the design and operation of solar reactors.[34−37] Some reviews have focused on specific materials, such as ceria and perovskite, used in the STCH field. For example, Stéphane Abanades' group summarized advanced redox cycles involving various metal oxides.[38,39] They highlighted the ability of these materials to produce water with high H_2 production yields, rapid reaction rates, and performance stability. Moreover, STCH as a H_2 generation method is also used to make comparisons with other methods, including PEC; for instance, Chengxiang Xiang's group has compared solar thermochemical and photoelectrochemical water-splitting methods, illustrating their respective advantages and challenges.[40] Despite these extensive studies, there is still a lack of a comprehensive summary of various B-site-based materials used in the STCH reaction, particularly regarding their thermodynamic and kinetic properties. This Review seeks to illuminate the landscape of STCH reactions, emphasizing the potential of perovskite materials from the perspectives of experimental, computational, thermodynamic, and kinetic studies as well as the complexities they entail. Ultimately, these efforts hold the potential not only to shape a more sustainable energy future but also to extend into the research field of chemical looping.

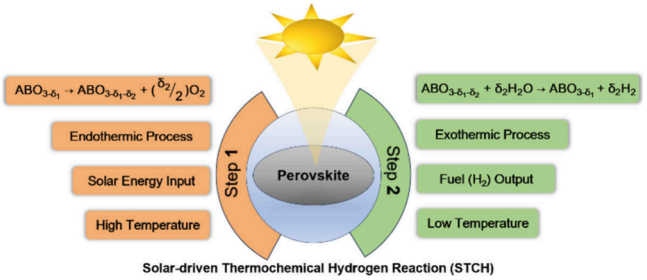

Figure 2. Schematic of the two-step water-splitting reaction using a metal oxide. In step 1, the perovskite oxide is reduced, accompanied by oxygen evolution, at high temperatures. In step 2, the perovskite is reoxidized, involving H_2 evolution, at low temperatures.

2. STRUCTURE AND PROPERTIES OF PEROVSKITE OXIDES

Perovskite-type oxides are named after $CaTiO_3$ and belong to a class of oxides with the common formula ABO_3 (where A represents a rare- or alkaline-earth metal and B represents a transition metal). In perovskite oxides, the crystal structure is characterized by a dominant 12-fold A cation sublattice, a 6-fold coordinated B cation sublattice, and an octahedral oxygen anion sublattice positioned between two B site locations. Furthermore, the cations in the A-site are larger than those in the B-site, as depicted in Figure 3.[41−44]

Inorganic perovskites, owing to their unique physical properties such as superconductivity, magnetoresistance, dielectricity, piezoelectricity, and ferroelectricity, can be applied in a variety of fields.[46] These fields include fuel cells, catalysis, thermoelectrics, batteries, and solar thermal energy, emphasizing their importance as energy materials.[47−51] When employed in solar thermal energy applications, perovskite oxides undergo thermal reduction, releasing oxygen from the lattice and creating oxygen vacancies. This process also induces changes in the oxidation states of the multivalent transition metal cations present in the structure.

https://doi.org/10.1021/acscatal.4c03357
ACS Catal. 2024, 14, 14974−15013

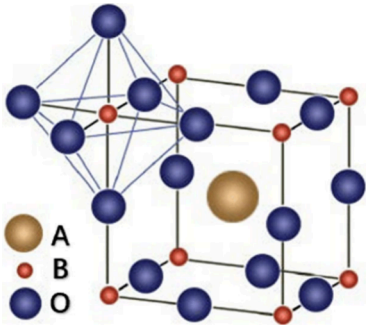

Figure 3. In the ideal perovskite structure, an octahedron of O atoms encloses the B ion, forming a three-dimensional cubic lattice through corner sharing, with the B-site ion situated at the center and surrounded by oxygen ions.[45] Reproduced from ref 45 with permission from the research repository at WVU. Copyright 2022 West Virginia University.

To maintain the perovskite phase, Victor Moritz Goldschmidt developed a tolerance factor based on the ionic radii of the cations occupying the A- and B-sites, and it serves as an important parameter in assessing perovskite structures. This so-called Goldschmidt tolerance factor, τ, is a function of the A cation radii, R_A, the B cation radii, R_B, and the O anion radii, R_O.[52]

$$\tau = \frac{R_A + R_O}{(\sqrt{2})(R_B + R_O)} \tag{3}$$

In general, materials with an ideal cubic structure have a tolerance factor (τ) within the range of $0.9 \leq \tau \leq 1.0$, while a hexagonal/tetragonal phase may form when $\tau > 1.0$, and an orthorhombic/rhombohedral phase may form when $\tau < 0.9$.[53−56] Distortions in perovskite structures can result in a variety of symmetry reductions, with orthorhombic and rhombohedral distortions being the most common.[57,58] Considering the most practical perovskite materials have mixed A and B ions, the weighted average cation radius is typically used and is expressed as follows:[59−62]

$$\tau_{avg} = \frac{\frac{\sum_{i=1}^{m} w_{A_i} R_{A_i}}{\sum_{i=1}^{m} w_{A_i}} + R_O}{\sqrt{2}\left(\frac{\sum_{i=1}^{n} w_{B_i} R_{B_i}}{\sum_{i=1}^{n} w_{B_i}}\right) + R_O} \xrightarrow{\text{equimolar}} \frac{\frac{\sum_{i=1}^{m} R_{A_i}}{m} + R_O}{\sqrt{2}\left(\frac{\sum_{i=1}^{n} R_{B_i}}{n}\right) + R_O} \tag{4}$$

where the subscript i indicates different types of cations (i = 1, 2, ..., m for A-site cations and i = 1, 2, ..., n for B-site cations), and w_{A_i} and w_{B_i} represent atomic fractions associated with R_{A_i} and R_{B_i}, respectively. Prior experiments suggested that the Goldschmidt tolerance factor needs to be closer to unity (e.g., $0.99 \leq \tau \leq 1.01$) for the formation of single-phase cubic high-entropy perovskite oxides.[62]

Despite the Goldschmidt tolerance factor's simplicity and utility in predicting perovskite stability, Christopher J. Bartel et al. developed an improved tolerance factor using a data-driven approach, which correctly predicts perovskite stability with 92% accuracy on a diverse set of 576 compounds.[63] This new factor accounts for the limitations of the traditional Goldschmidt factor, particularly in handling a broader range of ABX compositions, including halides and oxides. Incorporating these recent advancements allows for a more reliable prediction of perovskite stability and guides the discovery of new functional materials for various applications, including photovoltaics and electrocatalysis.

The ability to modify the perovskite structure provides extensive opportunities for enhancing the material properties, such as electronic and ionic conductivity.[64,65] When considering perovskites for thermochemical cycles, their reactivity for oxygen exchange and H_2O/CO_2 splitting is an important determining factor. To be suitable for this application, a perovskite material should exhibit a large range of oxygen nonstoichiometry (δ_2), possess a well-matched enthalpy of formation for oxide defects (typically oxygen vacancies), and support mobile electronic carriers that facilitate the exchange reaction at the surface.[58]

3. THERMODYNAMICS OF THE THERMOCHEMICAL WATER-SPLITTING REDUCTION CYCLE

By examining the thermodynamics of perovskites, we can predict the theoretical maximum achievable fuel production achievable in thermochemical cycles as a function of reduction and oxidation temperatures and the partial pressure of oxygen. This ΔG_O° can be calculated using the standard enthalpy change (ΔH_O°) and the standard entropy change (ΔS_O°) according to the following equation:[25]

$$\Delta G_O^\circ = \Delta H_O^\circ - T\Delta S_O^\circ \tag{5}$$

These relationships were formulated under the assumption that the individual values of ΔG_O° and ΔS_O° remain temperature-independent (T) and are solely reliant on the extent of nonstoichiometry (δ_2).[29] This presumption is reasonable for minor fluctuations in δ_2 and when the crystal structure is maintained. Considering that oxygen behaves as an ideal gas and the solid activity is unity, the ΔG_O° at equilibrium can be determined as follows:

$$\Delta G_O^\circ(T, \delta_2) = -\frac{1}{2} RT \ln(P_{O_2}) \tag{6}$$

The thermodynamics of active materials represent their most crucial attributes, which are essential for making unbiased comparisons between different materials and in system models. Hence, obtaining accurate thermodynamic data is of paramount importance. In the literature, one primary method is prevalent for calculating thermodynamic properties of materials used in solar thermochemical hydrogen (STCH) production: the van't Hoff analysis.[66]

The thermodynamics of reduction parameters (the reduction enthalpy change (ΔH_{red}°) and the reduction entropy change (ΔS_{red}°)) of perovskite can be measured by thermogravimetric analysis (TGA) according to the equation below:[67,68]

$$\lim_{\delta_2 \to 0} ABO_{3-\delta_1-\delta_2} + \frac{\delta_2}{2} O_2 \rightarrow ABO_{3-\delta_1} \tag{7}$$

According to the van't Hoff method, in the limit of an infinitesimal extent of reduction, the chemical activities of $ABO_{3-\delta_1}$ and $ABO_{3-\delta_1-\delta_2}$ become equal. Therefore, the equilibrium reaction constant (K_{red}^{eq}) can be given by

$$K_{red}^{eq} = \hat{P}_{O_2}^{1/2} = \exp\left\{\frac{-\Delta_{red} G^\circ(T, \delta)}{RT}\right\} \tag{8}$$

where $\hat{P}_{O_2}$ is the P_{O_2} relative to the reference standard pressure of 1 atm. The Arrhenius plot of eq 8 can be written in the form

https://doi.org/10.1021/acscatal.4c03357
ACS Catal. 2024, 14, 14974−15013

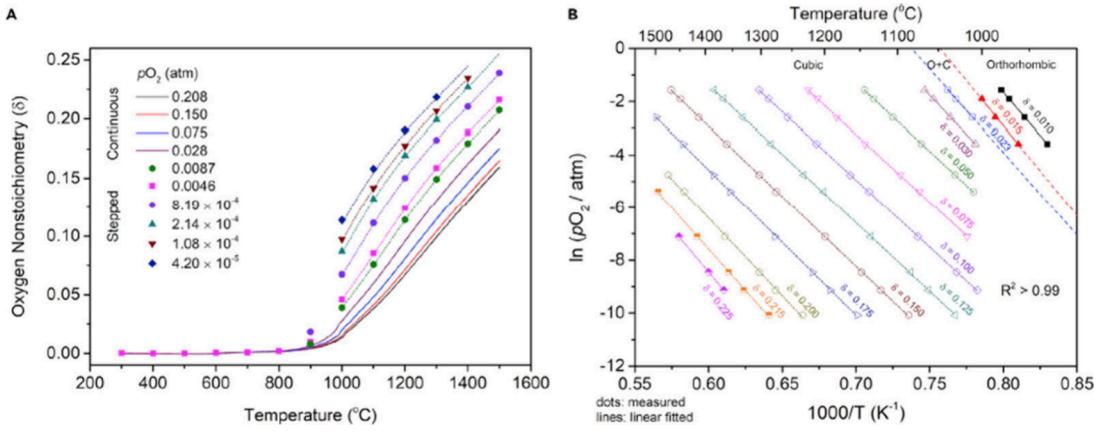

Figure 4. The process for performing the van't Hoff method is illustrated as follows: (a) a map of temperature, pressure, and oxygen nonstoichiometry for $CaTi_{0.5}Mn_{0.5}O_{3-\delta}$ and (B) straight lines that are linear fits to the plotted data points.[66] Reproduced from ref 66. Available under a Creative Commons CC-BY-NC-ND license. Copyright 2020 Qian and co-workers.

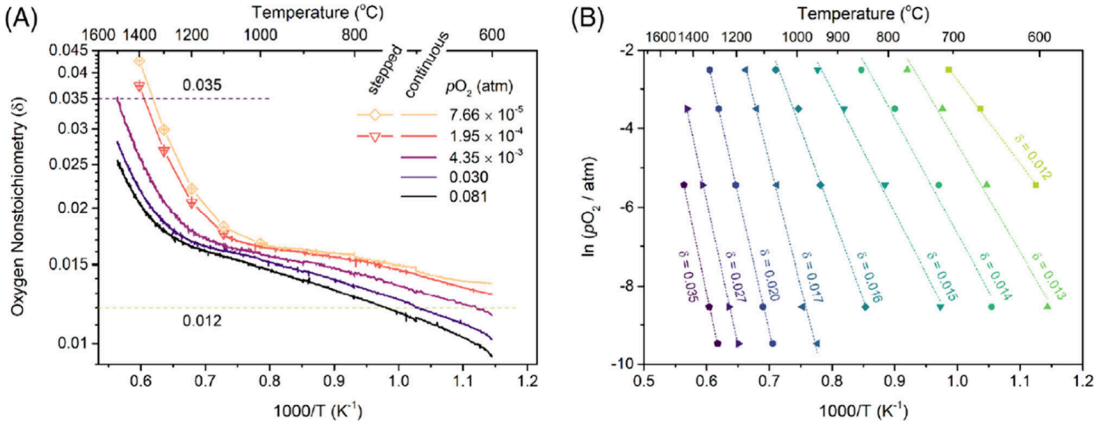

Figure 5. (A) Oxygen nonstoichiometry measured using both continuous and stepwise heating at the indicated P_{O_2} values. (B) An Arrhenius presentation is used to extract thermodynamic properties using the van't Hoff method, with representative fixed δ values ranging between 0.012 and 0.035.[71] Reproduced with permission from ref 71. Copyright 2022 John Wiley and Sons.

$$\ln(P_{O_2}) = 2\left(\frac{-\Delta_{red}H^{\circ}_{(\delta)}}{RT} + \frac{\Delta_{red}S^{\circ}_{(\delta)}}{R}\right) \quad (9)$$

$\Delta_{red}H^{\circ}_{(\delta)}$ and $\Delta_{red}S^{\circ}_{(\delta)}$ can be extracted from the slopes and intercepts of the plots of $\ln(P_{O_2})$ vs $1/T$ for each δ, respectively.

According to the van't Hoff method, a graph is constructed in the Arrhenius form, plotting the set of values for oxygen partial pressure against corresponding temperatures for a specified value of δ. From this graph, the slope and y-intercept can be determined, which correspond to the enthalpy and entropy, respectively. Figure 4, which illustrates an instance of this analysis for the perovskite oxide $CaTi_{0.5}Mn_{0.5}O_{3-\delta}$, clearly displays a minor anomaly at a temperature of 980 °C. This feature indicates a transition to a cubic phase, an attribute also observed in the oxide $CaMnO_{3-\delta}$.[66,69,70]

Xin Qian et al. first reported the experimental protocols for evaluating the redox thermodynamics of nonstoichiometric oxides, focusing on $YMnO_{3-\delta}$, as depicted in Figure 5.[71] They employed a temperature-stepped protocol involving long isothermal holds. Interpolation was necessary for analyzing the results obtained from these stepped measurements, with a preference for $\ln(\delta)$ versus $1/T$ plane analysis over δ versus T.[71]

The following equation is given to consider the influence of temperature at the first thermolysis reactions:[72]

$$T_{red} \geq \frac{\Delta H_{red}}{\Delta S^{\circ}_{red} - \frac{1}{2}R\ln\left(\frac{P_{O_2}}{bar}\right)} \quad (10)$$

In the given conditions, ΔH_{red} is approximately 250 kJ mol_o^{-1} and ΔS°_{red} is nearly constant at around 57 J $(mol_o\ K)^{-1}$ in the reduction process of water-splitting. At fixed P_{O_2}, T_{red} can be reduced only by either decreasing ΔH_{red} or increasing ΔS°_{red}. However, a large ΔH_{red} is required to provide the necessary driving force for the reduction of ABO_3. Therefore, a large ΔS°_{red} holds a pivotal role in the success of materials for thermochemical splitting.

The ΔS°_{red} may be decomposed into two parts: (1) a gas-phase contribution arising from the release of half a mole of O_2 and (2) a solid-state contribution (or more broadly, an oxide/metal contribution) indicating the entropy variation in the oxide between its oxidized and reduced states.[72]

$$\Delta S^{\circ}_{red} = S_{prods} - S_{reacts} = \frac{1}{2}S_{O_2} + \Delta S_{solid} \quad (11)$$

In this condition,

https://doi.org/10.1021/acscatal.4c03357
ACS Catal. 2024, 14, 14974−15013

$$\Delta G_{TR} = \Delta H_{reduction} - T_{TR}\left(\frac{1}{2}S_{O_2} + \Delta S_{solid}\right) \leq 0 \quad (12)$$

and

$$\Delta G_{GS} = -\Delta H_{reduction} - \Delta H_{f,T_{GS}}^{H_2O} - T_{GS}\left(-\frac{1}{2}S_{O_2} - \Delta S_{solid} + S_{T_{GS}}^{H_2} - S_{T_{GS}}^{H_2O}\right) \leq 0 \quad (13)$$

The van't Hoff model is extensively employed in solar thermochemical materials due to its relatively straightforward application. Generally, there exists considerable flexibility between the ΔH_{red} and ΔS_{red}° terms, leading to the potential misallocation of energies between enthalpy and entropy terms. Therefore, while nonstoichiometry might be predicted with accuracy, achieving precision in the determination of partial molar entropies and enthalpies could be challenging. Moreover, employing linear regression within the van't Hoff space might result in inaccuracies, particularly when dealing with a narrow temperature range. The inherent $1/T$ nature of this transformation leads to a concentration of higher-temperature data points, potentially amplifying experimental errors during the determination of the slope (ΔH_{red}) and intercept (ΔS_{red}°). As a result, its application should prioritize broader temperature ranges and encompass an investigation into nonstoichiometry at lower temperatures.[27]

Computational methods can be utilized to predict the thermodynamics of proposed water-splitting cycles after the materials are used in two-step water-splitting cycles. C. Wolverton's group screened all binary oxides (CeO_2, ZnO, Nb_2O_5, In_2O_3, SnO_2, WO_3, Fe_3O_4, CdO, Mn_3O_4, and Co_3O_4) for use in thermochemical H_2O splitting, as depicted in Figure 6.[27,73] They discovered that these oxides tend to aggregate close to the thermal reduction (TR) and gas splitting (GS) equilibrium lines. It is reasonable that most oxides also prefer GS slightly because the GS reaction is more likely affected by slow kinetics. Figure 6 shows that none of the evaluated reactions achieve the requisite combination of ΔH_{red} and ΔS_{red}° necessary to facilitate favorable TR and GS energetics. However, it is noted that ΔS_{red}° serves as a means to create an optimal range for values exceeding 10 cal (0.5 mol O_2 K)$^{-1}$. Achieving a substantial positive ΔS_{red}° is a complex task due to the fact that MO_{x-1} contains fewer atoms compared to MO_x, resulting in fewer vibrational degrees of freedom. Additionally, based on eqs 12 and 13, identifying or developing materials that possess a substantial positive ΔS_{red}° and also exhibit a corresponding ΔH_{red} is an ongoing challenge.

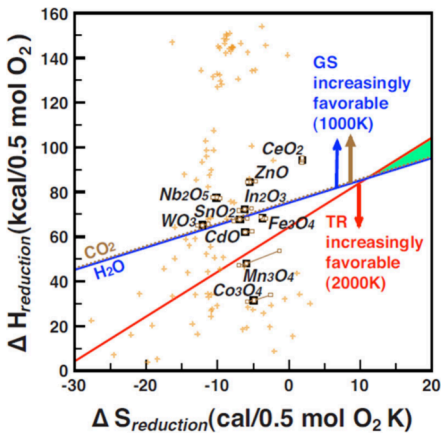

Figure 6. Computational screening for the utilization of monometal oxides in thermochemical water-splitting was conducted by C. Wolverton et al.[73] The screening encompassed considerations of oxidation and reduction toward equilibrium as well as reduction under atmospheric pressures. The "ideal" materials would be positioned within the designated green triangle region.[27] Reproduced with permission from ref 73. Copyright 2009 American Physical Society.

4. KINETICS OF THE THERMOCHEMICAL WATER-SPLITTING CYCLE

Theoretical limits on fuel production are determined by thermodynamic restrictions, while kinetic restrictions dictate the maximum quantity of fuel that can be generated within a reasonable duration. Here, the common methods used to investigate the kinetics of redox reactions involving perovskites will be discussed. The H_2 output depends on thermodynamics, the reaction kinetics, the mass transport, etc.; therefore, it highly depends on the measurement protocol.

The rate of a solid-state reaction can generally be described by[74,75]

$$\frac{d\alpha}{dt} = A\exp\left(-\frac{E_a}{RT}\right)f(\alpha) \quad (14)$$

where α represents the conversion fraction, A stands for the pre-exponential (frequency) factor, E_a denotes the activation energy, R signifies the gas constant, and T represents the absolute temperature. The function $f(\alpha)$ represents the reaction model. For a gravimetric measurement, α can be defined by the following equation:[74]

$$\alpha = \frac{W_0 - W_t}{W_0 - W_\infty} \quad (15)$$

where W_0 is the initial weight, the W_t is the weight at time t, and W_∞ is the final weight.

Jonathan R. Scheffe et al. were the first to introduce a computational method for analyzing the transient H_2 production rate observed during water-splitting. This method takes the following into account: (1) the kinetics inherent to the solid state, (2) the time needed to infuse the reacting chamber with water vapor, (3) delays associated with the detector, and (4) the distribution and blending of H_2 as it moves from the solid surface and travels downstream to the measurement device. Many earlier studies overlooked the significance of the experimental nuances (specifically points 2−4), and this oversight could result in inaccurate findings.[76]

A. H. McDaniel et al. also employed this computational approach, using water-splitting as an example of oxidation chemistry. They introduced steam into the reactor volume through a step-function input that triggers the solid-state chemical reactions, as shown in Figure 7(a).[77]

They determined the shape of this step function by utilizing a transient 3D computational fluid dynamics model of the reactor inlet under different operational conditions and by gas-injection tracer studies. Subsequent chemical reactions are viewed as a black box, characterized by kinetic models from solid-state kinetic theory, as shown in Figure 7(b). These models monitor a single variable, α, symbolizing the reaction

https://doi.org/10.1021/acscatal.4c03357
ACS Catal. 2024, 14, 14974−15013

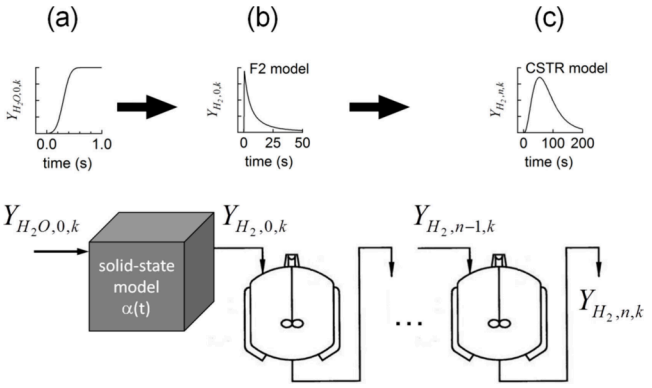

Figure 7. The kinetic model employed by Jonathan et al.[76] is schematically depicted as follows: (a) a step function representing the introduction of steam, (b) an H_2 evolution curve derived from the solid-state model, and (c) the H_2 flow rate following its mixing and dispersion within a continuously stirred tank reactor (CSTR). Reproduced with permission from ref 76. Copyright 2013 RSC Publishing.

extent, adhering to the Arrhenius behavior according to the following equation:[78]

$$\frac{d\alpha}{dt} = Ae^{[-E_a/RT]}[Y_{H_2O}(t)]\gamma f(\alpha) \quad (16)$$

where Y_{H_2O} represents the mole fraction of steam in the inlet, and γ is an exponent determining the reliance on steam concentration. The example given in Figure 7(b) depicts a second order relation represented by the formula $f(\alpha) = (1 - \alpha)^2$. The time duration of the transient pulse-like H_2 input into the continuously stirred tank reactors (CSTR) is extended as a result of dispersion and mixing processes (shown in Figure 7(c)). Using the least-squares method, the kinetic model and its associated parameters are determined. When a single kinetic model does not align well with the experimental data, two parallel kinetic models are employed. This method enables the simultaneous calculation of all kinetic parameters, considering the impact of physical processes dependent on the experimental setup. However, it necessitates numerical reactor simulation and data-fitting calculations, offering a suitable approach to precisely investigate the oxidation kinetics.[78,79]

The electrical conductivity relaxation (ECR) method, with its long history dating back to its earliest use by Dünwald and Wagner in 1934, is considered a "classic" tool in some sense. WooChul Jung's group measured the surface oxygen exchange kinetic parameters of $(La,Sr)MnO_{3-\delta}$ thin film using electrical conductivity relaxation (ECR) measurements. Two electrodes (Pt) were placed on the $La_{1-x}Sr_xMnO_{3-\delta}$ coating.[80] In order to support the hypothesis of a first-order surface oxygen exchange reaction and the linear variation of conductivity with oxygen partial pressure, experiments were conducted for both the reduction and oxidation process. The experimental data were fitted by the following equation:[81]

$$\frac{\sigma(t) - \sigma(0)}{\sigma(\infty) - \sigma(0)} = 1 - \exp\left(-\frac{K_s}{a}t\right) \quad (17)$$

where σ symbolizes the conductivity with respect to time, K_s stands for the surface reaction rate constant, and a is the sample thickness. The solid-state reaction rate constant K_s can be obtained from both experimental data and eq 17. The ECR method permits the investigation of surface oxygen exchange only and not the bulk. For example, YeonJu Kim et al. investigated the influence of the Sr concentration on the surface reaction kinetics of $La_{1-x}Sr_xMnO_{3-\delta}$ as shown in Figure 8 (a). Thin films of $La_{1-x}Sr_xMnO_{3-\delta}$ (where x = 0.1, 0.2, 0.3, 0.4) are synthesized through pulsed laser deposition, resulting in flat and dense surfaces. These films are subsequently analyzed for their K_s utilizing ECR under operational conditions (with temperatures ranging from 650 to 800 °C and oxygen partial pressures spanning from 2.9×10^{-19} to 9.0

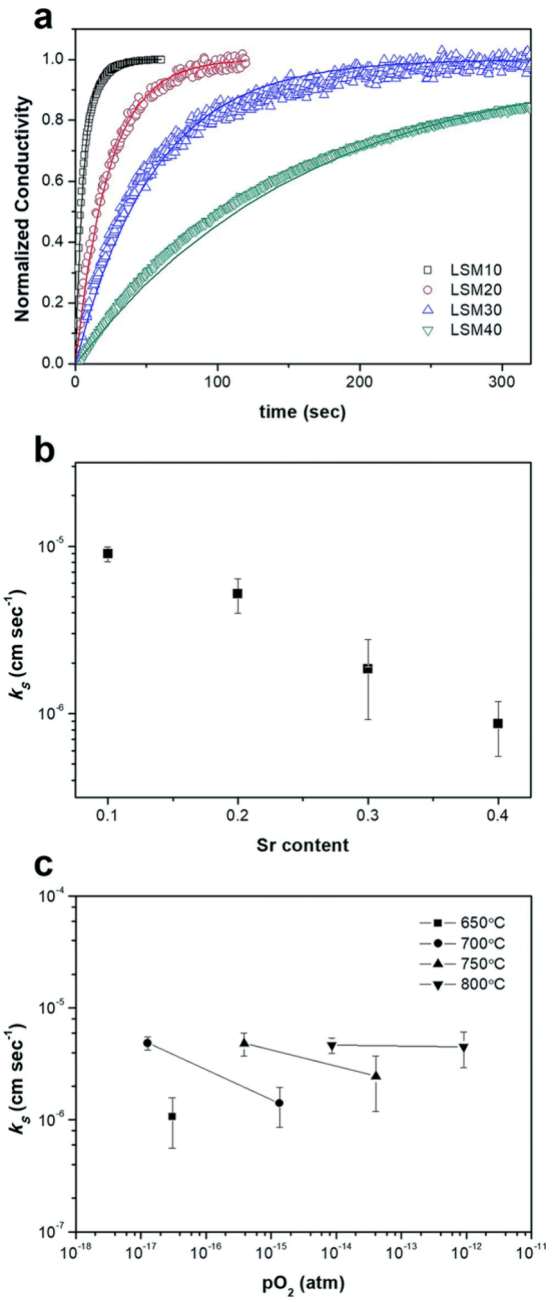

Figure 8. (a) Relaxation profiles of $La_{1-x}Sr_xMnO_{3-\delta}$ with different Sr contents at 800 °C, $P_{O_2} = 9.0 \times 10^{-15}$ atm, (b) a comparative analysis of the K_s values under same conditions, and (c) surface oxygen exchange coefficients of $La_{0.8}Sr_{0.2}MnO_{3-\delta}$ across different temperature and P_{O_2} values within a CO/CO_2 environment. The solid lines in (a) depict the fitted profiles.[80] Reproduced with permission from ref 80. Copyright 2018 RSC Publishing.

https://doi.org/10.1021/acscatal.4c03357
ACS Catal. 2024, 14, 14974−15013

Table 1. STCH Performance of Mn-Based Perovskite Oxides under Inert Gas Conditions

composition	synthesis method	cycles	$\Delta\delta$	temp. red./ox. (°C)	time red./ox. (min)	H_2O (% vol)	gas red./ox.	O_2 yield (μmol g^{-1})	H_2 yield (μmol g^{-1})	average H_2 production rate (μmol g^{-1} min^{-1})	ref
$LaMnO_{3-\delta}$	Pechini	3		1350/1000	1/60	84.0	N_2/N_2	112.8[a]	68.1[a]	1.14	90
$La_{0.9}Sr_{0.1}MnO_{3-\delta}$	solid-state	1	0.014	1400/800	12/8	20.0	Ar/Ar	24.6[a]	40.6[a]	5.08	91
$La_{0.7}Sr_{0.3}MnO_{3-\delta}$	solid-state	1	0.072	1400/800	60/31	20.0	Ar/Ar	151.8[a]	253.6[a]	8.18	91
$La_{0.6}Sr_{0.4}MnO_{3-\delta}$	solid-state	8	0.127	1400/800	70/65	20.0	Ar/Ar	218.8[a]	397.8[a]	6.12	91
$La_{0.8}Sr_{0.2}MnO_{3-\delta}$	solid-state	21	0.017	1400/800	47/16	20.0	Ar/Ar	64.7[a]	129.0[a]	8.06	91
$La_{0.8}Sr_{0.2}MnO_{3-\delta}$	commercial	1		1400/-	45/-		Ar/-	112.0			95
$La_{0.65}Sr_{0.35}MnO_{3-\delta}$	commercial	1		1400/1050	45/45	80.0	Ar/Ar	166.0	124.0	2.76	95
$La_{0.65}Sr_{0.35}MnO_{3-\delta}$	commercial	2		1400/1050		80.0	Ar/Ar		113.0		95
$La_{0.5}Sr_{0.5}MnO_{3-\delta}$	solid-state	1		1400/1000	45/45	80.0	Ar/Ar	298.0	195.0	4.33	95
$La_{0.5}Sr_{0.5}MnO_{3-\delta}$	solid-state	2		1400/1000		80.0	Ar/Ar		160		95
$La_{0.5}Sr_{0.5}MnO_{3-\delta}$	solid-state	1		1400/900	45/45	80.0	Ar/Ar	298.0	170.0	3.78	95
$La_{0.5}Sr_{0.5}MnO_{3-\delta}$	solid-state	2		1400/900			Ar/Ar		133		95
$Sr_{0.75}Ce_{0.25}MnO_{3-\delta}$	Pechini	3		1400/1000	5.5/20	40.0	Ar/Ar	104.0	224.0	11.2	76
$Sr_{0.75}Ce_{0.25}MnO_{3-\delta}$	Pechini	3		1350/850	5.5/20	40.0	Ar/Ar	68.0	98.0	4.9	76
$La_{0.65}Sr_{0.35}MnO_{3-\delta}$	commercial	1		1400/-	45/-		Ar/-	100.0			102
$La_{0.5}Sr_{0.5}MnO_{3-\delta}$	solid-state	1		1400/1000	100/100		N_2/N_2	193.0	308.0	3.08	102
$La_{0.65}Ca_{0.35}MnO_{3-\delta}$	solid-state	1		1400/1100	45/-		Ar/-	109.0			102
$La_{0.5}Ca_{0.5}MnO_{3-\delta}$	solid-state	1		1400/1000	100/100		N_2/N_2	272.0	407.0	4.07	102
$La_{0.35}Ca_{0.65}MnO_{3-\delta}$	solid-state	1		1400/1100	45/-		Ar/-	653.0			102
$La_{0.5}Sr_{0.5}MnO_{3-\delta}$	solid-state	1	0.088	1400/1100	45/-		Ar/-	198.0			103
$Nd_{0.5}Sr_{0.5}MnO_{3-\delta}$	solid-state	1	0.117	1400/1100	45/-		Ar/-	264.0			103
$Sm_{0.5}Sr_{0.5}MnO_{3-\delta}$	solid-state	1	0.135	1400/1100	45/-		Ar/-	301.0			103
$Gd_{0.5}Sr_{0.5}MnO_{3-\delta}$	solid-state	1	0.148	1400/1100	45/-		Ar/-	330.0			103
$Dy_{0.5}Sr_{0.5}MnO_{3-\delta}$	solid-state	1	0.179	1400/1100	45/-		Ar/-	393.0			103
$Y_{0.5}Sr_{0.5}MnO_{3-\delta}$	solid-state	1	0.192	1400/1100	45/140		N_2/N_2	481.0	320.0	2.29	103
$La_{0.5}Ca_{0.5}MnO_{3-\delta}$	solid-state	1	0.122	1400/1100	45/-		Ar/-	312.0			103
$Nd_{0.5}Ca_{0.5}MnO_{3-\delta}$	solid-state	1	0.135	1400/1100	45/-		Ar/-	343.0			103
$Sm_{0.5}Ca_{0.5}MnO_{3-\delta}$	solid-state	1	0.147	1400/1100	45/-		Ar/-	361.0			103
$Gd_{0.5}Ca_{0.5}MnO_{3-\delta}$	solid-state	1	0.134	1400/1100	45/-		Ar/-	404.0			103
$Dy_{0.5}Ca_{0.5}MnO_{3-\delta}$	solid-state	1	0.200	1400/1100	45/-		Ar/-	493.0			103
$Y_{0.5}Ca_{0.5}MnO_{3-\delta}$	solid-state	1	0.200	1400/1100	45/140		N_2/N_2	593.0	310.0	2.21	103
$La_{0.8}Sr_{0.2}MnO_{3-\delta}$	commercial	4	0.013	1400/1400			N_2/N_2	145.2	49.6		97
$La_{0.65}Sr_{0.35}MnO_{3-\delta}$	commercial	4	0.055	1400/1400			N_2/N_2	137.9	49.6		97
$La_{0.8}Sr_{0.2}MnO_{3-\delta}$	CALPHAD			1400/800		20.0		58.0[a]	116.1[a]		98
$La_{0.7}Sr_{0.3}MnO_{3-\delta}$	CALPHAD			1400/800		20.0		126.0[a]	250.5[a]		98
$La_{0.6}Sr_{0.4}MnO_{3-\delta}$	CALPHAD			1400/800		20.0		116.1[a]	392.9[a]		98
$LaMnO_{3-\delta}$	Pechini	1		1300/900	60/60	40.0	Ar/Ar	76.0	48.0	0.80	110
$La_{0.6}Sr_{0.4}MnO_{3-\delta}$	Pechini	1		1300/900	60/60	40.0	Ar/Ar	126.0	215.0	3.58	110
$La_{0.6}Ca_{0.4}MnO_{3-\delta}$	Pechini	1		1300/900	60/60	40.0	Ar/Ar	167.0	312.0	5.2	110
$Ba_{0.4}La_{0.6}MnO_{3-\delta}$	Pechini	1		1300/900	60/60	40.0	Ar/Ar	113.0	179.0	2.98	110
$La_{0.9}Sr_{0.1}MnO_{3-\delta}$		1	0.010	1385/840	40/5	20.0	Ar/Ar	TBD	TBD	0	111
$La_{0.8}Sr_{0.2}MnO_{3-\delta}$		1	0.040	1440/795	40/15	20.0	Ar/Ar	TBD	TBD	0	111
$La_{0.7}Sr_{0.3}MnO_{3-\delta}$		1	0.070	1440/810	40/30	20.0	Ar/Ar	TBD	TBD	0	111
$La_{0.6}Sr_{0.4}MnO_{3-\delta}$		1	0.130	1385/840	40/30	20.0	Ar/Ar	TBD	TBD	0	111
$La_{0.6}Sr_{0.4}MnO_{3-\delta}$	Pechini	1		1300/900	60/60	40.0	Ar/Ar	126.0	234.0	3.90	104
$La_{0.8}Ca_{0.2}MnO_{3-\delta}$	Pechini	1		1300/900	60/60	40.0	Ar/Ar	94.0	187.0	3.12	104
$La_{0.6}Ca_{0.4}MnO_{3-\delta}$	Pechini	1		1300/700	60/60	40.0	Ar/Ar	167.0	194.5	3.24	104
$La_{0.6}Ca_{0.4}MnO_{3-\delta}$	Pechini	1		1300/800	60/60	40.0	Ar/Ar	167.0	235.5	3.93	104
$La_{0.6}Ca_{0.4}MnO_{3-\delta}$	Pechini	6		1300/900	60/60	40.0	Ar/Ar	167.0	314.0	5.23	104
$La_{0.6}Ca_{0.4}MnO_{3-\delta}$	Pechini	1		1300/1000	60/60	40.0	Ar/Ar	167.0	267.5	4.46	104
$La_{0.6}Ca_{0.4}MnO_{3-\delta}$	Pechini	1		1300/1100	60/60	40.0	Ar/Ar	167.0	241.9	4.03	104
$La_{0.4}Ca_{0.6}MnO_{3-\delta}$	Pechini	1		1300/900	60/60	40.0	Ar/Ar	224.0	243.0	4.05	104
$La_{0.2}Ca_{0.8}MnO_{3-\delta}$	Pechini	1		1300/900	60/60	40.0	Ar/Ar	402.0	162.0	2.70	104
$La_{0.6}Sr_{0.4}MnO_{3-\delta}$	Pechini	1	0.058	1300/900	60/60	40.0	Ar/Ar	131.0	234.0	3.90	105

https://doi.org/10.1021/acscatal.4c03357
ACS Catal. 2024, 14, 14974−15013

Table 1. continued

composition	synthesis method	cycles	$\Delta\delta$	temp. red./ox. (°C)	time red./ox. (min)	H_2O (% vol)	gas red./ox.	O_2 yield (μmol g^{-1})	H_2 yield (μmol g^{-1})	average H_2 production rate (μmol g^{-1} min^{-1})	ref
$Ce_{0.1}Sr_{1.9}MnO_{3-\delta}$	evaporation	2	0.180	1400/1000	5.5/20	40.0	Ar/Ar	240.0	218.0	10.9	108
$Ce_{0.2}Sr_{1.8}MnO_{3-\delta}$	evaporation	2		1400/1000	5.5/20	40.0	Ar/Ar	168.0	247.0	12.35	108
$Ce_{0.3}Sr_{1.7}MnO_{3-\delta}$	evaporation	2	0.090	1400/1000	5.5/20	40.0	Ar/Ar	129.0	166.0	8.30	108
$SrMnO_3$	Pechini	1		1400/1000	5.5/16.7	50.0	Ar/Ar		0.0	0	108
$La_{0.6}Sr_{0.4}MnO_{3-\delta}$	Pechini		0.0038	1300/700	13.3/20	1.3	Ar/Ar		17.0	0.85	101
$La_{0.6}Sr_{0.4}MnO_{3-\delta}$	Pechini		0.0059	1300/500	13.3/20	1.3	Ar/Ar		27.0	1.35	101
$La_{0.6}Sr_{0.4}MnO_{3-\delta}$	Pechini		0.0121	1300/500	13.3/40	1.3	Ar/Ar		55.0	1.38	101
$Sr_{0.86}Ce_{0.14}MnO_{3-\delta}$	Pechini	1		1350/850	5.5/20	40.0	Ar/Ar		91.9	4.60	109
$Sr_{0.86}Ce_{0.14}MnO_{3-\delta}$	Pechini	1		1350/1000	5.5/20	40.0	Ar/Ar		177.1	8.86	109
$Sr_{0.86}Ce_{0.14}MnO_{3-\delta}$	Pechini	1		1400/850	5.5/20	40.0	Ar/Ar		153.2	7.66	109
$Sr_{0.86}Ce_{0.14}MnO_{3-\delta}$	Pechini	1		1400/1000	5.5/20	40.0	Ar/Ar		242.4	12.12	109
$Sr_{0.8}Ce_{0.2}MnO_{3-\delta}$	Pechini	1		1350/850	5.5/20	40.0	Ar/Ar		99.9	5.00	109
$Sr_{0.8}Ce_{0.2}MnO_{3-\delta}$	Pechini	1		1350/1000	5.5/20	40.0	Ar/Ar		154.5	7.73	109
$Sr_{0.8}Ce_{0.2}MnO_{3-\delta}$	Pechini	1		1400/850	5.5/20	40.0	Ar/Ar		158.5	7.93	109
$Sr_{0.8}Ce_{0.2}MnO_{3-\delta}$	Pechini	1		1400/1000	5.5/20	40.0	Ar/Ar		220.0	11.00	109
$Sr_{0.7}Ce_{0.3}MnO_{3-\delta}$	Pechini	1		1350/850	5.5/20	40.0	Ar/Ar		90.6	4.53	109
$Sr_{0.7}Ce_{0.3}MnO_{3-\delta}$	Pechini	1		1350/1000	5.5/20	40.0	Ar/Ar		163.8	8.19	109
$Sr_{0.7}Ce_{0.3}MnO_{3-\delta}$	Pechini	1		1400/850	5.5/20	40.0	Ar/Ar		210.4	10.52	109
$Sr_{0.7}Ce_{0.3}MnO_{3-\delta}$	Pechini	1		1400/1000	5.5/20	40.0	Ar/Ar		305.0	15.25	109
$La_{0.6}Sr_{0.4}MnO_3$		1	0.0322	1500/800	20.5/4.3	50.0	Ar/Ar		147.32[#]	34.26	88
$La_{0.8}Sr_{0.2}MnO_3$		1	0.0319	1500/800	14.7/5.7	50.0	Ar/Ar		138.39[#]	24.28	88
$La_{0.6}Sr_{0.4}MnO_3$		1	0.0179	1400/800	31.0/5.4	50.0	Ar/Ar		80.36[#]	14.88	88
$La_{0.8}Sr_{0.2}MnO_3$		1	0.015	1400/802	14.8/4.9	50.0	Ar/Ar		62.5[#]	12.76	88

[a]Value converted from mL $g_{material}^{-1}$. Standard volume occupied: 22400 mL mol^{-1}.

$\times 10^{-13}$ atm). The Sr concentration increases, leading to a significant deceleration in oxygen exchange, as depicted in Figure 8 (b). Figure 8 (c) shows that for a given Sr concentration the oxygen exchange displays limited fluctuations across a broad range of P_{O_2} values near the 800 °C target temperature. These findings have practical implications for selecting an optimal oxygen carrier composition for enhanced fuel production performance.[80]

5. DEVELOPMENT OF PEROVSKITE OXIDES FOR SOLAR THERMOCHEMICAL WATER-SPLITTING

As previously mentioned, the two-step STCH cycle capitalizes on the redox behavior of metal oxides, allowing for the water-splitting reaction to occur at lower temperatures and directly controlling the amount of H_2 produced by the quantity of oxide used.[82−85] In this case, searching for a suitable redox material with satisfactory properties is the key research area. Theoretically, a metal oxide used in water-splitting should consider the following:

- Large reducibility ($\Delta\delta$) of the materials at moderate temperatures.
- Suitable thermodynamic properties: materials suitable for H_2O splitting require specific thermodynamic properties (reduction of enthalpy; reduction of entropy) within an appropriate window of values.[86]
- Fast redox kinetics.
- Morphological
- Phase stability.
- Synthesis method used to synthesize the STCH material.
- Cycling capability of the materials across the temperature range.

Most of the studies focus on material evaluation for STCH. Tables 1−10 collect and summarize the following performance metrics, consolidating units to a single format:

- Temperature range, which consists of the reduction temperature and the oxidation temperature.
- The amount of time the sample was exposed to the reduction temperature and oxidation temperature.
- The concentration of steam (H_2O, % vol) used for the reoxidation of the material.
- The gas used to reduce the material and carry the steam.
- The amount of O_2 released by the material at the end of the reduction time.

Moreover, the average H_2 production rates are also included (Tables 1−10), providing a more comprehensive view of the data and allowing for better comparisons.

- **Thermodynamic and kinetic influences**: The average H_2 production rate is influenced by both the thermodynamic and kinetic properties of perovskite oxides. As shown in the tables, a higher $\Delta\delta$ indicates stronger thermodynamic properties, which are critical for the first step of the water-splitting process.[87] However, the second step of water-splitting is primarily dependent on the kinetic properties of the perovskite material. This analysis indicates that both kinetics and thermodynamics are crucial parameters for evaluating the performance of perovskites in solar thermochemical water-splitting.[88]
- **Comparison with fluorite oxides**: In comparison, fluorite oxides, particularly CeO_2, outperform perovskites in terms of H_2 production rates.[26] This is primarily due to their higher surface reactivity and faster oxygen exchange kinetics. Additionally, fluorite oxides exhibit better phase stability and resistance to sintering at high

https://doi.org/10.1021/acscatal.4c03357
ACS Catal. 2024, 14, 14974−15013

temperatures, ensuring stable performance over long-term cycling.[89]

5.1. Mn-Based Perovskite Oxides as Redox-Active Oxygen Exchange Materials. Lanthanum manganite ($LaMnO_{3-\delta}$) in near-stoichiometry contains an average +3 oxidation state, accompanied by Jahn−Teller distortion. Researchers like Nobuyuki Gokon et al. have observed that $LaMnO_3$ displays high oxygen-release activity, although the oxygen release rate decreased with cycling.[90] The introduction of Sr^{2+} can increase the reduction extent ($\Delta\delta$) and improve fuel production compared to $LaMnO_{3-\delta}$.[91,92] However, the ideal Sr content for substituting La lies between 0.3 and 0, as exceeding this range negatively impacts the reoxidation yield.[93] Aldo Steinfeld's group conducted an experimental and thermodynamic investigation of $La_{1-x}Sr_xMnO_{3-\delta}$ (x = 0.3, 0.4). They developed a defect model based on low-temperature oxygen nonstoichiometry data and extrapolated it to higher temperatures. Theoretical solar-to-fuel conversion efficiencies for $La_{0.6}Sr_{0.4}MnO_3$ are 16% at 1800 K and 13% at 1600 K.[94] Recently, Jiahui Lou et al. introduced a new model for rapidly evaluating nonstoichiometric oxides used in two-step solar thermochemical cycling, focusing on solar-to-fuel efficiency. It considers the oxide material thermodynamics and typical experimental conditions. The model's application revealed that CeO_2, under optimal cycling conditions, achieved the highest efficiency (12.9% at a reduction temperature of 1500 °C) compared to other materials, including 20 mol % Zr-doped CeO_2 (10.1%), $La_{0.8}Sr_{0.2}MnO_3$ (3.3%), and $La_{0.6}Sr_{0.4}MnO_3$ (2.5%). Moreover, the model could be enhanced by considering reaction kinetics for oxidation temperatures under 800−1000 °C.[88] The mixed ionic-electronic conductor $La_{1-x}Sr_xMnO_{3-\delta}$ (x = 0.2, 0.35, 0.5) is commonly used in fuel cells due to its reactivity toward oxygen vacancy formation upon heating and its ability to transport oxide ions, which is also vital during the second step of STCH. Moreover, Stéphane Abanades's group highlighted the importance of significant ionic conductivity at high temperatures for materials used in water-splitting, which is beneficial for bulk diffusion processes involved during the reduction and oxidation steps. Additionally, the oxidation temperature must be sufficiently high to promote oxide ionic bulk diffusion, a key kinetic limitation of perovskite oxides. They investigated the capabilities of $La_xSr_{1-x}MnO_3$ (x = 0.8, 0.65, and 0.5) for the STCH reaction. Upon the substitution of Sr^{2+} for La^{3+}, an increase in the extent of reduction was observed due to charge imbalances, resulting in a higher nominal oxidation state on the B-site of the perovskite. This led to oxygen production yields of 112, 166, and 298 μmol g^{-1} for Sr^{2+} substitutions of 20%, 35%, and 50%, respectively. Furthermore, in the observed mixed Mn^{3+}/Mn^{4+} valence state, the higher the Mn^{4+} content, the greater the favorability for the reduction of the $La_{1-x}Sr_xMnO_{3-\delta}$. H_2 production yields of 124 and 195 μmol g^{-1} were observed for $La_{0.65}Sr_{0.35}MnO_{3-\delta}$ and $La_{0.5}Sr_{0.5}MnO_{3-\delta}$, respectively. These yields were attributed mainly to the strong capability of the perovskite structure to accommodate large oxygen vacancies upon reduction, allowing for considerable H_2 production. Ultimately, the thermal reduction and water-splitting capabilities of perovskites lie in the redox chemistry of the ABO_3 structure and in the B−O bond properties, such as the B atomic ionization potential, the B−O bond energy, or the orbital overlap between O 2p and B 3d states.[95] Similarly, Yang et al. studied the thermodynamics and kinetics of $La_{1-x}Sr_xMnO_{3-\delta}$ (x = 0.1, 0.2, 0.3, and 0.4). The authors noted several important factors: (1) Grain size decreased with increasing Sr^{2+} content, while porosity remained constant. (2) Oxygen release and hydrogen production exhibited monotonic increase with Sr^{2+} content, consistent with thermodynamic expectations. Nonetheless, there was an associated increase in the steam required for fuel production. (3) The kinetics of fuel production were significantly affected by the Sr^{2+} content. They also discovered that higher levels of strontium (Sr) doping led to reduced rates of steam-to-hydrogen conversion. Furthermore, with an increase in the Sr content, the rate of fuel production decreased, suggesting that intermediate compositions could provide the most favorable combination of properties. $La_{0.8}Sr_{0.2}MnO_{3-\delta}$ and $La_{0.6}Sr_{0.4}MnO_{3-\delta}$ exhibited consistent hydrogen and oxygen evolution over 21 and 8 consecutive test cycles, respectively. The former released an average of 64.7 μmol g^{-1} O_2 and produced 129.0 μmol g^{-1} H_2, while the latter released an average of 218.8 μmol g^{-1} O_2 and produced 397.3 μmol g^{-1} H_2, as shown in Figure 9.[91]

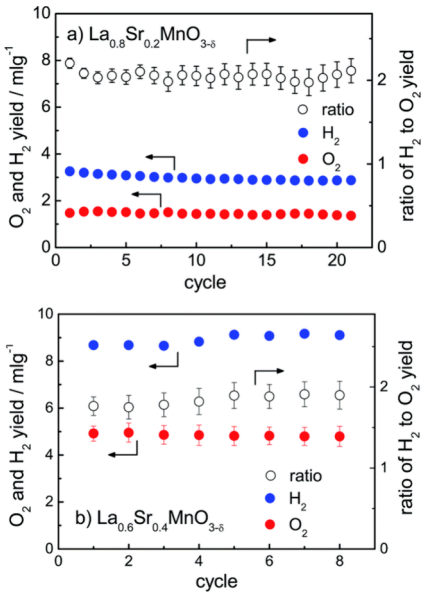

Figure 9. H_2 and O_2 production in $La_{0.8}Sr_{0.2}MnO_{3-\delta}$ and $La_{0.6}Sr_{0.4}MnO_{3-\delta}$, respectively. Reduction times for $La_{0.8}Sr_{0.2}MnO_{3-\delta}$ and $La_{0.6}Sr_{0.4}MnO_{3-\delta}$ were 47 and 70 min, and oxidation times were 16 and 65 min, respectively. The uncertainty is derived from calibration signal drift. Where omitted, error bars fall within the data symbol.[91] Reproduced with permission from ref 91. Copyright 2014 RSC Publishing.

In addition to the study of $La_{0.6}Sr_{0.4}MnO_3$ presented earlier, Luciani et al. also investigated $La_{0.6}Sr_{0.4}MnO_3$, which exhibited a tetragonal structure for STCH applications. Treatment of $La_{0.6}Sr_{0.4}MnO_3$ in a H_2 stream results in the coexistence of tetragonal and hexagonal phases, indicating that reduction in a hydrogen atmosphere induces a phase transition in the perovskite structure.[96] Later, Mara Orfila et al. investigated the STCH performance of two commercial perovskites with structure ABO_3: $La_{0.8}Sr_{0.2}MnO_{3-\delta}$ (LSM-20) and $La_{0.65}Sr_{0.35}MnO_{3-\delta}$ (LSM-35). They reveal a slight dependence between the reduction temperature and the strontium quantity within the structure. Higher strontium contents (as found in LSM-35) result in lower reduction temperatures compared to

https://doi.org/10.1021/acscatal.4c03357
ACS Catal. 2024, 14, 14974−15013

LSM-20, which has a lower strontium content. This result can be attributed to the higher quantity of strontium in the perovskite, which leads to the formation of more oxygen vacancies to maintain electroneutrality. This increase in the number of oxygen vacancies improves the oxygen mobility within the perovskite network, thereby facilitating the reduction process. H_2 production also increases with the doping level of Sr.[91,94,97] Alexander H. Bork et al. used data from Yang et al. as input to evaluate $La_{1-x}Sr_xMnO_{3-\delta}$ using the calculation of phase diagrams (CALPHAD) method. This method enables the description of multicomponent systems based on a physicochemical principle. In contrast to previous thermodynamic evaluations of perovskites, which relied on a single literature source and were constrained to a limited temperature range, the CALPHAD approach incorporates all relevant data available in the literature. Moreover, the CALPHAD results obtained are comparable to those obtained by Chih-Kai Yang et al. for H_2 production, with results of 116.1 and 392.9 μmol g^{-1} for $La_{0.8}Sr_{0.2}MnO_{3-\delta}$ and $La_{0.6}Sr_{0.4}MnO_{3-\delta}$, respectively.[98]

Additionally, Gager et al. discovered that porous $(La_{0.65}Sr_{0.35})_{0.95}MnO_{3-\delta}$ showed great promise as a catalyst for the STCH reaction. The use of porous ceramic foams offered several advantages, including a high specific area, significant porosity, and controlled permeability. The replica foams were carefully designed to have around 85% overall porosity, with about 65% of that being open porosity. Moreover, the foams retained their structure throughout 50 isothermal cycles at 1400 °C, while consistently yielding approximately 200 μmol g^{-1} of H_2.[99] In the field of STCH, besides delving into the impacts of doping, Lee et al. researched the effects of P_{H_2O}/P_{H_2} under isothermal cycling for $La_{0.65}Sr_{0.35}MnO_{3-\delta}$ and $La_{0.6}Sr_{0.4}MnO_{3-\delta}$. With P_{O_2} changes induced by changing P_{H_2O} relative to P_{H_2}, a general trend was observed for reduction extent, $\Delta\delta$, and H_2 production with increasing temperature and P_{O_2}, with $La_{0.65}Sr_{0.35}MnO_{3-\delta}$ producing 306.0 g mol^{-1} and $La_{0.6}Sr_{0.4}MnO_{3-\delta}$ producing 355.5 g mol^{-1} at 1400 °C.[91,100]

Later, Jonathan R. Scheffe's group conducted a study to investigate the morphological stability of $La_{0.6}Sr_{0.4}MnO_{3-\delta}$ during redox cycling using an infrared laser-based heating device. This device was employed to simulate the heat flux conditions expected in large-scale solar simulators. The study focused on these two porous materials and observed a correlation between the reaction extent and rates up to cycle 120, which was attributed to sintering and structural changes. In terms of water-splitting, the researchers found that ceria outperformed LSM40 due to LSM40's lower effectiveness at low P_{O_2} during the oxidation process. Moreover, the substitution of Sr^{2+} into the $LaMnO_{3-\delta}$ perovskite causes rhombohedral distortions in space group $R\bar{3}c$, generating a high concentration of Mn^{4+} due to the charge balance change induced by the replacement of La^{3+} with Sr^{2+}. Furthermore, a concentration of $Sr^{2+} \geq 47\%$ leads to a tetragonal structure ($I4/mcm$), and a concentration of $Sr^{2+} > 70\%$ leads to a cubic structure ($Pm3m$).[101]

The effect of Ca^{2+} doping into the lanthanum-manganite perovskite $La_{1-x}Ca_xMnO_{3-\delta}$ was also investigated. Sunita Dey et al. researched the impact of varying the Ca^{2+} content on $LaMnO_{3-\delta}$. They observed an increase in O_2 release with an increase in Ca^{2+} doping. Notably, $La_{0.5}Ca_{0.5}MnO_{3-\delta}$ produced 316.0 μmol g^{-1} of O_2, surpassing the production of the O_2 $La_{0.5}Sr_{0.5}MnO_{3-\delta}$ (201 μmol g^{-1}) and CeO_2 (63 μmol g^{-1}). Similarly, $La_{0.35}Ca_{0.65}MnO_{3-\delta}$ exhibited even higher O_2 production 653.0 μmol g^{-1}. During reoxidation, $La_{0.5}Sr_{0.5}MnO_{3-\delta}$ produced 308.0 μmol g^{-1} of H_2, while $La_{0.5}Ca_{0.5}MnO_{3-\delta}$ produced 407.0 μmol g^{-1} of H_2. This difference was attributed to the orthorhombic structure of Ca^{2+}-doped $LaMnO_{3-\delta}$, which exhibited superior activity compared to the rhombohedral structure of its Sr^{2+}-doped counterpart due to the former's distortion in the octahedral MnO_6. Additionally, the kinetics become sluggish with a high Ca^{2+} content.[102] A few months later, Dey et al. demonstrated the remarkable relationship between distortion and size disorder in relation to the H_2 yield of $Ln_{0.5}A_{0.5}MnO_3$ (Ln = Lanthanide, A = Ca^{2+}, Sr^{2+}). Accordingly, the O_2 released during the reduction step and the H_2 produced during the water-splitting step depend on the size of the lanthanide ion present at the A-site. As the size of the rare-earth ion decreases, the yields of O_2 and H_2 increase, with the onset temperature of oxygen evolution shifting to lower temperatures. This effect is attributed to small rare-earth ions, such as yttrium, having the highest lattice distortion and the smallest tolerance factor, indicating an increase in the tilting of the MnO_6 octahedra, which promotes the release of oxide ions. Specifically, a decrease in the tolerance factor leads to a significant reduction in the Mn−O−Mn bond angles, diminishing the spatial overlap between the Mn e_g and O 2pσ orbitals. The mismatch between the radii of the lanthanide ion and the alkaline-earth ion causes high site disorder where the oxygen is greatly displaced from the mean position, acting as the driving force for oxygen evolution. Thus, $Y_{0.5}Sr_{0.5}MnO_{3-\delta}$ and $Y_{0.5}Ca_{0.5}MnO_{3-\delta}$ released the highest amount of O_2, with 481.0 and 593.0 μmol g^{-1}, respectively. While $Y_{0.5}Ca_{0.5}MnO_{3-\delta}$ released the highest amount of O_2, $Y_{0.5}Sr_{0.5}MnO_{3-\delta}$ produced the highest amount of H_2 with 320.0 μmol g^{-1} versus 310.0 μmol g^{-1}.[103]

Lulu Wang et al. also investigated the effect of different Ca dopant levels on $LaMnO_{3-\delta}$. With increasing Ca^{2+} dopant levels, the temperature required to kick-start the evolution of the O_2 significantly decreased and the rate of release of the O_2 increased rapidly. Nevertheless, the trend for H_2 production performance was not in full accordance with the O_2 evolution trend, improving with Ca^{2+} dopant level from 0.2 to 0.4 and then decreasing thereafter. $La_{0.6}Ca_{0.4}MnO_3$ displays the highest hydrogen production (314 μmol g^{-1}) at the red./ox. temperature sof 1300 °C/900 °C and exhibits superior stability with stable hydrogen and oxygen production.[104] Subsequently, their research group elucidated a linear relationship between H_2 generation and the extent of oxygen vacancy (δ) in $La_{0.6}Sr_{0.4}BO_3$ (B = Cr, Mn, Fe, Co, and Ni).[105] Christopher L. Muhich et al. performed a thermodynamic analysis of six candidates. According to the solar-to-fuel conversion efficiency from high to low, the order follows Zr-doped CeO_2 > undoped CeO_2 > $La_{0.6}Ca_{0.4}MnO_3$ > $La_{0.6}Ca_{0.4}Mn_{0.6}Al_{0.4}O_3$ > $La_{0.6}Sr_{0.4}MnO_3$ > $La_{0.6}Sr_{0.4}Mn_{0.6}Al_{0.4}O_3$. This ranking is attributed to their relative reoxidizability and reducibility.[106]

Teruki Motohashi et al. investigated the effects of lanthanoid (Ln = La, Nd, Gd, Y) substitution on $BaLnMn_2O_{5+\delta}$, an A-site-ordered double perovskite. Interestingly, they observed that the water-splitting reaction occurs only once the oxygen content in the sample is less than oxygenated $O_{5.5}$. This points to the exclusive activity of Mn^{2+}, while Mn^{3+} and Mn^{4+} remain

https://doi.org/10.1021/acscatal.4c03357
ACS Catal. 2024, 14, 14974−15013

Table 2. STCH Performance of Mn-Based Perovskite Oxides under Reducing Gas Conditions

composition	synthesis method	cycles	$\Delta\delta$	temp. red./ox. (°C)	time red./ox. (min)	H_2O (%vol)	gas red./ox.	H_2 yield (μmol g^{-1})	average H_2 production rate (μmol g^{-1} min^{-1})	ref
$BaYMn_2O_{5+\delta}$	citrate/encapsulation	1	0.5	500/500	-/150	2.3	N_2-H_2/N_2	14.3[a]		107
$BaGdMn_2O_{5+\delta}$	citrate/encapsulation	1	0.5	500/500	-/17500	2.3	N_2-H_2/N_2	646.7[a]		107
$BaNdMn_2O_{5+\delta}$	citrate/encapsulation	1	0.5	500/500	-/2000	2.3	N_2-H_2/N_2	1064.6[a]		107
$BaLaMn_2O_{5+\delta}$	citrate/encapsulation	1	0.5	500/500	-/1500	2.3	N_2-H_2/N_2	1093.2[a]	0.73	107
$(La_{0.65}Sr_{0.35})_{0.95}MnO_{3-\delta}$	commercial	50	0.05	1400/1400	30/10		$Ar-H_2$/Ar	200.0	6.67	99
$La_{0.65}Sr_{0.35}MnO_{3-\delta}$	commercial	1	0.092	1300/1300		24.82	$Ar-H_2$[b]/$Ar-H_2$	147.5		92
$La_{0.65}Sr_{0.35}MnO_{3-\delta}$	commercial	1	0.115	1350/1350		24.82	$Ar-H_2$[b]/$Ar-H_2$	234.5		92
$La_{0.65}Sr_{0.35}MnO_{3-\delta}$	commercial	1	0.131	1400/1400		24.82	$Ar-H_2$[b]/$Ar-H_2$	306.0		92
$La_{0.6}Sr_{0.4}MnO_{3-\delta}$	Pechini	1	0.087	1300/1300		24.82	$Ar-H_2$[b]/$Ar-H_2$	156.0		92
$La_{0.6}Sr_{0.4}MnO_{3-\delta}$	Pechini	1	0.123	1350/1350		24.82	$Ar-H_2$[b]/$Ar-H_2$	273.0		92
$La_{0.6}Sr_{0.4}MnO_{3-\delta}$	Pechini	1	0.144	1400/1400		24.82	$Ar-H_2$[b]/$Ar-H_2$	355.5		92

[a]Value converted from mL $g_{material}^{-1}$. Standard volume occupied: 22400 mL mol^{-1}). [b]Steam injected during reduction step. 1300 °C ≈ 11.66 vol % H_2O, 1350 °C ≈ 6.69 vol % H_2O, 1400 °C ≈ 4.05 vol % H_2O.

inactive. Additionally, the reoxygenation rate from $O_{5.0}$ to $O_{5.5}$ is influenced by an increase in coordination number at the Ln^{3+} site. Larger Ln members (e.g., La^{3+}) exhibit greater stability in the deoxygenated $O_{5.0}$ form, resulting in a higher endothermic oxygenation enthalpy and stronger reductive reactivity. Consequently, $BaLaMn_2O_{5+\delta}$ exhibited the highest H_2 production (1093.2 μmol g^{-1}) and the shortest reduction time. As the Ln^{3+} size decreased, H_2 production decreased and reduction time increased, culminating with $BaYMn_2O_{5+\delta}$ showing almost undetectable H_2 production (14.3 μmol g^{-1}). These differences in reactivity might be explained by considering electrostatic interactions within the crystal lattice.[107]

Débora R. Barcellos et al. discovered a Ruddlesden−Popper phase layered perovskite, $Ce_xSr_{2-x}MnO_4$, and its applicability for STCH through DTF calculations. Accordingly, the suitability of an oxide for STCH is tied to the energy required to create and fill oxygen vacancies during the STCH cycling. The oxygen vacancy formation energy, E_v, directly impacts the driving force for oxide reoxidation in the presence of steam and must be low enough to allow a feasible level of non-stoichiometry during reduction, yet high enough to overcome the O−H bond strength of water during oxidation. Through DFT calculations, the oxygen vacancy formation energy of $Ce_xSr_{2-x}MnO_4$ was computed to range from 1.8 to 2.7 eV, implying its good suitability for water-splitting (1.5−5 eV). Coupled with the enhanced oxygen ion mobility characteristic of layered perovskites, $Ce_xSr_{2-x}MnO_4$ demonstrated complete redox reversibility, with $Ce_{0.1}Sr_{1.9}MnO_4$ having an oxygen release of 240.0 μmol g^{-1}, $Ca_{0.2}Sr_{1.8}MnO_4$ having a release of 168.0 μmol g^{-1}, and $Ca_{0.3}Sr_{1.7}MnO_4$ having a release of 129.0 μmol g^{-1}, equating to hydrogen productions of 218.0, 247.0, and 166.0 μmol g^{-1}, respectively. Conversely, $Ce_{0.1}Sr_{1.9}MnO_4$ had the lowest oxygen vacancy formation energy and thus had the largest oxygen evolution, while $Ca_{0.3}Sr_{1.7}MnO_4$ had the highest oxygen vacancy formation energy but the lowest oxygen evolution. Nevertheless, $Ca_{0.2}Sr_{1.8}MnO_4$ had the highest H_2 production because it balanced a moderate extent of reduction with an adequate driving force by having an intermediate oxygen vacancy formation energy.[108]

Recently, Bergenson-Keller et al. compared the work of Débora R. Barcellos et al. on the Ruddlesden−Popper layered perovskite $Ce_xSr_{2-x}MnO_4$ with the perovskite $Sr_{1-x}Ce_xMnO_{3-\delta}$. $SrMnO_{3-\delta}$ presented several phase transitions due to the concentration of Ce^{2+} used, starting off as hexagonal ($P6_3/mmc$), cubic (Pm3m) at 5 mol % Ce^{2+}, tetragonal ($I4/mcm$) at 8 mol % Ce^{2+}, and orthorhombic ($Imma$) at 35 mol % Ce^{2+}. At elevated temperatures, samples with ≤30 mol % Ce^{2+} transitioned to the $Pm3m$ phase, while samples with 40 mol % Ce^{2+} transitioned to $I4/mcm$ and then to $Pm3m$. The cerium-doped strontium manganite perovskite and its Ruddlesden−Popper counterpart demonstrated opposite trends for H_2 production with an increasing Ce^{2+} content. $Sr_{0.8}Ce_{0.2}MnO_{3-\delta}$ produced the lowest H_2 yield at 220.0 μmol g^{-1}, while $Sr_{0.7}Ce_{0.3}MnO_{3-\delta}$ produced the highest at 305.0 μmol g^{-1}, yet $Ce_{0.2}Sr_{1.8}MnO_{3-\delta}$ produced the highest at 247.0 μmol g^{-1} and $Ce_{0.3}Sr_{1.7}MnO_{3-\delta}$ produced the lowest at 166.0 μmol g^{-1} for their respective families. While the Ruddlesden−Popper family was expected to outperform its perovskite counterpart based on thermal reduction screening, the results proved otherwise. This was attributed to possible variability within the morphology or secondary-phase distribution within each sample and/or viability in the testing procedure, since both families were tested a year apart from each other. Moreover, the authors stress that under a local steam-to-hydrogen ratio deviation from pure steam conditions of 10 000:1, the hydrogen production of $Sr_{1-x}Ce_xMnO_{3-\delta}$ would be suppressed from that of $Ce_xSr_{2-x}MnO_4$. Nevertheless, a direct correlation between structure, Ce^{2+} content, and H_2 yield could not be discerned.[109] Table 1 summarizes the STCH performance of Mn-based perovskite oxides under inert gas conditions.

Table 2 summarizes the STCH performance of Mn-based perovskite oxides under reducing gas conditions.

https://doi.org/10.1021/acscatal.4c03357
ACS Catal. 2024, 14, 14974−15013

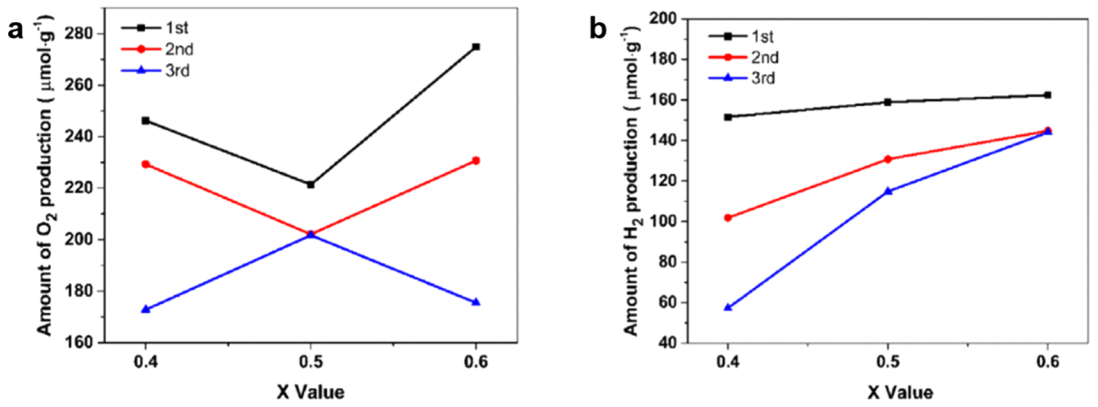

Figure 10. (a) The oxygen production and (b) the hydrogen production over three consecutive cycles for $La_{0.4}Sr_{0.6}Mn_{1-x}Al_x$ (x = 0.4, 0.5, and 0.6).[115] Reproduced with permission from ref 115. Copyright 2022 Elsevier.

5.2. MnAl-Based Perovskite Oxides as Redox-Active Oxygen Exchange Materials. As mentioned previously, La−Mn perovskites often exhibit incomplete reoxidation. However, doping with aluminum (Al) at the B-site can enhance the efficiency of reoxidation and increase the extent of reduction.[112] For example, McDaniel et al. investigated three perovskites ($La_{0.4}Sr_{0.6}Mn_{0.6}Al_{0.4}O_{3-\delta}$, $La_{0.6}Sr_{0.4}Mn_{0.6}Al_{0.4}O_{3-\delta}$, and $La_{0.4}Sr_{0.6}Mn_{0.4}Al_{0.6}O_{3-\delta}$) in the field of STCH and demonstrated that it is possible to achieve significant improvements in redox capacity and a dramatic increase in redox thermodynamics by tuning the combination of Mn and Al on the B-site of the perovskite structure. Lanthanum aluminate is known to remain stable in both oxidizing and reducing environments due to its cations maintaining a consistent oxidation state. McDaniel et al. introduced redox activity and increased the extent of reduction by doping Mn^{2+}/Mn^{3+}/Mn^{4+} on the B-site and Sr^{2+} on the A-site of $LaAlO_{3-\delta}$. $La_{0.6}Sr_{0.4}Mn_{0.6}Al_{0.4}O_{3-\delta}$ (known as LSMA6464) produced 307.0 μmol g^{-1} of H_2, surpassing the production of 220.0 μmol g^{-1} achieved by $La_{0.6}Sr_{0.4}Mn_{0.4}Al_{0.6}O_{3-\delta}$ through a 40% to 60% increase in Mn content. This indicates the importance of Mn inducing higher redox activity. In contrast, $La_{0.4}Sr_{0.6}Mn_{0.6}Al_{0.4}O_{3-\delta}$ produced 277.0 μmol g^{-1} of H_2, indicating the negative effect of introducing high amount of Sr^{2+} doping on the A-site.[77,113] Ann M. Deml et al. put forward the sensitivity of oxygen vacancy formation energies (E_v) to composition. In the $Sr_xLa_{1-x}Mn_yAl_{1-y}O_3$ composition spectrum, E_v spans a wide range from near 0 to over 3 eV, offering significant control over the V_o formation energetics and redox properties. They observe that E_v decreases with higher Sr mole fractions (χSr) and either increases or remains constant with increasing Mn mole fractions (χMn). As a result, compositions with lower χSr and higher χMn tend to have higher E_v. Additionally, they also used density functional theory (DFT) to identify LSMA6464 as an optimal LSMA composition.[114] M. Ezbiri et al. reported that perovskites typically show decreasing enthalpy changes as nonstoichiometry increases, with the most pronounced effect observed in LSMA6464, making it an attractive candidate for H_2O splitting.[87] Furthermore, they also measured the equilibrium thermodynamics of $La_{0.6}Ca_{0.4}Mn_{0.8}Al_{0.2}O_{3-\delta}$ and the perovskite family $La_xSr_{1-x}Mn_yAl_{1-y}O_{3-\delta}$ ($0 \le x \le 1$, $0 \le y \le 1$) in the temperature range from 1573 to 1773 K and from 0.206 to 180 mbar O_2, demonstrating a tunable reduction extent that increases with higher Sr content.[87] Additionally, Aldo Steinfeld's group measured the oxygen nonstoichiometry of $La_{0.6}A_{0.4}Mn_{1-y}Al_yO_3$ (A = Ca, Sr, and y = 0, 0.4) under the same temperature conditions as M. Ezbiri et al. and at a range of P_{O_2} from 4.5066×10^{-2} to 9.9×10^{-5} bar. They discovered that the oxygen nonstoichiometry is higher when the Sr^{2+} is replaced with Ca^{2+} in $La_{0.6}Sr_{0.4}MnO_3$, but it also notably increases when 40 mol % Al is doped into the Mn-site.[25] Berke Piskin's group also investigated Al-substituted $La_{0.4}Sr_{0.6}Mn_{1-x}Al_xO_3$ (x = 0.4, 0.5, and 0.6). The samples were studied through three continuous thermochemical cycles at reduction/oxidation temperatures of 1350 °C/800 °C. LSMA4646 exhibited the highest H_2 and O_2 production of 144 μmol g^{-1} and 275 μmol g^{-1}, respectively. This study suggested that increasing the amount of Al can improve hydrogen and oxygen production (as presented in Figure 10), as well as the reoxidation capacity, and enhance structural stability during redox cycling.[115]

In addition, Ezbiri et al. conducted an extensive characterization of the reduction extent capacity of $La_{1-x}Sr_xMn_yAl_{1-y}O_{3-\delta}$ perovskites. They observed an increase in oxygen nonstoichiometry with the increase in Sr^{2+} while keeping Al^{3+} constant. However, when Al^{3+} was varied while Sr^{2+} was kept constant, no significant change was observed. The authors also noted the presence of Mn^{2+} surface enrichment in all compositions except for $La_{0.8}Sr_{0.2}Mn_{0.8}Al_{0.2}O_{3-\delta}$ and $La_{0.8}Sr_{0.2}Mn_{0.2}Al_{0.8}O_{3-\delta}$, which were the two samples with the lowest oxygen nonstoichiometry. While this observation indicates the redox activity of Mn, samples with a large reduction extent did not necessarily contain a large concentration of Mn^{2+}, indicating no correlation between the two. In the absence of Al, Sr surface enrichment occurs rather than Mn enrichment. Ultimately, Mn ions were found to be the redox-active sites for reduction, with Al-doping leading to Mn cation surface enrichment, which are the main enhancers of the reduction extent of Al-doped $La_{1-x}Sr_xMnO_{3-\delta}$ and $La_{1-x}Ca_xMnO_{3-\delta}$.[116]

Consequently, Wang et al. continued to characterize $La_{1-x}Ca_xMn_{1-y}Al_yO_{3-\delta}$ for water-splitting applications. Samples with varying Ca^{2+} content (i.e., $La_{1-x}Ca_xMn_{0.6}Al_{0.4}O_{3-\delta}$) had an improved O_2 evolution performance with a positive linear trend and a lower onset temperature for O_2 evolution with increasing Ca^{2+} concentration. However, H_2 production peaked at 40% Ca^+ content and decreased thereafter in a parabola-shaped trend. This anomaly is attributed to the detrimental effect of high Ca content on the thermodynamic

https://doi.org/10.1021/acscatal.4c03357
ACS Catal. 2024, 14, 14974−15013

Table 3. STCH Performance of MnAl-Based Perovskite Oxides under Inert Gas Conditions

composition	synthesis method	cycles	$\Delta\delta$	temp. red./ox. (°C)	time red./ox. (min)	H_2O (% vol)	gas red./ox.	O_2 yield (μmol g^{-1})	H_2 yield (μmol g^{-1})	average H_2 production rate (μmol g^{-1} min^{-1})	ref
$La_{0.6}Sr_{0.4}Mn_{0.6}Al_{0.4}O_{3-\delta}$	modified Pechini	1	0.15	1400/-			Ar/O_2				112
$La_{0.6}Ca_{0.4}Mn_{0.6}Al_{0.4}O_{3-\delta}$	Modified Pechini	1	0.13	1400/-			Ar/O_2				112
$La_{0.4}Sr_{0.6}Mn_{0.6}Al_{0.4}O_{3-\delta}$;	modified Pechini	1		1350/1000		40.0	He/He		307.0		77, 113
$La_{0.6}Sr_{0.4}Mn_{0.6}Al_{0.4}O_{3-\delta}$;	modified Pechini	1		1350/1000		40.0	He/He		277.0		77, 113
$La_{0.4}Sr_{0.6}Mn_{0.4}Al_{0.6}O_{3-\delta}$	modified Pechini	1		1350/1000		40.0	He/He		220.0		77, 113
$La_{0.8}Ca_{0.2}Mn_{0.6}Al_{0.4}O_3$	sol−gel	1		1400/1000	60/60	40.0	Ar/Ar	176.0	334.0	5.57	99
$La_{0.6}Ca_{0.4}Mn_{0.6}Al_{0.4}O_3$	sol−gel	1		1400/1000	60/60	40.0	Ar/Ar	231.0	429.0	7.15	99
$La_{0.4}Ca_{0.6}Mn_{0.6}Al_{0.4}O_3$	sol−gel	1		1400/1000	60/60	40.0	Ar/Ar	280.0	364.0	6.07	99
$La_{0.2}Ca_{0.8}Mn_{0.6}Al_{0.4}O_3$	sol−gel	1		1400/1000	60/60	40.0	Ar/Ar	419.0	260.0	4.33	99
$La_{0.6}Ca_{0.4}Mn_{0.8}Al_{0.2}O_{3-\delta}$	Pechini	1		1300/900	60/60	40.0	Ar/Ar	184.0	339.0	5.65	110
$La_{0.8}Sr_{0.2}Mn_{0.8}Al_{0.2}O_{3-\delta}$	Pechini	1	0.034	1350/-	225/-		Ar/-				116
$La_{0.6}Sr_{0.4}Mn_{0.8}Al_{0.2}O_{3-\delta}$	Pechini	1	0.116	1350/-	225/-		Ar/-				116
$La_{0.4}Sr_{0.6}Mn_{0.8}Al_{0.2}O_{3-\delta}$	Pechini	1	0.270	1350/-	225/-		Ar/-				116
$La_{0.2}Sr_{0.8}Mn_{0.8}Al_{0.2}O_{3-\delta}$	Pechini	1	0.351	1350/-	225/-		Ar/-				116
$La_{0.8}Sr_{0.2}Mn_{0.6}Al_{0.4}O_{3-\delta}$	Pechini	1	0.028	1350/-	225/-		Ar/-				116
$La_{0.6}Sr_{0.4}Mn_{0.6}Al_{0.4}O_{3-\delta}$	Pechini	1	0.171	1350/-	225/-		Ar/-				116
$La_{0.4}Sr_{0.6}Mn_{0.6}Al_{0.4}O_{3-\delta}$	Pechini	1	0.208	1350/-	225/-		Ar/-				116
$La_{0.8}Sr_{0.2}Mn_{0.4}Al_{0.6}O_{3-\delta}$	Pechini	1	0.035	1350/-	225/-		Ar/-				116
$La_{0.6}Sr_{0.4}Mn_{0.4}Al_{0.6}O_{3-\delta}$	Pechini	1	0.134	1350/-	225/-		Ar/-				116
$La_{0.8}Sr_{0.2}Mn_{0.2}Al_{0.8}O_{3-\delta}$	Pechini	1	0.049	1350/-	225/-		Ar/-				116
$La_{0.6}Ca_{0.4}Mn_{0.6}Al_{0.4}O_{3-\delta}$	Pechini	1	0.153	1350/-	225/-		Ar/-				116
$La_{0.6}Ca_{0.4}Mn_{0.8}Al_{0.2}O_{3-\delta}$	Pechini	1		1400/1000	60/60	40.0	Ar/Ar	201.0	374.0	0	117
$La_{0.8}Ca_{0.2}Mn_{0.6}Al_{0.4}O_{3-\delta}$	Pechini	1		1400/1000	60/60	40.0	Ar/Ar	176.0	334.0	0	117
$La_{0.6}Ca_{0.4}Mn_{0.6}Al_{0.4}O_{3-\delta}$	Pechini	5		1400/1000	60/60	40.0	Ar/Ar	231.0	429.0	0	117
$La_{0.4}Ca_{0.6}Mn_{0.6}Al_{0.4}O_{3-\delta}$	Pechini	1		1400/1000	60/60	40.0	Ar/Ar	280.0	364.0	0	117
$La_{0.2}Ca_{0.8}Mn_{0.6}Al_{0.4}O_{3-\delta}$	Pechini	1		1400/1000	60/60	40.0	Ar/Ar	419.0	260.0	0	117
$La_{0.6}Ca_{0.4}Mn_{0.4}Al_{0.6}O_{3-\delta}$	Pechini	1		1400/1000	60/60	40.0	Ar/Ar	186.0	349.0	0	117
$La_{0.6}Ca_{0.4}Mn_{0.2}Al_{0.8}O_{3-\delta}$	Pechini	1		1400/1000	60/60	40.0	Ar/Ar	126.0	239.0	0	117
$La_{0.9}Sr_{0.1}Mn_{0.9}Al_{0.1}O_{3-\delta}$	Pechini	3		1350/1000	1/60	84.0	N_2/N_2	55.2[a]	72.1[a]	0	90
$La_{0.8}Sr_{0.2}Mn_{0.8}Al_{0.2}O_{3-\delta}$	Pechini	3		1350/1000	1/60	84.0	N_2/N_2	85.2[a]	76.8[a]	0	90
$La_{0.7}Sr_{0.2}Mn_{0.7}Al_{0.3}O_{3-\delta}$	Pechini	3		1350/1000	1/60	84.0	N_2/N_2	107.5[a]	125.0[a]	0	90
$La_{0.3}Sr_{0.7}Mn_{0.7}Al_{0.3}O_{3-\delta}$	Pechini	2		1350/1000	1/60	50.0	N_2/N_2	674.1[a]	69.3[a]	0	90
$La_{0.3}Sr_{0.7}Mn_{0.7}Al_{0.3}O_{3-\delta}$	Pechini	1		1350/1000	1/60	84.0	N_2/N_2		116.1[a]	1.94	90
$La_{0.6}Sr_{0.4}Mn_{0.6}Al_{0.4}O_{3-\delta}$	Pechini	3		1350/1000	1/60	84.0	N_2/N_2	103.4[a]	58.7[a]	0.98	90
$La_{0.4}Sr_{0.6}Mn_{0.6}Al_{0.4}O_{3-\delta}$	Pechini	2		1350/1000	1/60	50.0	N_2/N_2	535.7[a]	75.7[a]	1.26	90
$La_{0.4}Sr_{0.6}Mn_{0.6}Al_{0.4}O_{3-\delta}$	Pechini	1		1350/1000	1/60	84.0	N_2/N_2		147.3[a]	2.46	90
$La_{0.5}Sr_{0.5}Mn_{0.5}Al_{0.5}O_{3-\delta}$	Pechini	2		1350/1000	1/60	50.0	N_2/N_2	405.5[a]	129.5[a]	2.16	90
$La_{0.5}Sr_{0.5}Mn_{0.5}Al_{0.5}O_{3-\delta}$	Pechini	1		1350/1000	1/60	84.0	N_2/N_2		129.5[a]	2.16	90

https://doi.org/10.1021/acscatal.4c03357
ACS Catal. 2024, 14, 14974−15013

Table 3. continued

composition	synthesis method	cycles	$\Delta\delta$	temp. red./ox. (° C)	time red./ox. (min)	H_2O (% vol)	gas red./ox.	O_2 yield (μmol g^{-1})	H_2 yield (μmol g^{-1})	average H_2 production rate (μmol g^{-1} min^{-1})	ref
$La_{0.6}Sr_{0.4}Mn_{0.4}Al_{0.6}O_{3-\delta}$	Pechini	2		1350/1000	1/60	50.0	N_2/N_2	338.5[a]	66.5[a]	1.11	90
$La_{0.7}Sr_{0.3}Mn_{0.3}Al_{0.7}O_{3-\delta}$	Pechini	2		1350/1000	1/60	50.0	N_2/N_2	156.3[a]	22.3[a]	0.37	90
$La_{0.6}Sr_{0.4}Mn_{0.6}Al_{0.4}O_{3-\delta}$	Pechini	3	0.086	1400/1000	5.5/20	40.0	Ar/Ar		292.0	14.60	26
$La_{0.6}Sr_{0.4}Mn_{0.6}Al_{0.4}O_{3-\delta}$	Pechini	1		1400/850	5.5/20	40.0	Ar/Ar		256.0	12.80	26
$La_{0.6}Sr_{0.4}Mn_{0.6}Al_{0.4}O_{3-\delta}$	Pechini	1		1400/750	5.5/20	40.0	Ar/Ar		205.0	10.25	26
$La_{0.6}Sr_{0.4}Mn_{0.6}Al_{0.4}O_{3-\delta}$	Pechini	1		1350/1000	5.5/20	40.0	N_2/N_2		224.0	11.20	26
$La_{0.6}Sr_{0.4}Mn_{0.6}Al_{0.4}O_{3-\delta}$	Pechini	3		1350/850	5.5/20	40.0	Ar/Ar	163.0	194.0	9.70	26
$La_{0.6}Sr_{0.4}Mn_{0.6}Al_{0.4}O_{3-\delta}$	Pechini	1		1350/850	5.5/20	40.0	Ar/Ar−H_2[b]		54.7	2.74	26
$La_{0.6}Sr_{0.4}Mn_{0.6}Al_{0.4}O_{3-\delta}$	Pechini	1		1350/850	5.5/20	40.0	Ar/Ar−H_2[c]		32.4	1.62	26
$La_{0.6}Sr_{0.4}Mn_{0.6}Al_{0.4}O_{3-\delta}$	Pechini	1		1350/850	5.5/20	40.0	Ar/Ar−H_2[d]		27.7	1.39	26
$La_{0.6}Sr_{0.4}Mn_{0.6}Al_{0.4}O_{3-\delta}$	Pechini	1		1350/850	5.5/20	40.0	Ar/Ar−H_2[e]		2.4	0.12	26
$La_{0.6}Sr_{0.4}Mn_{0.6}Al_{0.4}O_{3-\delta}$	Pechini	1		1350/850	5.5/20	40.0	Ar/Ar−H_2[f]		0.0	0	26
$La_{0.6}Sr_{0.4}Mn_{0.6}Al_{0.4}O_{3-\delta}$	Pechini	1		1350/750	5.5/20	40.0	Ar/Ar		150.0	7.50	26
$La_{0.6}Sr_{0.4}Mn_{0.6}Al_{0.4}O_{3-\delta}$	Pechini	1		1250/1000	5.5/20	40.0	Ar/Ar		105.0	5.25	26
$La_{0.6}Sr_{0.4}Mn_{0.6}Al_{0.4}O_{3-\delta}$	Pechini	1		1250/850	5.5/20	40.0	Ar/Ar		89.0	4.45	26
$La_{0.6}Sr_{0.4}Mn_{0.6}Al_{0.4}O_{3-\delta}$	Pechini	1		1250/750	5.5/20	40.0	Ar/Ar		74.0	3.70	26
$La_{0.6}Sr_{0.4}Mn_{0.6}Al_{0.4}O_{3-\delta}$	Combustion	3	0.040	1350/800	40/-	100.0	Ar/-	103.0	254.0		119

[a]Value converted from mL $g_{material}^{-1}$ (Ncm^3 $g_{material}^{-1}$). Standard volume occupied: 22400 mL mol^{-1}). [b]$H_2O:H_2$ = 1333. [c]$H_2O:H_2$ = 1000. [d]$H_2O:H_2$ = 750. [e]$H_2O:H_2$ = 500. [f]$H_2O:H_2$ = 285.

https://doi.org/10.1021/acscatal.4c03357
ACS Catal. 2024, 14, 14974−15013

Table 4. STCH Performance of MnAl-Based Perovskite Oxides under Reducing Gas Conditions

composition	synthesis method	cycles	$\Delta\delta$	temp. red./ox. (°C)	time red./ox. (min)	gas red./ox.	average H_2 production rate (μmol g^{-1} min^{-1})	ref
$Y_{0.8}Sr_{0.2}Mn_{0.6}Al_{0.4}O_{3-\delta}$	Pechini	8	0.3925	900/900	1/5	[a]Ar−H_2/Ar−O_2	0	118
$Y_{0.8}Sr_{0.2}Mn_{0.4}Al_{0.6}O_{3-\delta}$	Pechini	8	0.3319	900/900	1/5	[a]Ar−H_2/Ar−O_2	0	118
$Y_{0.9}Sr_{0.1}Mn_{0.6}Al_{0.4}O_{3-\delta}$	Pechini	8	0.3388	900/900	1/5	[a]Ar−H_2/Ar−O_2	0	118

[a]Injection of Ar−H_2 (P_{H_2} = 0.01 atm) began at 300 °C. Injection of Ar−O_2 (P_{O_2} = 0.15 atm) continued with cooldown to 300 °C.

water-splitting, since only 30% of the O_2 released with 80% Ca^{3+} content was recovered. Accordingly, a maximum O_2 evolution of 419.0 μmol g^{-1} was achieved by $La_{0.2}Ca_{0.6}Mn_{0.6}Al_{0.4}O_{3-\delta}$, and a maximum H_2 production of 429.0 μmol g^{-1} was achieved by $La_{0.6}Ca_{0.4}Mn_{0.6}Al_{0.4}O_{3-\delta}$. Thereafter, the authors varied the Al^{3+} content while maintaining the 40% Ca^{3+} content (i.e., $La_{0.6}Ca_{0.4}Mn_{1-y}Al_yO_{3-\delta}$), with O_2 release and H_2 production increasing with increasing Al^{3+} up until 40% Al^{3+} content and decreasing thereafter. The variation of Al^{3+} had a slight effect on the thermodynamics of the perovskite, as all samples had high reoxidation yields.[117] As mentioned in the previous section, Lulu Wang et al. also sought enhancement by substituting Mn^{3+} with a Al^{3+} metal ion on the B-site, resulting in an enhanced oxygen release of 184.0 and H_2 production of 339.0 μmol g^{-1} for $La_{0.6}Ca_{0.4}Mn_{0.8}Al_{0.2}O_{3-\delta}$.[110] Moreover, Aldo Steinfeld's group investigated the solar-to-fuel energy conversion efficiency of $La_{0.6}Ca_{0.4}Mn_{0.6}Al_{0.4}O_3$ (LCMA) and $La_{0.6}Sr_{0.4}Mn_{0.6}Al_{0.4}O_3$ (LSMA) and uncovered that investigated materials were more or less sensitive to different parameters, where LCMA and LSMA are associated with gas−gas heat recuperation.[106]

Moreover, Gokon et al. investigated the effects of concurrent Sr^{2+} and Mn ion substitution in $La_{1-x}Sr_xMn_xAl_{1-x}O_{3-\delta}$ and concurrent Sr^{2+} and Al^{3+} ion substitution in $La_{1-y}Sr_yMn_{1-y}Al_yO_{3-\delta}$ on oxygen release and H_2 production for thermochemical water-splitting. Accordingly, in $La_{1-x}Sr_xMn_xAl_{1-x}O_{3-\delta}$ the concurrent increasing substitution of Sr^{2+} and Mn ions caused the formation of lattice defects in the perovskite structure due to changes in the charge neutrality, which enhanced oxygen release during reduction due to the reaction mechanism involving the Mn^{4+} to Mn^{3+} reduction transition. Under the first thermochemical cycle, 156.3−674.1 μmol g^{-1} of O_2 was released by the samples, with the amount increasing with the concurrent increase of Sr^{2+} and Mn ion content, corresponding to a H_2 production of 22.3−129.5 μmol g^{-1} with the maximum occurring at x = 0.5. The disparity between the release of the O_2 and the production of the H_2 deals with the different mechanisms for each: O_2 release from a perovskite oxide is an oxygen diffusion process of surface-to-bulk and bulk-to-bulk from the material to an inert atmosphere, while H_2 production is a chemical reaction of the reduced perovskite oxide with steam. Thus, the samples are not fully reversible.[90] Recently, Carrillo et al. investigated the oxygen nonstoichiometry and defect equilibria of $Y_{1-x}Sr_xMn_{1-y}Al_yO_{3-\delta}$ though reduction experiments conducted at different P_{O_2} and temperatures, testing them against the Mn^{4+}/Mn^{3+} and Mn^{4+}/Mn^{2+} defect models. Accordingly, under low P_{O_2}, both models fail to fit the reduction extent data of $Y_{0.8}Sr_{0.2}Mn_{0.6}Al_{0.4}O_{3-\delta}$ and $Y_{0.9}Sr_{0.1}Mn_{0.6}Al_{0.4}O_{3-\delta}$. Yet, under high P_{O_2}, both model predictions fit well for $Y_{0.8}Sr_{0.2}Mn_{0.6}Al_{0.4}O_{3-\delta}$. The authors attribute this disagreement between the models and the data obtained under low P_{O_2} to changes in the crystal structure (phase impurities) observed after cycling. Furthermore, for $Y_{0.8}Sr_{0.2}Mn_{0.4}Al_{0.6}O_{3-\delta}$, the Mn^{4+}/Mn^{3+} model succeeded for all measured data under all temperate conditions, under both low and high P_{O_2}. The authors concluded that the $Y_{1-x}Sr_xMn_{1-y}Al_yO_{3-\delta}$ perovskites are not ideal candidates for STCH due to their low sensitivity to reduction under changes in P_{O_2}. They also state that these samples require a substantial excess of oxidant to achieve high reoxidation rates and hydrogen (H_2) production.[118] Table 3 presents a detailed overview of STCH performance of MnAl-based perovskite oxides under inert gas conditions.

Table 4 presents an overview of the STCH performance of MnAl-based perovskite oxides under reducing gas conditions.

5.3. MnX-Based Perovskite Oxides As Redox-Active Oxygen Exchange Materials. In addition to investigating Al doping in the Mn site, researchers have also explored doping with other elements (X = Ce, Sc, Ga, Cr, Fe, Co, Ti, and Mg) in the Mn site. For example, Ryan P. O'Hayre's group discovered that $BaCe_{0.25}Mn_{0.75}O_3$ (BCM) exhibits nearly three times the amount of hydrogen compared to ceria when reduced at 1350 °C. Furthermore, this material demonstrates a greater tendency for H_2O splitting and faster oxidation kinetics compared to the Mn-based perovskite $La_{1-x}Sr_xMn_yAl_{1-y}$ (x, y = 0.4, 0.6).[26] Additionally, Trindell et al. also investigated the potential of $BaCe_{0.25}Mn_{0.75}O_3$ (BCM) as an active material for solar thermochemical processes. Previous studies on BCM have faced challenges due to the presence of secondary phases, which hindered the analysis of stability and performance. This study presents two synthesis approaches for producing nearly single-phase samples of BCM: solid-state and sol−gel routes. It demonstrates that both methods can yield a high-purity 12R hexagonal perovskite phase of BCM (>97 wt %). The study also examines the anisotropy of thermal expansion in BCM and investigates the impact of high-temperature redox cycling on its stability and phase fraction. The results provide valuable insights into the synthesis and performance of BCM for solar thermochemical applications.[120] In addition, the 12R hexagonal perovskite structure of BCM exhibits an interesting characteristic wherein it tends to partially transform into a 6H polytype when exposed to high temperatures and reducing environments. This transformation occurs during the initial stage of the thermochemical cycle and can help to prevent the degradation of this complex oxide material. An analogous compound, $BaNb_{0.25}Mn_{0.75}O_3$ (BNM), which also possesses a 12R structure, was successfully synthesized. Remarkably, BNM undergoes almost complete conversion into the 6H structure under the same reaction conditions as BCM.[121] Moreover, Roychoudhury et al. investigated the electronic structure of $BaCe_{0.25}Mn_{0.75}O_{3-\delta}$ before and after thermal reduction using a

https://doi.org/10.1021/acscatal.4c03357
ACS Catal. 2024, 14, 14974−15013

combination of experimental K-edge X-ray absorption spectroscopy (XAS) and first-principles calculations. The computed projected density of states (PDOS) and orbital plots propose a simplified model that elucidates the interaction between oxygen and metal atoms within the material. Experimental measurements confirm a noticeable reduction in the intensity of the first peak in the O K-edge spectrum for the reduced crystal due to oxygen removal.[122]

Debora R. Barcellos et al.'s initial attempt to synthesize B-site doping of $SrMnO_{3-\delta}$ by Ce led to the development of the novel Ruddlesden−Popper (layered perovskite) phase discussed previously. $SrCe_yMn_{1-y}O_3$ (y = 0, 0.3, 0.5, 0.7, 1.0) were investigated. In all cases, a mixture of $SrCeO_3$ and/or $SrMnO_3$, CeO_2, and $Ce_xSr_{2-x}MnO_4$ was developed as secondary phases though the compositional range, despite the tolerance factor calculation predicting a cubic phase for doped samples. Two samples were tested for STCH production. The first one, y = 0.5, contained 8% $SrCeO_3$, 53% $Ce_xSr_{2-x}MnO_4$, 27% CeO_2, and 12% $SrMnO_3$ and produced 140.0 μmol g^{-1} of H_2. The second one, y = 0.7, contained 52% $SrCeO_3$, 33% $Ce_xSr_{2-x}MnO_4$, and 15% CeO_2, and it produced 100.0 μmol g^{-1} of H_2. As a result, only CeO_2 and the RP phase are thermochemically active, with the latter one showing higher activity as a higher concentration presented a higher H_2 yield.[108] Su Jeong Heo et al. investigated the possibility of double Ce substitution of the $(Ba,Sr)MnO_{3-\delta}$ perovskite (i.e., $(Ba,Sr)_{1-x}Ce_xCe_yMn_{1-y}O_{3-\delta}$) following the results obtained from Débora R. Barcellos et al. The initial models of single- and double-site substitution using the Goldschmidt tolerance factor were applied to the composition space of a $(Ba,Sr)_{1-x}Ce_xCe_yMn_{1-y}O_{3-\delta}$ quaternary phase diagram and a $BaMnO_3$−$SrMnO_3$−CeO_2 ternary phase diagram, respectively. These models demonstrated the possible structural changes induced in $(Ba,Sr)MnO_{3-\delta}$ due to reductions in the tolerance factor. The authors concluded that the double-site substitution of Ce in $(Ba,Sr)MnO_{3-\delta}$ expands the composition range of stability for 10H (e.g., $BaCe_{0.25}Mn_{0.75}O_{3-\delta}$) and 3C (e.g., $Sr_{0.75}Ce_{0.25}MnO_{3-\delta}$) perovskite structures, which are known to be suitable for STCH applications. Moreover, the introduction of Sr^{2+} into $Ba(Ce,Mn)O_3$ increases the occurrence of 10H phase formation from 25% Ce to approximately 32% Ce, overcoming the restriction of having an exact Ce/Mn ratio of 0.25/0.75 for $BaCe_{0.25}Mn_{0.75}O_{3-\delta}$.[123] In recent years, E. A. Carter's research group has specifically considered the incorporation of only Ce and/or Ca on the A-site of perovskite structures due to their similar ionic sizes and the potential redox activity of Ce^{4+}. Furthermore, they have identified promising candidates, including $Ca_{0.5}Ce_{0.5}MnO_3$, $Ca_{0.5}Ce_{0.5}FeO_3$, and $Ca_{0.5}Ce_{0.5}VO_3$, based on their favorable oxygen vacancy formation energies and thermodynamic stability. Notably, $Ca_{0.5}Ce_{0.5}MnO_3$ stands out as an exceptional candidate for STCH applications. This compound exhibits simultaneous reduction of both Ce^{4+} on the A-site and Mn^{3+} on the B-site, making it particularly promising due to its predicted higher reduction entropy compared to CeO_2.[124] They have also introduced a new redox-active perovskite, $Ca_{2/3}Ce_{1/3}Ti_{1/3}Mn_{2/3}O_3$, which exhibits a high-purity phase. Experimental and modeling results have demonstrated that the main redox-active species in this perovskite is Ce^{4+}, undergoing a reduction from Ce^{4+} to Ce^{3+}. This marks the first report of a perovskite with both a reducible A-site and reducible Ce^{4+}, which distinguishes it from other known reducible perovskites where the active element is invariably located on the B-site.[125]

C. N. R. Rao's group first explored $La_{0.5}Sr_{0.5}Mn_{0.95}Sc_{0.05}O_3$ in thermochemical water-splitting. They reported that substitution of even 5% Sc^{3+} (x = 0.05) results in an outstanding performance. For instance, the yield of the O_2 is almost twice that of the parent perovskite $La_{0.5}Sr_{0.5}MnO_3$. Furthermore, $La_{0.5}Sr_{0.5}Mn_{0.95}Sc_{0.05}O_3$ produced 250 μmol g^{-1} of H_2 at 1100 °C.[126] In addition, Lulu Wang et al. also conducted an investigation involving the doping of Ga^{3+} ions on the B-site of perovskites. This study led to the discovery of a novel perovskite composition, $La_{0.6}Ca_{0.4}Mn_{0.8}Ga_{0.2}O_3$, exhibiting an exceptional water-splitting performance. It generated a noteworthy 401 μmol g^{-1} of H_2 at relatively low thermochemical cycle temperatures between 1300 and 900 °C.[110] Remarkably, this as-prepared perovskite demonstrated 12× higher H_2 production compared to the benchmark CeO_2 catalyst under the same experimental conditions. Additionally, this innovative perovskite demonstrated remarkable stability and steady-state redox activity throughout the water-splitting cycles.[110]

$La_{0.7}Sr_{0.3}Mn_{1-z}Cr_zO_3$ was examined by Nobuyuki Gokon et al. They reported that lower amounts of Cr (z = 0.1 and 0.2) promote oxidation kinetics, and a small Cr content in $LaSrMnO_3$ can enhance the overall thermochemical efficiency.[90] They explored the influence of the thermal reduction temperatures of 1000−1350 °C on O_2/H_2 productivity and repeatability with water-splitting at 1200 °C. $La_{0.7}Sr_{0.3}Mn_{0.9}Cr_{0.1}O_3$ exhibited notable oxygen evolution rates within the temperature range of 1350−1300 °C, while demonstrating comparable rates in the range of 1000−1200 °C. Following treatment at temperatures of 1350−1300 °C during the thermal reduction (TR) process, the resulting samples exhibited superior hydrogen production rates. Conversely, during TR at 1000−1200 °C, the sample exhibited favorable reactivity and consistency in both oxygen release and hydrogen production, even at lower production levels, without encountering coagulation or sintering issues.[127] Berke Piskin's group investigated the effect of a range of calcium concentrations (x = 0, 0.2, 0.4, 0.6, 0.8) in $La_{1-x}Ca_xMn_{0.8}Co_{0.2}O_3$ (LCMC) perovskite-type oxide and explored the hydrogen production about their kinetics, structural properties, H_2/O_2 production capacities, and cyclabilities. Among these compositions, LCMC6282 and LCMC8282 displayed hydrogen productions of 88 and 256 μmol g^{-1}, respectively. However, all materials examined suffer from poor cyclability.[128]

In addition to the study of $La_{0.6}Sr_{0.4}MnO_3$ presented earlier, Luciani et al. studied $La_{0.6}Sr_{0.4}Mn_{1-x}Fe_xO_3$ (x = 0, 0.2, 0.4, and 0.6) for STCH applications via reduction through the usage of H_2 balanced in N_2. Thus, x = 0 presented a tetragonal structure, x = 0.2 represented the coexistence of tetragonal and orthorhombic structures, x = 0.4 and x = 0.6 represented single rhombohedral structures, and x = 1.0 presented both rhombohedral and tetragonal structures with a minor presence of the $SrLaFeO_4$ phase. x = 1.0 was the most reducible of the samples, showing both the lowest reduction temperature (i. e., 400 °C) and the highest O_2 production. For x = 0.4 and x = 0.6, the start of reduction occurred at temperatures higher that for x = 0, with the presence of a small reduction phenomenon at low temperatures becoming more apparent with increasing Fe content. The reduced amount of released oxygen for x = 0.2 and x = 0.4 was ascribed to the preferential substitution of Fe^{3+} ions to Mn^{4+} species, which accounts for the decrease in the

https://doi.org/10.1021/acscatal.4c03357
ACS Catal. 2024, 14, 14974−15013

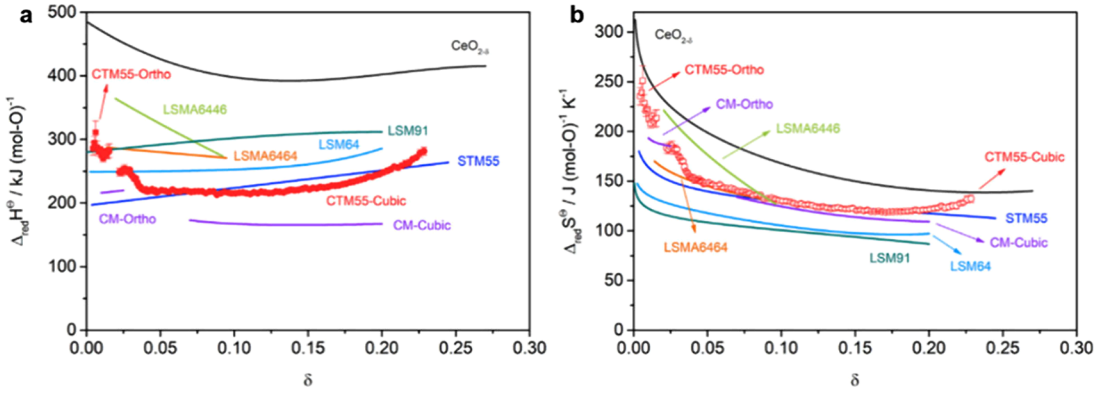

Figure 11. (a) Standard enthalpy of reduction and (b) standard entropy of reduction for a series of oxides, including $CaMnO_3$ (CM) and $SrTi_{0.5}Mn_{0.5}O_{3-\delta}$ (STM55).[66] Reproduced from ref 66. Available under a Creative Commons CC-BY-NC-ND license. Copyright 2020 Qian and co-workers.

overall reduction behavior. After water-splitting tests, the secondary phase (i.e., $SrLaFeO_4$) in $x = 1.0$ disappeared while the tetragonal phase became dominant; for $x = 0$, the presence of both tetragonal and hexagonal phases demonstrated that reduction in a hydrogen atmosphere leads to a phase transition in the perovskite structure. The authors highlighted that no reduced phase is detected after H_2 reduction; rather, any change is related to the conversion from one perovskite structure to another. Production of H_2 steadily increases with increasing Fe content, with the onset temperature of H_2 production also increasing with the Fe content, while oxidation is preferred by the Mn content through a decrease in the onset temperature of O_2 evolution.[96] $LaFe_{1-y}Mn_yO_3$ ($y = 0$, 0.05, 0.1, 0.2, 0.3, 0.4, 0.5) (25 wt %)/SiO_2 were investigated by Zhenpan Chen et al. Relative to undoped $LaFeO_3/SiO_2$, the addition of approximately 5 at. % Mn leads to an approximately 20% increase in the maximum rate of oxygen release. However, with higher Mn doping levels, the maximum oxygen release rate begins declining. Concurrently, the highest rate of hydrogen release experiences a gradual reduction as the Mn content increases, attributed to the diminishing thermodynamic impetus behind the water-splitting reaction.[129] G. Luciani et al. also explored $La_{0.6}Sr_{0.4}Mn_{1-x}Fe_xO_{3-\delta}$ ($x = 0.2$, 0.4, and 0.6). The increase of the iron content corresponds to a progression in the reduction stage, as indicated by the trend of the initial reduction temperatures. Conversely, heightened levels of manganese appear to enhance the activity to water-splitting.[96]

Xin Qian et al. explored the redox thermodynamics of $SrTi_{0.5}Mn_{0.5}O_{3-\delta}$ for water-splitting. The authors mention that a material that readily releases oxygen in the thermal reduction step will typically have a small driving force for reoxidation by steam during the water-splitting process. Under nonisothermal conditions, the previously mentioned contradictions can be addressed by developing a material with a significant entropy of reduction, primarily driven by configurational entropy arising from the creation of oxygen vacancies. Regarding the entropy of reduction, that of the sample is comparable to those of undoped or lightly B-site-doped alkaline manganates. Additionally, it is substantially larger than that of $La_{0.6}Sr_{0.4}MnO_3$, which is a material known for its suitability in STCH applications. The enthalpy of reduction for $SrTi_{0.5}Mn_{0.5}O_{3-\delta}$ was found to be higher than those of undoped or lightly B-site-doped alkaline manganates such as $CaMnO_3$ (i.e., 161−178 kJ (mol-O)$^{-1}$), as shown in Figure 11, and $SrMnO_3$ (i.e., 147 kJ (mol-O)$^{-1}$).[66]

Upon multiple cycles, three features became evident: (1) oxygen release is faster than hydrogen production, as expected from the quasi-equilibrium behavior and thermodynamic properties of the material; (2) there is no evidence of decay in hydrogen production between cycles; and (3) the H_2/O_2 ratio remains consistently close to 2:1 for all cycles, indicating the full utilization of oxygen vacancies generated during reduction.[127] On the next year, the same group of authors (i.e., Xin Qian et al.) explored the properties and STCH performance of $CaTi_{0.5}Mn_{0.5}O_{3-\delta}$. The perovskite adopted the $GdFeO_3$-type phase with an orthorhombic distortion, with a random arrangement of Ti and Mn on the B-site. The behavior of $CaTi_{0.5}Mn_{0.5}O_{3-\delta}$ exactly resembled that of $CaMnO_3$.[66] $CaMnO_3$ is considered a promising candidate in thermochemical heat storage, as it can reversibly release oxygen over a wide range of oxygen partial pressures and temperatures. However, it undergoes decomposition at a temperature of ≥1100 °C and $P_{O_2} \leq 0.008$ atm. Sossina M. Haile's group explored two doping levels, $x = 0.1$ and 0.3, in $CaFe_xMn_{1-x}O_{3-\delta}$ to overcome this shortage and extend the operating temperature. They discovered that $CaFe_{0.1}Mn_{0.9}O_{3-\delta}$ can prevent $CaMnO_3$ decomposition up to 1200 °C at $P_{O_2} = 0.008$ atm.[67] In situ analysis in air of $CaTi_{0.5}Mn_{0.5}O_{3-\delta}$ showed the reversible transitions between the orthorhombic and cubic phases, with the latter being the only phase present after 1200 °C. Ex situ analysis revealed a minimum stability condition of 1600 °C under air and 1450 °C under $P_{O_2} = 4.20 \times 10^{-5}$ atm for the sample, with the latter showing the presence of stoichiometric $CaTiO_3$ and $Ca_{0.5}Mn_{0.5}O$ that implied the complete reduction of Mn into the 2+ oxidation state while Ti retained its 4+ oxidation state. Through the mass loss profile studies described earlier, both the reduction enthalpy and reduction entropy of the orthorhombic phase are larger than those of the cubic phase, with the entropy approaching that of $CeO_{2-\delta}$ and similar to that of $La_{0.6}Sr_{0.4}Mn_{0.4}Al_{0.6}O_{3-\delta}$, and the enthalpy being moderate and approaching those of $La_{0.6}Sr_{0.4}Mn_{0.6}Al_{0.4}O_{3-\delta}$ and $La_{0.9}Sr_{0.1}MnO_{3-\delta}$. Nevertheless, the cubic region showed thermodynamic properties similar to that of $Sr_{0.5}Ti_{0.5}MnO_{3-\delta}$, suggesting a cubic or near-cubic perovskite presents a low enthalpy of reduction and is the phase present under high δ, as seen under STCH conditions. Overall, the instruction of Ti into the $CaMnO_3$ perovskite

https://doi.org/10.1021/acscatal.4c03357
ACS Catal. 2024, 14, 14974−15013

increased the enthalpy while having little effect on the entropy, which is highly desirable for water-splitting applications.[66] Greta R. Patzke's group investigated the potential of cation-deficient oxides $(Ce_xSr_{1-x})_{0.95}Ti_{0.5}Mn_{0.5}O_{3-\delta}$ (x = 0, 0.10, 0.15, and 0.20; CSTM) as the redox materials for solar-driven thermochemical (STC) fuel production. With the substitution of Ce, the enthalpy and entropy change increase simultaneously. $(Ce_{0.2}Sr_{0.8})_{0.95}Ti_{0.5}Mn_{0.5}O_{3-\delta}$ (CSTM20) has a combination of a moderate enthalpy change of about 238 kJ $(mol\text{-}O)^{-1}$ and a large entropy change of about 141 $J(mol\text{-}O)^{-1}K^{-1}$, which created a favorable thermodynamic property for H_2O splitting. Both Ce and Mn are redox-active centers that experience concurrent reduction during redox cycling, as confirmed by X-ray absorption spectroscopy (XAS).[130]

$La_{0.5}Sr_{0.5}Mn_{0.9}Mg_{0.1}O_3$ was investigated as a perovskite coating by Haeussler et al. due to its thermochemical stability and high fuel productivity. Anita Haeussler et al. focused on the thermochemical performance of a composite reactive material composed of reticulated ceria foam with a uniform perovskite coating consisting of $La_{0.5}Sr_{0.5}Mn_{0.9}Mg_{0.1}O_3$ to enhance the reduction extent in comparison with pure ceria. Ceria, in this regard, has limitations due to its moderate reduction extent at temperatures up to 1400 °C, while perovskites offer a higher oxygen exchange capacity under similar conditions. Nevertheless, the reoxidation of perovskites is slow and incomplete due to their thermodynamic limitations, whereas ceria reoxidation is thermodynamically more favorable. Therefore, the addition of a thin layer of perovskite to ceria should enhance its reduction ability, as the perovskite is expected to promote oxygen diffusion within ceria.[131] Two year later, Haeussler et al. explored a wide range of ABO_3 compositions (with A = La, Y, Sr, Ca, Pr, Ce, Sm and B = Co, Mn, Fe, Al, Ga, Mg, Cr) to identify suitable formulations for thermochemical cycles that could potentially achievea high solar-to-fuel conversion efficiency. Stéphane Abanades's group also investigated $La_{0.5}Sr_{0.5}Mn_{0.9}Mg_{0.1}O_3$ and discovered that the presence of a Mg^{2+} ion can stabilize the perovskite structure, as the thermochemical cycles measured in TGA did not induce sintering. Mg is promising as a dopant, it can enhance the oxidation degree of Mn even though Mg^{2+} is not involved in redox reactions.[132] Table 5 provides a comprehensive overview of the solar thermochemical hydrogen (STCH) production performance of MnX-based perovskite oxides when subjected to inert gas conditions.

Table 6 provides a detailed analysis of the solar thermochemical hydrogen (STCH) production performance of MnX-based perovskite oxides under reducing gas conditions.

5.4. Fe- and FeX-Based Perovskite Oxides As Redox-Active Oxygen Exchange Materials. Alongside $La_{1-x}Sr_xMnO_3$ perovskites, $La_{1-x}Sr_xFeO_3$ was also among the first families of perovskites tested for STCH. When compared to the temperature requirements for the reduction of manganese-based materials (LSM-20 and LSM-35), which necessitate temperatures close to 1400 °C, the theoretical temperature needed for the reduction of Fe-based materials is lower, at 1150 °C.[97] In 2009, Nalbandian et al. followed the same parameters and synthesis used by Edvou et al. using the oxidation of CH_4 as a means of reducing their perovskite material and pure steam as the oxidizing medium. Their perovskites achieved cumulative H_2 production of 261.0 μmol g^{-1} per ~2000 μmol g^{-1} of H_2O at x = 0.3, while reaching 123.0 μmol g^{-1} of H_2 per ~1000 μmol g^{-1} of H_2O at x = 0.7 and 130.0 μmol g^{-1} of H_2 per ~1000 μmol g^{-1} of H_2 at x = 1.[133] Commercial $La_{0.6}Sr_{0.4}FeO_{3-\delta}$ rendered 124.0 μmol g^{-1} of H_2 under isothermal 1400 °C conditions with undefined reduction/oxidation times, and undefined steam concentration.[97] G. Luciani et al. examined the perovskite $La_{0.6}Sr_{0.4}FeO_{3-\delta}$, which exhibited the most substantial release of oxygen (427.3 μmol g^{-1}) during thermogravimetric analysis and generated significant hydrogen production (3359.0 μmol g^{-1}) in splitting tests.[96] In 2014, the commercial $La_{0.6}Sr_{0.4}FeO_{3-\delta}$, which was also used as a mixed ionic electronic conductor in fuel cells, was also investigated by Stéphane Abanades's group, who found an oxygen production of 425 μmol g^{-1} at 1200 °C.[95] Additionally, Lulu Wang et al. similarly explored $La_{0.6}Sr_{0.4}FeO_{3-\delta}$, emphasizing the essential role of oxygen vacancies within metal oxide for controlling significant redox properties.[105] $LaFeO_3$ has recently attracted attention for its impressive performance in photocatalytic hydrogen production, but its use in STCH has been relatively unexplored. In this study, Jin et al. employed a first-principles method at the density functional theory level to investigate the hydrogen production mechanism of $LaFeO_3$ perovskite doped with 25% Sr/Ca at the A-site. The rate of hydrogen production is determined by the migration of hydrogen at the surface. The water-splitting (WS) mechanism of $La_{0.75}A_{0.25}FeO_3$ (A = Ca, Sr) elucidates the process of water-splitting and H_2 generation on the defected material surface. For example, in the case of $La_{0.75}Sr_{0.25}FeO_3$, the process begins with the approach and adsorption of H_2O on the defective surface, releasing 16.94 kJ mol^{-1} of energy. Subsequently, one of the two H−O bonds of H_2O is broken, and the H atom combines with an adjacent lattice O atom on the surface, forming a hydroxyl group. Another hydroxyl group fills the oxygen vacancy, releasing 43.72 kJ mol^{-1} of energy. This decomposition of H_2O into two hydroxyl groups is followed by successive hydrogen production and desorption steps. In summary, $LaFeO_3$'s hydrogen production mechanism involves several energy-releasing steps, with a distinct transition state observed during hydrogen migration.[134] Recently, Park et al. have introduced another mechanism in which the distribution of the oxygen formation energy (therefore enthalpy) can lead to increased H_2 production, particularly when the P_{H_2}/P_{H_2O} ratio is relatively low. Their results indicate that distribution refers to both the average and the spreading of the oxygen vacancy formation energy.[135] Maria Batuk et al. were the first to report in situ 3D electron diffraction (ED) studies of $SrFeO_{2.5}$ in both O_2 and H_2 environments. Their research provided detailed insights into the structural changes occurring during redox reactions at the nanoscale, involving individual particles with dimensions of a few hundred nanometers. The results notably revealed the formation of the $SrFeO_{2.75}$ *Cmmm* structure upon oxidation, followed by a subsequent transformation into the perovskite $SrFeO_{3-\delta}$ with a $Pm\bar{3}m$ structure. Importantly, this phase transition had not been observed in prior in situ experiments conducted in gas environments using X-ray or neutron powder diffraction techniques.[136]

In addition to the presence of Sr on the A-site, Hartley's group also investigated the incorporation of Ba on the A-site. They discovered that $Ba_{0.95}La_{0.05}FeO_{3-\delta}$ (BLF) with a cubic phase exhibited the most substantial H_2 production (approximately 1310 μmol g^{-1}) under an isothermal reduction/oxidation temperature of 900 °C. However, it should be noted that this catalyst faced challenges related to "sintering"

https://doi.org/10.1021/acscatal.4c03357
ACS Catal. 2024, 14, 14974−15013

Table 5. STCH Performance of MnX-Based Perovskite Oxides under Inert Gas Conditions

composition	synthesis method	cycles	$\Delta\delta$	temp. red./ox. (°C)	time red./ox. (min)	H_2O (% vol)	gas red./ox.	O_2 yield (μmol g^{-1})	H_2 yield (μmol g^{-1})	average H_2 production rate (μmol g^{-1} min^{-1})	ref
$BaCe_{0.05}Mn_{0.95}O_{3-\delta}$	Pechini		0.345				N_2/air				26
$BaCe_{0.15}Mn_{0.85}O_{3-\delta}$	Pechini		0.228				N_2/air				26
$BaCe_{0.25}Mn_{0.75}O_{3-\delta}$	Pechini	3	0.183	1400/1000	5.5/20	40.0	Ar/Ar		181.0	9.05	26
$BaCe_{0.25}Mn_{0.75}O_{3-\delta}$	Pechini	3		1400/850	5.5/20	40.0	Ar/Ar		165.0	8.25	26
$BaCe_{0.25}Mn_{0.75}O_{3-\delta}$	Pechini	3	0.183	1400/750	5.5/20	40.0	Ar/Ar		136.0	6.80	26
$BaCe_{0.25}Mn_{0.75}O_{3-\delta}$	Pechini	3		1350/1000	5.5/20	40.0	Ar/Ar		146.0	7.30	26
$BaCe_{0.25}Mn_{0.75}O_{3-\delta}$	Pechini	3		1350/850	5.5/20	40.0	Ar/Ar	82.0	140.0	7.00	26
$BaCe_{0.25}Mn_{0.75}O_{3-\delta}$	Pechini	50		1350/850	3.5/10	40.0	Ar/Ar	65.0	138.0	13.80	26
$BaCe_{0.25}Mn_{0.75}O_{3-\delta}$	Pechini	1		1350/850	5.5/20	40.0	Ar/Ar–H_2[b]		98.2	4.91	26
$BaCe_{0.25}Mn_{0.75}O_{3-\delta}$	Pechini	1		1350/850	5.5/20	40.0	Ar/Ar–H_2[c]		93.5	4.68	26
$BaCe_{0.25}Mn_{0.75}O_{3-\delta}$	Pechini	1		1350/850	5.5/20	40.0	Ar/Ar–H_2[d]		67.1	3.36	26
$BaCe_{0.25}Mn_{0.75}O_{3-\delta}$	Pechini	1		1350/850	5.5/20	40.0	Ar/Ar–H_2[e]		64.1	3.21	26
$BaCe_{0.25}Mn_{0.75}O_{3-\delta}$	Pechini	1		1350/850	5.5/20	40.0	Ar/Ar–H_2[f]		26.5	1.33	26
$BaCe_{0.25}Mn_{0.75}O_{3-\delta}$	Pechini	3		1350/750	5.5/20	40.0	Ar/Ar		99.0	4.95	26
$BaCe_{0.25}Mn_{0.75}O_{3-\delta}$	Pechini	3		1250/1000	5.5/20	40.0	Ar/Ar		86.0	4.30	26
$BaCe_{0.25}Mn_{0.75}O_{3-\delta}$	Pechini	3		1250/850	5.5/20	40.0	Ar/Ar		56.0	2.80	26
$BaCe_{0.25}Mn_{0.75}O_{3-\delta}$	Pechini	3		1250/750	5.5/20	40.0	Ar/Ar		52.0	2.60	26
$BaCe_{0.50}Mn_{0.50}O_{3-\delta}$	Pechini	3	0.104	1350/1000	5.5/20	40.0	Ar/Ar		97.0	4.85	26
$BaCe_{0.75}Mn_{0.25}O_{3-\delta}$	Pechini	3	0.158	1350/1000	5.5/20	40.0	Ar/Ar		40.5	2.03	26
$SrCe_{0.3}Mn_{0.7}O_{3-\delta}$	Pechini	1		1400/1000	5.5/16.7	50.0	Ar/Ar				108
$SrCe_{0.5}Mn_{0.5}O_{3-\delta}$	Pechini	1		1400/1000	5.5/16.7	50.0	Ar/Ar		140.0	8.38	108
$SrCe_{0.7}Mn_{0.3}O_{3-\delta}$	Pechini	1		1400/1000	5.5/16.7	50.0	Ar/Ar		100.0	5.99	108
$Sr_{0.75}Ce_{0.25}MnO_{3-\delta}$	Pechini	3		1400/1000	5.5/20	40.0	Ar/Ar	104.0	224.0	11.20	123
$Sr_{0.75}Ce_{0.25}MnO_{3-\delta}$	Pechini	3		1350/850	5.5/20	40.0	Ar/Ar	68.0	98.0	4.90	123
$La_{0.5}Sr_{0.5}Mn_{0.95}Sc_{0.05}O_{3-\delta}$	Pechini	3	0.21	1400/1100	45/		Ar/-	417.0			126
$La_{0.5}Sr_{0.5}Mn_{0.95}Sc_{0.05}O_{3-\delta}$	Pechini	1	0.21	1400/1100	45/100		N_2/N_2	390.0	250.0	2.50	126
$La_{0.5}Sr_{0.5}Mn_{0.9}Sc_{0.1}O_{3-\delta}$	Pechini	1	0.21	1400/1100	45/		Ar/-	426.0			126
$La_{0.6}Ca_{0.4}Mn_{0.8}Ga_{0.2}O_{3-\delta}$	Pechini	6		1300/900	60/60	40.0	Ar/Ar	212.0	401.0	6.68	110
$La_{0.6}Ca_{0.4}Mn_{0.8}Ga_{0.2}O_{3-\delta}$	Pechini	1		1400/900	60/60	40.0	Ar/Ar	320.0	473.0	7.88	110
$La_{0.7}Sr_{0.3}Mn_{0.9}Cr_{0.1}O_{3-\delta}$	Pechini	3		1350/1000	1[a]/60	84.0	N_2/N_2	96.2[g]	145.8[g]	2.43	90
$La_{0.7}Sr_{0.3}Mn_{0.9}Cr_{0.1}O_{3-\delta}$	Pechini	3		1350/1200	1[a]/60	84.0	N_2/N_2	107.6[g]	160.9[g]	2.68	90
$La_{0.7}Sr_{0.3}Mn_{0.8}Cr_{0.2}O_{3-\delta}$	Pechini	3		1350/1000	1[a]/60	84.0	N_2/N_2	97.7[g]	113.9[g]	1.90	90
$La_{0.7}Sr_{0.3}Mn_{0.8}Cr_{0.2}O_{3-\delta}$	Pechini	3		1350/1100	1[a]/60	84.0	N_2/N_2	106.8[g]	133.0[g]	2.22	90
$La_{0.7}Sr_{0.3}Mn_{0.8}Cr_{0.2}O_{3-\delta}$	Pechini	3		1350/1200	1[a]/60	84.0	N_2/N_2	102.3[g]	160.2[g]	2.67	90
$La_{0.7}Sr_{0.3}Mn_{0.7}Cr_{0.3}O_{3-\delta}$	Pechini	3		1350/1000	1[a]/60	84.0	N_2/N_2	86.7[g]	123.9[g]	2.07	90
$La_{0.7}Sr_{0.3}Mn_{0.6}Cr_{0.4}O_{3-\delta}$	Pechini	3		1350/1000	1[a]/60	84.0	N_2/N_2	87.7[g]	93.4[g]	1.56	90
$La_{0.7}Sr_{0.3}Mn_{0.5}Cr_{0.5}O_{3-\delta}$	Pechini	3		1350/1000	1[a]/60	84.0	N_2/N_2	85.3[g]	73.8[g]	1.23	90
$La_{0.7}Sr_{0.3}Mn_{0.3}Cr_{0.7}O_{3-\delta}$	Pechini	3		1350/1000	1[a]/60	84.0	N_2/N_2	75.3[g]	56.2[g]	0.94	90
$La_{0.7}Sr_{0.3}Mn_{0.9}Cr_{0.1}O_{3-\delta}$	Pechini	3		1350/1200	30[a]/60	84.0	N_2/N_2	107.1[g]	160.1[g]	2.67	127
$La_{0.7}Sr_{0.3}Mn_{0.9}Cr_{0.1}O_{3-\delta}$	Pechini	3		1300/1200	30[a]/60	84.0	N_2/N_2	92.6[g]	277.8[g]	4.63	127
$La_{0.7}Sr_{0.3}Mn_{0.9}Cr_{0.1}O_{3-\delta}$	Pechini	3		1250/1200	30[a]/60	84.0	N_2/N_2	89.7[g]	135.0[g]	2.25	127

https://doi.org/10.1021/acscatal.4c03357
ACS Catal. 2024, 14, 14974−15013

Table 5. continued

composition	synthesis method	cycles	$\Delta\delta$	temp. red./ox. (°C)	time red./ox. (min)	H_2O (% vol)	gas red./ox.	O_2 yield (μmol g^{-1})	H_2 yield (μmol g^{-1})	average H_2 production rate (μmol g^{-1} min^{-1})	ref
$La_{0.7}Sr_{0.3}Mn_{0.9}Cr_{0.1}O_{3-\delta}$	Pechini	3		1200/1200	30[a]/60	84.0	N_2/N_2	74.3[g]	82.9[g]	1.38	127
$La_{0.7}Sr_{0.3}Mn_{0.9}Cr_{0.1}O_{3-\delta}$	Pechini	3		1100/1200	30[a]/60	84.0	N_2/N_2	29.9[g]	70.4[g]	1.17	127
$La_{0.7}Sr_{0.3}Mn_{0.9}Cr_{0.1}O_{3-\delta}$	Pechini	3		1000/1200	30[a]/60	84.0	N_2/N_2	22.2[g]	117.7[g]	1.96	127
$LaFe_{0.95}Mn_{0.05}O_{3-\delta}$(25 wt %)/$SiO_2$	combustion	1		1350/1100	40/15	100.0	Ar/-		87.1[g]	5.81	129
$LaFe_{0.9}Mn_{0.1}O_{3-\delta}$(25 wt %)/$SiO_2$	combustion	1		1350/1100	40/15	100.0	Ar/-	117.6[g]	78.3[g]	5.22	129
$LaFe_{0.9}Mn_{0.1}O_{3-\delta}$(25 wt %)/$SiO_2$	combustion	1		1350/1100	40/60	100.0	Ar/-	117.6[g]	100.4[g]	1.67	129
$LaFe_{0.8}Mn_{0.2}O_{3-\delta}$(25 wt %)/$SiO_2$	combustion	1		1350/1100	40/15	100.0	Ar/-		67.8[g]	4.52	129
$LaFe_{0.7}Mn_{0.3}O_{3-\delta}$(25 wt %)/$SiO_2$	combustion	1		1350/1100	40/15	100.0	Ar/-		50.0[g]	3.33	129
$LaFe_{0.6}Mn_{0.4}O_{3-\delta}$(25 wt %)/$SiO_2$	combustion	1		1350/1100	40/15	100.0	Ar/-		43.8[g]		129
$LaFe_{0.5}Mn_{0.5}O_{3-\delta}$(25 wt %)/$SiO_2$	combustion	1		1350/1100	40/15	100.0	Ar/-		35.3[g]	2.35	129
$Sr_{0.75}Ce_{0.25}MnO_{3-\delta}$	Pechini	3		1400/1000	5.5/20	40.0	Ar/Ar	104.0	224.0	11.20	76
$Sr_{0.75}Ce_{0.25}MnO_{3-\delta}$	Pechini	3		1350/850	5.5/20	40.0	Ar/Ar	68.0	98.0	4.90	76
$La_{0.8}Ca_{0.2}Mn_{0.8}Co_{0.2}O_{3-\delta}$	sol−gel	1		1400/800	120/120		Ar/Ar	186.0	256.0	2.13	128
$La_{0.6}Ca_{0.4}Mn_{0.8}Co_{0.2}O_{3-\delta}$	sol−gel	1		1400/800	120/120		Ar/Ar	275.0	88.0	0.73	128
$La_{0.4}Ca_{0.6}Mn_{0.8}Co_{0.2}O_{3-\delta}$	sol−gel	1		1400/800	120/120		Ar/Ar	722.0	6.0	0.05	128
$La_{0.2}Ca_{0.8}Mn_{0.8}Co_{0.2}O_{3-\delta}$	sol−gel	1		1400/800	120/120		Ar/Ar	924.0	27.0	0.23	128
$La_{0.8}Ca_{0.2}Mn_{0.8}Co_{0.2}O_{3-\delta}$	sol−gel	2		1400/800	120/120		Ar/Ar	183.0	82.0	0.68	128
$La_{0.6}Ca_{0.4}Mn_{0.8}Co_{0.2}O_{3-\delta}$	sol−gel	2		1400/800	120/120		Ar/Ar	214.0	78.0	0.65	128
$La_{0.8}Ca_{0.2}Mn_{0.8}Co_{0.2}O_{3-\delta}$	sol−gel	3		1400/800	120/120		Ar/Ar	159.0	44.0	0.37	128
$La_{0.6}Ca_{0.4}Mn_{0.8}Co_{0.2}O_{3-\delta}$	sol−gel	3		1400/800	120/120		Ar/Ar	167.0	54.0	0.45	128
$Ca_{2/3}Ce_{1/3}Ti_{1/3}Mn_{2/3}O_3$	solid-state	1		1350/850	∼30/30	40.0	Ar/Ar		298.8	9.96	125
$Ca_{2/3}Ce_{1/3}Ti_{1/3}Mn_{2/3}O_3$	solid-state	2		1350/850	∼30/30	40.0	Ar/Ar		307.4	10.25	125
$SrTi_{0.5}Mn_{0.5}O_{3-\delta}$	solid-state	10		1400/800	30/60	20.0	Ar/Ar	85.3[g]	165.6[g]	2.76	127
$SrTi_{0.5}Mn_{0.5}O_{3-\delta}$	solid-state	10		1400/1000	30/60	20.0	Ar/Ar	116.5[g]	237.1[g]	3.95	127
$SrTi_{0.5}Mn_{0.5}O_{3-\delta}$	solid-state	10	0.230	1400/1000	30/60	40.0	Ar/Ar	152.7[g]	308.5[g]	5.14	127
$SrTi_{0.5}Mn_{0.5}O_{3-\delta}$	solid-state	8		1400/1100	30/60	40.0	Ar/Ar	183.5[g]	371.0[g]	6.18	127
$SrTi_{0.5}Mn_{0.5}O_{3-\delta}$	solid-state	10		1400/1200	30/60	40.0	Ar/Ar	134.4[g]	268.3[g]	4.47	127
$SrTi_{0.5}Mn_{0.5}O_{3-\delta}$	solid-state	10		1350/1100	30/60	40.0	Ar/Ar	143.8[g]	281.7[g]	4.70	127
$SrTi_{0.5}Mn_{0.5}O_{3-\delta}$	solid-state	10		1350/1100	30/60	40.0[!]	Ar/Ar	166.1[g]	330.8[g]	5.51	127
$SrTi_{0.5}Mn_{0.5}O_{3-\delta}$	solid-state	10		1350/1100	30/15	40.0	Ar/Ar	54.0[g]	103.6[g]	6.91	127
$SrTi_{0.5}Mn_{0.5}O_{3-\delta}$	solid-state	10		1350/1100	30/15	40.0	Ar/Ar	67.9[g]	134.8[g]	8.99	127
$SrTi_{0.5}Mn_{0.5}O_{3-\delta}$	solid-state	10		1350/1100	30/15	40.0	Ar/Ar	85.3[g]	170.1[g]	11.34	127
$CaTi_{0.5}Mn_{0.5}O_{3-\delta}$	solid-state	14		1350/900	30/60	40.0	Ar/Ar	817.0[g]	228.1[g]	3.80	66
$CaTi_{0.5}Mn_{0.5}O_{3-\delta}$	solid-state	14	0.103	1350/1000	30/60	40.0	Ar/Ar	817.0[g]	268.3[g]	4.47	66
$CaTi_{0.5}Mn_{0.5}O_{3-\delta}$	solid-state	14		1350/1100	30/60	40.0	Ar/Ar	817.0[g]	295.1[g]	4.92	66
$CaTi_{0.5}Mn_{0.5}O_{3-\delta}$	solid-state	14		1350/1150	30/60	40.0	Ar/Ar	817.0[g]	304.0[g]	5.07	66
$CaTi_{0.5}Mn_{0.5}O_{3-\delta}$	solid-state	14		1350/1200	30/60	40.0	Ar/Ar	817.0[g]	286.2[g]	4.77	66

https://doi.org/10.1021/acscatal.4c03357
ACS Catal. 2024, 14, 14974−15013

Table 5. continued

composition	synthesis method	cycles	Δδ	temp. red./ox. (°C)	time red./ox. (min)	H_2O (% vol)	gas red./ox.	O_2 yield (μmol g^{-1})	H_2 yield (μmol g^{-1})	average H_2 production rate (μmol g^{-1} min^{-1})	ref
$CaTi_{0.5}Mn_{0.5}O_{3-\delta}$	solid-state	14		1350/1150	30/60	40.0	Ar/Ar	817.0[g]	339.7[g]	5.66	66
$CaTi_{0.5}Mn_{0.5}O_{3-\delta}$	solid-state	14		1350/1150	30/60	40.0	Ar/Ar	817.0[g]	447.3[g]	7.46	66
$La_{0.5}Sr_{0.5}Mn_{0.9}Mg_{0.1}O_3$	Pechini	1		1400/1050	45/60		Ar/-	269.0		0	131
$La_{0.5}Sr_{0.5}Mn_{0.9}Mg_{0.1}O_3$–$CeO_2$	suspension	1		1399/1040	40/13.1[h]	17.2	Ar/Ar	87.0	149.0	11.37	131
$La_{0.5}Sr_{0.5}Mn_{0.9}Mg_{0.1}O_3$–$CeO_2$	suspension	1		1409/1034	40/6.1[h]	24.2	Ar/Ar	203.0	234.0	38.36	131
$La_{0.5}Sr_{0.5}Mn_{0.9}Mg_{0.1}O_3$–$CeO_2$	suspension	1		1407/959	40/7.5[h]	50.0	Ar/Ar	72.0	166.0	22.13	131
$La_{0.5}Sr_{0.5}Mn_{0.9}Mg_{0.1}O_3$	Pechini	1	0.231	1400/1050	-/40	50.0	Ar/Ar	206.0	236.0	5.90	132
$La_{0.5}Sr_{0.5}Mn_{0.9}Mg_{0.1}O_3$	Pechini	2	0.231	1400/1050	-/40	50.0	Ar/Ar	123.0	251.0	6.28	132

[a]Sample was cooled to RT after reduction and pulverized prior to heating to oxidation temperature. [b]H_2O:H_2 = 1333. [c]H_2O:H_2 = 1000. [d]H_2O:H_2 = 750. [e]H_2O:H_2= 500. [f]H_2O:H_2 = 285. [g]Value converted from mL $g_{material}^{-1}$. Standard volume occupied: 22400 mL mol^{-1}. [h]Amount of time for 90% of fuel to be produced.

(coarsening of nanoparticles).[137] Alejandro Perez et al. studied the hydrogen production by thermochemical H_2O splitting with a $La_{0.8}Al_{0.2}FeO_{3-\delta}$ perovskite prepared under a controlled pH during the synthesis process. The reason for changing the pH is that, in the Pechini method, the pH level significantly affects the stability and homogeneity of metal citrate solutions.[138] Figure 12 displays the SEM images of a series of perovskites synthesized at various pH levels, demonstrating their significant impact on the morphological attributes of the perovskites.

Mingkai Fu et al. first filled the gap in the water dissociative mechanism of $LaFeO_3$. They meticulously calculated the entire pathway for water-splitting and H_2 production on a defective $LaFeO_3$ (010) surface. Their findings reveal a distinctive characteristic of the oxidation step on the defected $LaFeO_3$ surface, which is endothermic in nature. This differs markedly from the exothermic water-splitting behavior observed in many other redox materials like CeO_2 and SnO_2.[139]

In addition to the extensively researched Fe-based perovskites, the exploration of FeX-based materials (where X includes Gd, Co, Ni, Al, Ir, and Ti as the doping elements on the B site) has also captured the attention of researchers. For example, when subjecting the materials to TGA testing, the presence of cobalt leads to a more substantial reduction in weight when comparing $La_{0.6}Sr_{0.4}Co_{0.2}Fe_{0.8}O_{3-\delta}$ to $La_{0.6}Sr_{0.4}FeO_{3-\delta}$. This aligns with the general trend of cobalt oxides exhibiting greater ease of reduction compared to iron oxides at equivalent oxidation states.[95] A series of $Ba_xSr_{1-x}Co_yFe_{1-y}O_{3-\delta}$ (x = 0.5, 0.25; y = 0.2, 0.4, 0.6, 0.8) materials were also explored by Stéphane Abanades's group, and they mentioned that introducing Sr^{2+} as a substitute for Ba^{2+} within the BSCF series could potentially stimulate the formation of M^{4+} (M = Mn, Co, Fe) cations, consequently enhancing the likelihood of achieving elevated reduction yields.[95] The combination of Fe and Co in the B-site of the perovskite is beneficial for fuel products. Here, Can Li's group screened a series $LaFe_{1-y}Co_yO_3$ (y = 0, 0.1, 0.2, 0.3, 0.4, and 0.5) and found that when y = 0.2 the H_2 and O_2 production is the highest and the kinetic is the fast as the result of H_2 production of the initial 15 min.[129] Moreover, Zhenpan Chen et al. investigated the effects of a SiO_2 support on the $LaMn_yFe_{1-y}O_3$ perovskite, and they found SiO_2 support was helpful to mitigate sintering effects and disperse iron silicon oxides at high temperatures. Their approach involved the usage of modified glycine nitrate autocombustion to synthesize their perovskites, which were subsequently mechanically milled with SiO_2 prior to the STCH analysis. A temperature sweep of 250 K (1350/1100 °C) was employed, with a reduction time of 40 min, an oxidation time of 15 or 60 min, and pure steam as the oxidizing gas. They witnessed the enhancement of H_2 in $LaFeO_3$ through the support of 25 wt % SiO_2, advancing from a negligible H_2 yield to reach 96.9 μmol g^{-1} after 15 min and a total of 130.5 μmol g^{-1} after the sample was fully oxidized. Doping with Mn did not result in an increase in the STCH performance, being rather detrimental to the yield of H_2. Furthermore, Chen et al. briefly studied the effects of Ni or Al doping in $LaFeO_3$ (25 wt %)/SiO_2 at 10% doping concentration. They too did not see an increase to the production of H_2, with $LaFe_{0.9}Ni_{0.1}O_3$ (25 wt %)/SiO_2 producing 1.4 μmol g^{-1} more than $LaFeO_3$ (25 wt %)/SiO_2 when fully oxidized.[129] The previous study from their group showed the IrO_x-catalyzed CO_2 at high temperatures with similar catalytic functions compared to the catalysis of the

https://doi.org/10.1021/acscatal.4c03357
ACS Catal. 2024, 14, 14974−15013

Table 6. STCH Performance of MnX-Based Perovskite Oxides under Reducing Gas Conditions

composition	synthesis method	cycles	temp. red./ox. (°C)	time red./ox. (min)	H_2O (%vol)	gas red./ox.	O_2 yield (μmol g^{-1})	H_2 yield (μmol g^{-1})	average H_2 production rate (μmol g^{-1} min^{-1})	ref
$La_{0.6}Sr_{0.4}Mn_{0.8}Fe_{0.2}O_{3-\delta}$	sol−gel	2	1000/1000	-/20	3.0	N_2−H_2/N_2[a]	286.0[b]	1205.0[c]	60.25	96
$La_{0.6}Sr_{0.4}Mn_{0.6}Fe_{0.4}O_{3-\delta}$	sol−gel	2	1000/1000	-/20	3.0	N_2−H_2/N_2[a]	280.0[b]	1645.0[c]	82.25	96
$La_{0.6}Sr_{0.4}Mn_{0.4}Fe_{0.6}O_{3-\delta}$	sol−gel	2	1000/1000	-/20	3.0	N_2−H_2/N_2[a]	333.2[b]	2827.0[c]	141.35	96

[a]5 vol % H_2 stream. [b]Results from TGA analysis. [c]Introduction of steam began at 60 °C while ramping to 1000 °C

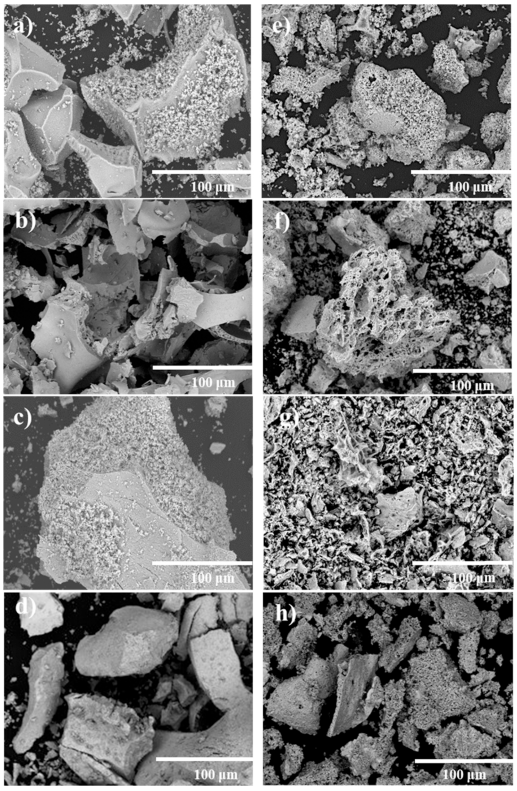

Figure 12. SEM imagines of (a) $La_{0.8}Al_{0.2}CoO_{3-\delta}$ (acid), (b) $La_{0.8}Al_{0.2}NiO_{3-\delta}$ (acid), (c) $La_{0.8}Al_{0.2}FeO_{3-\delta}$ (acid), (d) $La_{0.8}Al_{0.2}CuO_{3-\delta}$ (acid), (e) $La_{0.8}Al_{0.2}CoO_{3-\delta}$ (basic), (f) $La_{0.8}Al_{0.2}NiO_{3-\delta}$ (basic), (g) $La_{0.8}Al_{0.2}FeO_{3-\delta}$ (basic), and (h) $La_{0.8}Al_{0.2}CuO_{3-\delta}$ (basic).[138] Reproduced with permission from ref 138. Copyright 2022 Elsevier.

chemical reaction at the gas−solid interface is probably facilitated by iridium dopants present at the exposed microscale surface, which aligns with the reaction mechanism governed by surface control.[140] Similarly, they found even that when the doping level was a mere 1 at. %, the oxygen release is increased. Additionally, the maximum H_2 rate enhanced roughly 0.5× when 1 at. % Ir was added to $LaFe_{0.99}Ir_{0.01}O_3$/SiO_2.[129] To investigate perovskite materials that can be formed from more earth-abundant elements and to establish techniques for the efficient synthesis of a diverse range of potential compositions, the $CaTi_xFe_{1-x}O_3$ (x = 0.7, 0.8, 0.9, 1) series was studied, and researchers found these oxides exhibit water-splitting activity. Additionally, they reported the redox behavior of $CaTi_{0.7}Fe_{0.3}O_3$ is similar to that of CeO_2, and the total quantity of oxygen produced by $CaTi_{0.7}Fe_{0.3}O_3$ when the reduction temperature at 1320 °C is similar to CeO_2.[77] Sha Chen and colleagues conducted a study using density functional theory calculations to explore how water interacts with the surfaces of perovskite materials based on $SrFeO_{3-\delta}$, doped with different metals (B = Al, Zr, Nb, and W). Their findings revealed that Zr-, Nb-, and W-doped structures enhanced the production of H_2, while the Al-doped structure did not facilitate H_2 release. The calculations demonstrated that the introduction of metal dopants had a positive effect on the molecular and dissociative adsorption of H_2O on both perfect and oxygen-deficient surfaces. Furthermore, the presence of surface oxygen vacancies was predicted to promote the dissociative adsorption of H_2O and the subsequent formation of H_2.[141] Table 7 indicates the STCH performance of Fe and FeX-based perovskite oxides under inert gas conditions.

Table 8 presents a comprehensive analysis of the solar thermochemical hydrogen (STCH) production performance of Fe- and FeX-based perovskite oxides under reducing gas conditions.

5.5. Co- and CoX-Based Perovskite Oxides as Redox-Active Oxygen Exchange Materials. The lanthanum−cobalt perovskites have been investigated in thermochemical cycles by various research groups. For instance, Stéphane Abanades's group reported that $La_{0.8}Sr_{0.2}CoO_{3-\delta}$ produces 732 μmol g^{-1} of oxygen at 1200 °C.[95] Additionally, Mara Orfila et al. evaluated a commercially available Co-based perovskite material, $La_{0.8}Sr_{0.2}CoO_{3-\delta}$. The study revealed that $La_{0.8}Sr_{0.2}CoO_{3-\delta}$ exhibited the highest activity compared to iron-based material $La_{0.6}Sr_{0.4}FeO_{3-\delta}$ and manganese materials (LSM-20, LSM-35), as observed through thermogravimetric analysis. Furthermore, theoretical reduction temperatures for Co-based materials were found to be lower at 1050 °C in comparison to those of Mn-based and Fe-based perovskite. However, both H_2-TPR and SEM results confirmed that the cobalt material undergoes significant changes after 4 reaction cycles, negatively impacting hydrogen production.[97] Lulu Wang et al. investigated a series of $La_{1-x}Ca_xCoO_3$ perovskites for two-step thermochemical H_2O splitting cycles, revealing the significant impact of the Ca dopant content on both thermal reduction and H_2O splitting steps. Enhanced O_2 evolution was achieved with increased Ca doping, but this compromised H_2O splitting thermodynamics and led to lower reoxidation yields. Among the compositions, $La_{0.6}Ca_{0.4}CoO_3$ exhibited the best performance, with the optimal thermochemical operational conditions identified between 1300 (thermal reduction) and 900 °C (reoxidation), resulting in a notable H_2 yield of 587 μmol g^{-1}.[142] Co-based perovskite oxides were extensively investigated in terms of the extent of reduction (δ). For instance, Wang et al. also reported significant H_2 (514 μmol g^{-1}) and O_2 (718 μmol g^{-1}) production from the

https://doi.org/10.1021/acscatal.4c03357
ACS Catal. 2024, 14, 14974−15013

Table 7. STCH Performance of Fe- and FeX-Based Perovskite Oxides under Inert Gas Conditions

composition	synthesis method	cycles	$\Delta\delta$	temp. red./ox. (°C)	time red./ox. (min)	H_2O (% vol)	gas red./ox.	O_2 yield (μmol g^{-1})	H_2 yield (μmol g^{-1})	average H_2 production rate (μmol g^{-1} min^{-1})	ref
$La_{0.6}Sr_{0.4}FeO_{3-\delta}$	commercial	5	0.030	1400/1400			N_2/N_2	327.2	124.0		97
$La_{0.6}Sr_{0.4}FeO_{3-\delta}$	commercial	1		1200/-	45/-		Ar/-	425.0			95
$La_{0.6}Sr_{0.4}FeO_{3-\delta}$	Pechini	1	0.170	1300/900	60/60	40.0	Ar/Ar	375.0	349.0	5.82	105
$BaFeO_{3-\delta}$	sol−gel	9		700/700	30/30	30.0	Ar/Ar		~216.85		137
$Ba_{0.95}La_{0.05}FeO_{3-\delta}$	sol−gel	9		500/500	30/30	30.0	Ar/Ar		~48.9		137
$Ba_{0.95}La_{0.05}FeO_{3-\delta}$	sol−gel	9		900/900	30/30	30.0	Ar/Ar		~1485.5		137
$BaFe_{0.975}Gd_{0.025}O_{3-\delta}$	sol−gel	9		700/700	30/30	30.0	Ar/Ar		~297.56		137
$La_{0.8}Al_{0.2}FeO_{3-\delta}$-acid pH	Pechini	1		1400/800	80/80	100.0	N_2/N_2		271.88[a]	3.40	138
$La_{0.8}Al_{0.2}FeO_{3-\delta}$-acid pH	Pechini	1		1200/800	80/80	100.0	N_2/N_2		19.53[a]	0.24	138
$La_{0.8}Al_{0.2}FeO_{3-\delta}$-acid pH	Pechini	1		1000/800	80/80	100.0	N_2/N_2		315.18[a]	3.94	138
$La_{0.8}Al_{0.2}FeO_{3-\delta}$-acid pH	Pechini	1		800/800	80/80	100.0	N_2/N_2		131.14[a]	1.64	138
$La_{0.8}Al_{0.2}FeO_{3-\delta}$-basic pH	Pechini	1		1400/800	80/80	100.0	N_2/N_2		19.53[a]	0.24	138
$La_{0.8}Al_{0.2}FeO_{3-\delta}$-basic pH	Pechini	1		1200/800	80/80	100.0	N_2/N_2		244.2[a]	3.05	138
$La_{0.8}Al_{0.2}FeO_{3-\delta}$-basic pH	Pechini	1		1000/800	80/80	100.0	N_2/N_2		308.04[a]	3.85	138
$La_{0.8}Al_{0.2}FeO_{3-\delta}$-basic pH	Pechini	1		800/800	80/80	100.0	N_2/N_2		131.14[a]	1.64	138
$Ba_{0.5}Sr_{0.5}Co_{0.2}Fe_{0.8}O_{3-\delta}$	solid-state	1		1000/-	30/-		Ar/-	630.0			95
$Ba_{0.5}Sr_{0.5}Co_{0.6}Fe_{0.4}O_{3-\delta}$	solid-state	1		1000/-	30/-		Ar/-	611.0			95
$Ba_{0.5}Sr_{0.5}Co_{0.8}Fe_{0.2}O_{3-\delta}$	Pechini	1		1000/800	30/45	80.0	Ar/Ar	600.0	102.0	2.27	95
$Ba_{0.5}Sr_{0.5}Co_{0.8}Fe_{0.2}O_{3-\delta}$	solid-state	1		1000/800	30/45	80.0	Ar/Ar	600.0	83.0	1.84	95
$Ba_{0.25}Sr_{0.75}Co_{0.8}Fe_{0.2}O_{3-\delta}$	solid-state	2		1000/800	30/45	80.0	Ar/Ar	700.0	74.0	1.64	95
$La_{0.8}Sr_{0.2}FeO_{3-\delta}$(25 wt %)/$SiO_2$	combustion	1		1350/1100	40/60	100.0	Ar/-	105.0[a]	126.2[a]	2.10	129
$La_{0.8}Ba_{0.2}FeO_{3-\delta}$(25 wt %)/$SiO_2$	combustion	1		1350/1100	40/60	100.0	Ar/-	100.6[a]	126.6[a]	2.11	129
$La_{0.8}Ce_{0.2}FeO_{3-\delta}$(25 wt %)/$SiO_2$	combustion	1		1350/1100	40/60	100.0	Ar/-	80.9[a]	85.9[a]	1.43	129
$LaFeO_{3-\delta}$(25 wt %)/SiO_2	combustion	1		1350/1100	40/15	100.0	Ar/-	88.3[a]	96.9[a]	6.46	129
$LaFeO_{3-\delta}$(25 wt %)/SiO_2	combustion	1		1350/1100	40/60	100.0	Ar/-	88.3[a]	130.5[a]	2.175	129
$LaFe_{0.95}Mn_{0.05}O_{3-\delta}$(25 wt %)/$SiO_2$	combustion	1		1350/1100	40/15	100.0	Ar/-		87.1[a]	5.81	129
$LaFe_{0.9}Mn_{0.1}O_{3-\delta}$(25 wt %)/$SiO_2$	combustion	1		1350/1100	40/15	100.0	Ar/-	117.6[a]	78.3[a]	5.22	129
$LaFe_{0.9}Mn_{0.1}O_{3-\delta}$(25 wt %)/$SiO_2$	combustion	1		1350/1100	40/60	100.0	Ar/-	117.6[a]	100.4[a]	1.67	129
$LaFe_{0.9}Ni_{0.1}O_{3-\delta}$(25 wt %)/$SiO_2$	combustion	1		1350/1100	40/60	100.0	Ar/-	93.3[a]	131.9[a]	2.20	129
$LaFe_{0.9}Al_{0.1}O_{3-\delta}$(25 wt %)/$SiO_2$	combustion	1		1350/1100	40/60	100.0	Ar/-	118.6[a]	115.2[a]	1.92	129
$LaFe_{0.8}Mn_{0.2}O_{3-\delta}$(25 wt %)/$SiO_2$	combustion	1		1350/1100	40/15	100.0	Ar/-		67.8[a]	4.52	129
$LaFe_{0.7}Mn_{0.3}O_{3-\delta}$(25 wt %)/$SiO_2$	combustion	1		1350/1100	40/15	100.0	Ar/-		50.0[a]	3.33	129
$LaFe_{0.6}Mn_{0.4}O_{3-\delta}$(25 wt %)/$SiO_2$	combustion	1		1350/1100	40/15	100.0	Ar/-		43.8[a]	2.92	129
$LaFe_{0.5}Mn_{0.5}O_{3-\delta}$(25 wt %)/$SiO_2$	combustion	1		1350/1100	40/15	100.0	Ar/-		35.3[a]	2.35	129
$CaTi_{0.7}Fe_{0.3}O_3$	solid-state			1400/1100	-/10	40.0	He/-		39.0	3.9	77

[a]Value converted from mL $g_{material}^{-1}$. Standard volume occupied: 22400 mL mol^{-1}.

$La_{0.6}Sr_{0.4}CoO_3$ perovskite under a temperature combination of 1300/900 °C. Furthermore, experimental observations have indicated that $La_{0.6}Sr_{0.4}CoO_3$ exhibits the highest formation of oxygen vacancies on the B-site when compared to Ni, Fe, Cr, and Mn. This indicates its potential as an active catalyst for H_2O splitting. Additionally, $La_{0.6}Sr_{0.4}CoO_3$ demonstrates the highest weight loss measured by TGA. However, after the cycle reaction, $La_{0.6}Sr_{0.4}CoO_3$ exhibits significant particle aggregation and a phase change.[105] $La_{0.8}Al_{0.2}CoO_{3-\delta}$ was synthesized using the Pechini method at various pH levels, as studied by Pérez et al. The research revealed that both the thermal reduction and hydrolysis stages induce permanent structural alterations when synthesized under acidic pH conditions. However, such changes are not observed when the synthesis takes place under basic pH conditions and the material is processed at 800 °C.[138] $La_{0.8}Sr_{0.2}CoO_3$ (LSC), with higher exergy (36%) and solar to fuel efficiencies (67%) according to the thermodynamic evaluation, stands out as a promising material in comparison to other reported materials. Moreover, LSC has stable hydrogen production during 20 consecutive cycles at 1000 °C, as shown in Figure 13; however, at a high reduction temperature (>1000 °C), the formation of the segregated Co_3O_4 phase is induced, resulting in a decrease in hydrogen production.[143]

Lanthanum−cobalt perovskites substituted in the A- or/and B-site were investigated. The cubic structure perovskite $Sr_2CoNb_{1-x}Ti_xO_{6-\delta}$ (x = 1.00, 0.70) exhibiting outstanding H_2 performance even at 700 °C were investigated by Prof. M.

https://doi.org/10.1021/acscatal.4c03357
ACS Catal. 2024, 14, 14974−15013

Table 8. Fe and FeX-based perovskite oxides STCH performance under reducing gas conditions

composition	synthesis method	cycles	temp. red./ox. (°C)	time red/.ox. (min)	H_2O (% vol)	gas red./ox.	O_2 yield (μmol g^{-1})	H_2 yield (μmol g^{-1})	average H_2 production rate (μmol g^{-1} min^{-1})	ref
$La_{0.7}Sr_{0.3}FeO_{3-\delta}$	sol−gel	3	1000/1000		100.0	He-CH_4/-		261.0		133
$La_{0.3}Sr_{0.7}FeO_{3-\delta}$	sol−gel	3	1000/1000		100.0	He-CH_4/-		123.0		133
$SrFeO_{3-\delta}$	sol−gel	3	1000/1000		100.0	He-CH_4/-	270.0	130.0		133
$LaFeO_{3-\delta}$	sol−gel	3	1000/-			He-CH_4/-	530.0			133
$La_{0.6}Sr_{0.4}FeO_{3-\delta}$	sol−gel	2	1000/1000	-/20	3.0	[a]N_2−H_2/N_2	427.3[b]	3359.0[c]	167.95	96
$La_{0.6}Sr_{0.4}Mn_{0.8}Fe_{0.2}O_{3-\delta}$	sol−gel	2	1000/1000	-/20	3.0	[a]N_2−H_2/N_2	286.0[b]	1205.0[c]	60.25	96
$La_{0.6}Sr_{0.4}Mn_{0.6}Fe_{0.4}O_{3-\delta}$	sol−gel	2	1000/1000	-/20	3.0	[a]N_2−H_2/N_2	280.0[b]	1645.0[c]	82.25	96
$La_{0.6}Sr_{0.4}Mn_{0.4}Fe_{0.6}O_{3-\delta}$	sol−gel	2	1000/1000	-/20	3.0	[a]N_2−H_2/N_2	333.2[b]	2827.0[c]	141.35	96
$BaFeO_{3-\delta}$	sol−gel	9	500/500	30/30	30.0	10%H_2−Ar/Ar		∼26.43		137
$BaFeO_{3-\delta}$	sol−gel	9	900/900	30/30	30.0	10%H_2−Ar/Ar		∼1285.8		137
$Ba_{0.95}La_{0.05}FeO_{3-\delta}$	sol−gel	9	700/700	30/30	30.0	10%H_2−Ar/Ar		∼370.2		137
$BaFe_{0.975}Gd_{0.025}O_{3-\delta}$	sol−gel	9	500/500	30/30	30.0	10%H_2−Ar/Ar		∼42.84		137
$BaFe_{0.975}Gd_{0.025}O_{3-\delta}$	sol−gel	9	900/900	30/30	30.0	10%H_2−Ar/Ar		∼737.28		137

[a]5 vol % H_2 stream. [b]Results from TGA analysis. [c]Introduction of steam began at 60 °C while ramping to 1000 °C

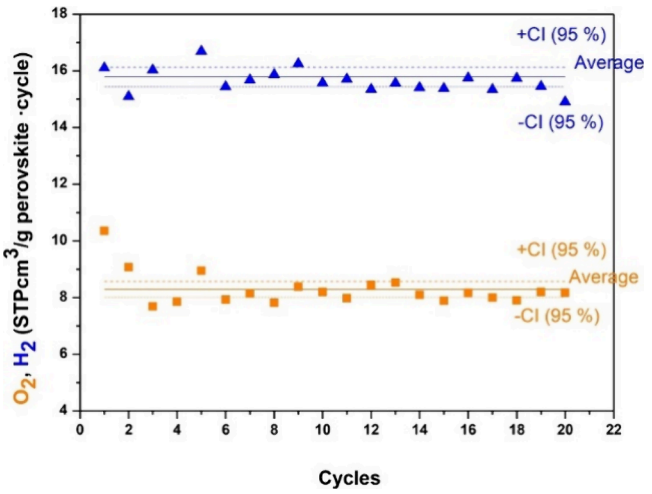

Figure 13. Performance of LSC materials in 20 thermochemical cycles. This involves assessing oxygen release at 1000 °C and hydrogen release at 800 °C.[143] Reproduced from ref 143. Available under a Creative Commons CC-BY license. Copyright 2022 M. Orfila and co-workers.

Teresa Azcondo et al. They also found a $Sr_2CoNb_{0.3}Ti_{0.7}O_{6-\delta}$ material that maintained its remarkable performance upon cycling. The Mn perovskite undergoes thermal reduction at temperatures exceeding 1000 °C, while the Co material requires 800 °C and the Fe material requires 900 °C. Additionally, after eight thermochemical reactions at 700 °C, $Sr_2CoNb_{0.30}Ti_{0.70}O_{6-\delta}$ showed the highest ever reported hydrogen production of 410 μmol g^{-1}.[144] Perovskite $La_{0.6}Sr_{0.4}Cr_{1-x}Co_xO_3$ used in water-splitting was first reported by A. H. Bork et al. They exhibit that there is a trade-off in doping: the introduction of cobalt dopants enhances the liberation of oxygen during the initial high-temperature reduction phase; however, this advantage is counterbalanced by the less advantageous thermodynamics observed during the subsequent second step involving water-splitting at lower temperatures.[145] Sr- and Co-doped $LaGaO_{3-\delta}$ was successfully investigated in thermochemical water-splitting (TCWS) by Can Li's group. They found that the oxygen vacancy concentration (δ) increased with the content of the Sr and Co dopants. The catalyst IrO_x, doped into the LGC50 structure, was found to increase the hydrogen release rate by 1.3-fold. XPS analysis revealed that the water-splitting reaction was driven by Co^{2+}/Co^{3+} ions. The oxygen vacancy formation energies (Ev) were predicted using DFT calculations, which found that E_v is from about 0.7 to nearly 5.3 eV at 1623 K under vacuum conditions. However, under the evaluation conditions, the low water-to-hydrogen conversion (less than 1%) is still far away from the practical needs.[119] In a study by Park et al., the perovskite $Gd_{0.5}La_{0.5}Co_{0.5}Fe_{0.5}O_3$ was identified as a promising water-splitting catalyst through computational analysis, and its efficacy was subsequently confirmed experimentally. In water-splitting assessments conducted at a thermal reduction temperature of 1350 °C, the reoxidation temperatures of 850 and 1000 °C yielded hydrogen outputs of 101 and 141 μmol g^{-1}, respectively, with a progressive enhancement in production across successive cycles.[146] Table 9 provides a detailed overview of the solar thermochemical hydrogen (STCH) production performance of Co- and CoX-based perovskite oxides.

5.6. Other Perovskite Oxides as Redox-Active Oxygen Exchange Materials. Nickel (Ni) was studied as a B-site element in perovskites. Huijun Zhao's group elucidated the linear relationship between H_2 generation and the extent of oxygen vacancy (δ) in $La_{0.6}Sr_{0.4}BO_3$ (B = Mn, Cr, Fe, Co, and Ni). Additionally, the LSB perovskites possessing lower V_o formation energies can achieve higher levels of V_o formation and oxygen evolution. Notably, the H_2 production (368 μmol

https://doi.org/10.1021/acscatal.4c03357
ACS Catal. 2024, 14, 14974−15013

Table 9. STCH Performance of Co- and CoX-Based Perovskite Oxides

composition	synthesis method	cycles	$\Delta\delta$	temp. red./ox. (°C)	time red./ox. (min)	H_2O (%vol)	gas red./ox.	O_2 yield (μmol g^{-1})	H_2 yield (μmol g^{-1})	average H_2 production rate (μmol g^{-1} min^{-1})	ref
$La_{0.8}Sr_{0.2}CoO_{3-\delta}$	commercial	1		1200/-	45/-		Ar/-	732.0			95
$La_{0.6}Sr_{0.4}Fe_{0.8}Co_{0.2}O_{3-\delta}$	commercial	2		1200/800	45/45	80.0	Ar/Ar	503.0	90.0	2.00	95
$La_{0.6}Sr_{0.4}Fe_{0.8}Co_{0.2}O_{3-\delta}$	Pechini	2		1200/800	45/45	80.0	Ar/Ar	503.0	162.0	3.60	95
$La_{0.8}Sr_{0.2}CoO_{3-\delta}$	commercial	5	0.220	1400/1400			N_2/N_2	492.7	272.8		97
$La_{0.8}Ca_{0.2}CoO_{3-\delta}$	Pechini	1		1300/900	60/60	40.0	Ar/Ar	715.0	496.0	8.27	142
$La_{0.6}Ca_{0.4}CoO_{3-\delta}$	Pechini	5		1300/900	60/60	40.0	Ar/Ar	832.5	587.0	9.78	142
$La_{0.4}Ca_{0.6}CoO_{3-\delta}$	Pechini	1		1300/900	60/60	40.0	Ar/Ar	157.5	472.0	7.87	142
$La_{0.2}Ca_{0.8}CoO_{3-\delta}$	Pechini	1		1300/900	60/60	40.0	Ar/Ar	1213.0	204.0	3.40	142
$La_{0.6}Sr_{0.4}CoO_{3-\delta}$	Pechini	5	0.330	1300/900	60/60	40.0	Ar/Ar	718.0	514.0	8.57	105
$La_{0.6}Sr_{0.4}CrO_{3-\delta}$	Pechini	1	0.072	1300/900	60/60	40.0	Ar/Ar	166.0	280.0	4.67	105
$La_{0.6}Sr_{0.4}NiO_{3-\delta}$	Pechini	1	0.200	1300/900	60/60	40.0	Ar/Ar	437.0	368.0	6.13	105
$La_{0.8}Al_{0.2}CoO_{3-\delta}$-acid pH	Pechini	1		1400/800	80/80	100.0	N_2/N_2		503.57[a]	6.29	138
$La_{0.8}Al_{0.2}CoO_{3-\delta}$-acid pH	Pechini	1		1200/800	80/80	100.0	N_2/N_2		239.73[a]	3.00	138
$La_{0.8}Al_{0.2}CoO_{3-\delta}$-acid pH	Pechini	1		1000/800	80/80	100.0	N_2/N_2		16.74[a]	0.21	138
$La_{0.8}Al_{0.2}CoO_{3-\delta}$-acid pH	Pechini	1		800/800	80/80	100.0	N_2/N_2		136.72[a]	1.71	138
$La_{0.8}Al_{0.2}CoO_{3-\delta}$-basic pH	Pechini	1		1400/800	80/80	100.0	N_2/N_2		366.96[a]	4.59	138
$La_{0.8}Al_{0.2}CoO_{3-\delta}$-basic pH	Pechini	1		1200/800	80/80	100.0	N_2/N_2		213.39[a]	2.67	138
$La_{0.8}Al_{0.2}CoO_{3-\delta}$-basic pH	Pechini	1		1000/800	80/80	100.0	N_2/N_2		309.71[a]	3.87	138
$La_{0.8}Al_{0.2}CoO_{3-\delta}$-basic pH	Pechini	1		800/800	80/80	100.0	N_2/N_2		133.93[a]	1.67	138
$La_{0.8}Sr_{0.2}CoO_{3-\delta}$	commercial	1		1400/800		100.0	N_2/N_2	915.18[a]	296.34[a]		143
$La_{0.8}Sr_{0.2}CoO_{3-\delta}$	commercial	1		1200/800		100.0	N_2/N_2	618.3[a]	279.02[a]		143
$La_{0.8}Sr_{0.2}CoO_{3-\delta}$	commercial	1		1000/800		100.0	N_2/N_2	461.16[a]	717.41[a]		143
$La_{0.8}Sr_{0.2}CoO_{3-\delta}$	commercial	1		800/800		100.0	N_2/N_2	11.01[a]	3.67[a]		143
$La_{0.8}Sr_{0.2}CoO_{3-\delta}$	commercial	20		1000/800		100.0	N_2/N_2	364.73[a]	665.18[a]		143
$Sr_2CoNb_{0.3}Ti_{0.7}O_{6-\delta}$	Pechini	1		700/700		100.0	N_2/N_2	235.29	450.0		144
$Sr_2CoNb_{0.3}Ti_{0.7}O_{6-\delta}$	Pechini	8		700/700		100.0	N_2/N_2	200.78	410.0		144
$Sr_2CoTiO_{6-\delta}$	Pechini	1		700/700		100.0	N_2/N_2	260.68	492.0		144
$Sr_2CoTiO_{6-\delta}$	Pechini	8		700/700		100.0	N_2/N_2	181.55	238.18		144
$LaGaO_{3-\delta}$	combustion	1	0.010	1350/650	40/-	100.0	Ar/-	2.0	6.0		119
$LaGa_{0.99}Co_{0.01}O_{3-\delta}$	combustion	1	0.010	1350/650	40/-	100.0	Ar/-	26.0	8.0		119
$LaGa_{0.9}Co_{0.1}O_{3-\delta}$	combustion	1	0.044	1350/650	40/-	100.0	Ar/-	75.0	146.0		119
$LaGa_{0.85}Co_{0.15}O_{3-\delta}$	combustion	1		1350/650	40/-	100.0	Ar/-	90.0	128.0		119
$LaGa_{0.8}Co_{0.2}O_{3-\delta}$	combustion	1	0.056	1350/650	40/-	100.0	Ar/-	116.0	185.0		119
$LaGa_{0.7}Co_{0.3}O_{3-\delta}$	combustion	1	0.084	1350/650	40/-	100.0	Ar/-	172.0	254.0		119
$LaGa_{0.6}Co_{0.4}O_{3-\delta}$	combustion	1	0.106	1350/650	40/-	100.0	Ar/-	203.0	329.0		119
$LaGa_{0.5}Co_{0.5}O_{3-\delta}$	combustion	1	0.137	1350/550	40/-	100.0	Ar/-	227.0	258.0		119
$LaGa_{0.5}Co_{0.5}O_{3-\delta}$	combustion	1	0.137	1350/650	40/-	100.0	Ar/-	268.0	406.0		119
$LaGa_{0.5}Co_{0.5}O_{3-\delta}$	combustion	1	0.137	1350/700	40/-	100.0	Ar/-	260.0	440.0		119
$LaGa_{0.5}Co_{0.5}O_{3-\delta}$	combustion	1	0.137	1350/800	40/-	100.0	Ar/-	272.0	450.0		119
$LaGa_{0.5}Co_{0.5}O_{3-\delta}$	combustion	1	0.137	1350/900	40/-	100.0	Ar/-	256.0	440.0		119
$LaGa_{0.5}Co_{0.5}O_{3-\delta}$	combustion	1	0.137	1350/1000	40/-	100.0	Ar/-	246.0	328.0		119
$LaGa_{0.5}Co_{0.5}O_{3-\delta}$	combustion	1	0.137	1350/1100	40/-	100.0	Ar/-	202.0	301.0		119
$LaGa_{0.5}Co_{0.5}{}^{\circ}{}_{3-\delta}$-Ir(0.5 atom %)	combustion	1		1350/800	40/100	100.0	Ar/-	268.0	363.0	3.63	119
$LaGa_{0.5}Co_{0.5}O_{3-\delta}$-Ir(1.0 atom %)	combustion	1	0.131	1350/800	40/100	100.0	Ar/-	274.0	413.0	4.13	119
$LaGa_{0.5}Co_{0.5}O_{3-\delta}$-Ir(1.5 atom %)	combustion	1		1350/800	40/100	100.0	Ar/-	274.0	337.0	3.37	119
$LaGa_{0.4}Co_{0.6}O_{3-\delta}$	combustion	3	0.156	1350/800	40/400	100.0	Ar/-	313.0	478.0	1.20	119
$LaGa_{0.3}Co_{0.7}O_{3-\delta}$	combustion	1	0.160	1350/800	40/530	100.0	Ar/-	321.0	196.0	0.37	119
$LaCoO_{3-\delta}$	combustion	1	0.245	1350/800	40/250	100.0	Ar/-	500.0	69.0	0.28	119
$La_{0.9}Sr_{0.1}GaO_{3-\delta}$	combustion	1	0.137	1350/800	40/-	100.0	Ar/-	4.0	4.0		119
$La_{0.9}Sr_{0.1}Ga_{0.5}Co_{0.5}O_{3-\delta}$	combustion	1	0.160	1350/800	40/-	100.0	Ar/-	328.0	215.0		119
$La_{0.7}Sr_{0.3}Ga_{0.5}Co_{0.5}O_{3-\delta}$	combustion	1	0.167	1350/1000	40/-	100.0	Ar/-	355.0	45.0		119
$La_{0.5}Sr_{0.5}Ga_{0.5}Co_{0.5}O_{3-\delta}$	combustion	1		1350/1000	40/-	100.0	Ar/-	379.0	4.0		119
$Gd_{0.5}La_{0.5}Co_{0.5}Fe_{0.5}O_3$	solid-state	1		1350/850	5.5/20	40.0	Ar/Ar	261.0	67.0	3.35	146
$Gd_{0.5}La_{0.5}Co_{0.5}Fe_{0.5}O_3$	solid-state	2		1350/850	5.5/20	40.0	Ar/Ar	87.0	90.0	4.50	146
$Gd_{0.5}La_{0.5}Co_{0.5}Fe_{0.5}O_3$	solid-state	3		1350/850	5.5/20	40.0	Ar/Ar	74.0	101.0	5.05	146
$Gd_{0.5}La_{0.5}Co_{0.5}Fe_{0.5}O_3$	solid-state	4		1350/850	5.5/20	40.0	Ar/Ar	69.0	-	-	146
$Gd_{0.5}La_{0.5}Co_{0.5}Fe_{0.5}O_3$	solid-state	1		1350/1000	5.5/20	40.0	Ar/Ar	125.0	127.0	6.35	146

https://doi.org/10.1021/acscatal.4c03357
ACS Catal. 2024, 14, 14974−15013

Table 9. continued

composition	synthesis method	cycles	$\Delta\delta$	temp. red./ox. (°C)	time red./ox. (min)	H_2O (%vol)	gas red./ox.	O_2 yield (μmol g^{-1})	H_2 yield (μmol g^{-1})	average H_2 production rate (μmol g^{-1} min^{-1})	ref
$Gd_{0.5}La_{0.5}Co_{0.5}Fe_{0.5}O_3$	solid-state	2		1350/1000	5.5/20	40.0	Ar/Ar	93.0	141.0	7.05	146
$Gd_{0.5}La_{0.5}Co_{0.5}Fe_{0.5}O_3$	solid-state	3		1350/1000	5.5/20	40.0	Ar/Ar	87.0	-	-	146
$LaFe_{0.9}Co_{0.1}O_{3-\delta}$(25 wt %)/$SiO_2$	combustion	1		1350/1100	40/15	100.0	Ar/-	104.2[a]	108.0[a]	7.20	129
$LaFe_{0.9}Co_{0.1}O_{3-\delta}$(25 wt %)/$SiO_2$	combustion	1		1350/1100	40/60	100.0	Ar/-	104.2[a]	155.1[a]	2.59	129
$LaFe_{0.8}Co_{0.2}O_{3-\delta}$(10 wt %)/$SiO_2$	combustion	1		1350/1100	40/60	100.0	Ar/-	45.0[a]	57.8[a]	0.96	129
$LaFe_{0.8}Co_{0.2}O_{3-\delta}$(25 wt %)/$SiO_2$	combustion	1		1350/1100	40/15	100.0	Ar/-	125.2[a]	128.9[a]	8.59	129
$LaFe_{0.8}Co_{0.2}O_{3-\delta}$(25 wt %)/$SiO_2$	combustion	9		1350/1100	40/60	100.0	Ar/-	125.2[a]	188.3[a]	3.14	129
$LaFe_{0.8}Co_{0.2}O_{3-\delta}$(50 wt %)/$SiO_2$	combustion	1		1350/1100	40/60	100.0	Ar/-	203.5[a]	351.4[a]	5.86	129
$LaFe_{0.8}Co_{0.2}O_{3-\delta}$(75 wt %)/$SiO_2$	combustion	1		1350/1100	40/60	100.0	Ar/-	53.6[a]	10.8[a]	0.18	129
$LaFe_{0.7}Co_{0.3}O_{3-\delta}$(25 wt %)/$SiO_2$	combustion	1		1350/1100	40/15	100.0	Ar/-		117.4[a]	7.83	129
$LaFe_{0.6}Co_{0.4}O_{3-\delta}$(25 wt %)/$SiO_2$	combustion	1		1350/1100	40/15	100.0	Ar/-		115.4[a]	7.69	129
$LaFe_{0.5}Co_{0.5}O_{3-\delta}$(25 wt %)/$SiO_2$	combustion	1		1350/1100	40/15	100.0	Ar/-		77.3[a]	5.15	129

[a]Value converted from mL $g_{material}^{-1}$. Standard volume occupied: 22400 mL mol^{-1}.

g^{-1}) of $La_{0.6}Sr_{0.4}NiO_{3-\delta}$ was found to be competitive when compared to other B-site elements (Cr, Mn, and Fe).[105] Alejandro Perez et al. also found the promising performance of Ni-based perovskite $La_{0.8}Al_{0.2}NiO_{3-\delta}$ in H_2 production (196 μmol g^{-1}) at an isothermal temperature (800 °C). Furthermore, the $La_{0.8}Al_{0.2}NiO_{3-\delta}$ perovskite demonstrates excellent performance in terms of solar/fuel efficiency with a ratio of 0.46. This ratio represents the potential energy recovery from the produced hydrogen compared to the solar heat required for its production, and it is comparable to or even higher than values reported in the literature for other metal oxides. However, $La_{0.8}Al_{0.2}NiO_{3-\delta}$ perovskites prepared at acidic pH undergo irreversible changes in their crystalline structure during both the thermal reduction and hydrolysis steps.[138] The perovskite materials $La_{0.6}Sr_{0.4}NiO_{3-\delta}$ were studied with chromium (Cr) as a B-site element. Compared to Mn in the B-site, the Cr-based perovskite exhibits a higher extent of oxygen vacancy formation in the $La_{0.6}Sr_{0.4}B$ (B = Cr, Mn) system, and the hydrogen production of the Cr-based perovskite is also higher than that of the Mn-based perovskite. This also meets the correlation between the H_2 production and the extent of oxygen vacancy formation.[105] Xin Li's group also designed a Cr perovskite via the oxygen vacancy mechanism analysis and doping-mixture modification for solar thermochemical water-splitting.[147] Alejandro Perez et al. also investigated Cu in the B-site, $La_{0.8}Al_{0.2}CuO_{3-\delta}$, and it was found that while reducing the temperature to 1400 °C is thermodynamically favorable, the hydrogen production is lower compared to temperatures of 1200 and 1000 °C. Additionally, when comparing the B-site metals Co, Ni, Fe, and Cu, Cu exhibits the lowest hydrogen production at a given temperature.[138]

High-entropy oxides (HEOs), a novel category of materials discovered in 2015, have garnered significant attention in recent years.[148] A high-entropy oxide is defined as a multicationic oxide featuring a random and homogeneous cation distribution that is entropy-stabilized within a single sublattice. The key criteria for HEO classification include the mixing of typically five or more cations in equimolar amounts (on at least one sublattice) to optimize the configurational entropy and parent oxides exhibiting distinct crystal structures with low mutual solubility.[149] While most initial studies of HEOs focus on equimolar compositions where the configurational entropy is maximized ($\ln(N)k_B$ per cation, where N is the number of equimolar components and k_B is the Boltzmann constant), high-entropy oxides (or ceramics in general) are extended to compositionally complex oxides (CCOs) or ceramics (CCCs) to include nonequimolar compositions, as well as long- and short-range orders, which reduce the configurational entropy but offer more opportunities to tune and improve properties to outperform their equimolar higher-entropy counterparts.[150,151] The intrinsic configurational disorder within these compounds paves the way for innovative pathways to design and discover multiple new crystalline material phases. In 2018, Jian Luo's group first reported the fabrication of high-entropy perovskite oxides (HEPOs),[56] which soon attracted interest because of their catalytic, dielectric, magnetic, ionic, ferroelectric, and other properties with vast tunability. To enhance the efficiency of fuel generation per cycle and achieve favorable kinetic rates, Alex Le Gal et al. delved into an investigation of a series of seven HEOs, including two HEPOs ($(Gd_{0.2}La_{0.2}Nd_{0.2}Sm_{0.2}Y_{0.2})(Co_{0.2}Cr_{0.2}Fe_{0.2}Mn_{0.2}Ni_{0.2})O_3$, $(La_{0.5}Sr_{0.5})(Mn_{0.2}Ce_{0.2}Ni_{0.2}Mg_{0.2}Cr_{0.2})O_3$) and nonequimolar $(La_{0.8}Sr_{0.2})(Mn_{0.2}Fe_{0.2}Co_{0.4}Al_{0.2})O_{3-\delta}$, to improve the fuel generation with good kinetic rates.[149] The CO production of these HEPOs is higher than that of ceria but still far from the production yield of $LaSrMnO_3$ perovskites.[149] Dawei Zhang et al. investigated the impact of aliovalent doping, differentiating between normal and abnormal cases, on the redox behaviors observed in compositionally complex perovskite oxides (CCPOs). They discovered two series of medium-entropy CCPOs, namely, $(La_{1-x}Sr_x)(Mn_{1/3}Fe_{1/3}Ti_{1/3})O_{3-\delta}$ (LS_MFT) and $(La_{1-x}Sr_x)(Mn_{1/3}Fe_{1/3}Cr_{1/3})O_{3-\delta}$ (LS_MFC). They observed a linear relationship between the extent of reduction ($\Delta\delta$) and the Sr molar ratio in LS_MFC, as well as a V-shaped correlation between $\Delta\delta$ and the Sr molar ratio in LS_MFT. The explanation is as follows: In LS_MFC, the energy shifts of

https://doi.org/10.1021/acscatal.4c03357
ACS Catal. 2024, 14, 14974−15013

the Cr−$L_{2,3}$, Mn−$L_{2,3}$, and Fe−$L_{2,3}$ peak toward higher values as x increases, indicating elevated oxidation states for Cr, Mn, and Fe, along with decreased oxygen vacancy formation energies. In LS_MFT, the V-shaped curve of $\Delta\delta$ vs x is attributed to the stable Ti^{4+} state and the V-shaped dependence of the Mn/Fe valency on x.[37]

In addition, Zhang et al. studied the STCH performance of $(La_{0.8}Sr_{0.2})(Mn_{(1-x)/3}Fe_{(1-x)/3}Co_xAl_{(1-x)/3})O_3$ (LS_MFC$_x$A) and found that LS_MFC$_x$A has tunable thermodynamic and kinetics properties. They reported that the extent of reduction ($\Delta\delta$) increases with the increasing Co content (x), but at the same time there is a decreasing trend in the intrinsic kinetics (oxygen surface exchange coefficient, K_{ex}), as shown in Figure 14.[27]

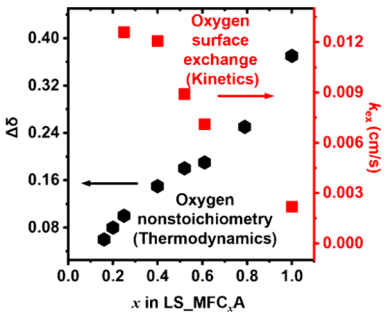

Figure 14. Relationship between $\Delta\delta$ and K_{ex} on the Co content in LS_MFC$_x$A.[27] Reproduced from ref 27. Copyright 2023 American Chemical Society.

In B-site elements, the preferential redox element was found to be Co by in situ XPS and TGA. The DFT calculation result shows that oxygen vacancies tend to form near positions where Co is the first nearest neighbor. The analysis of the magnetic moments of the B-site metals also confirms that the Co redox valence change exhibits the highest activity when oxygen vacancies are formed. Furthermore, the bond valence sum (BVS) results indicate a notable weakening of Co−O bonds, slight weakening of Mn−O and Al−O bonds, and strengthening of Fe−O bonds.[27]

Cijie Liu et al. reported a new series of A-site high-entropy HPEOs, $(La_{1/6}Pr_{1/6}Nd_{1/6}Gd_{1/6}Sr_{1/6}Ba_{1/6})MnO_3$ (LPNGSB_Mn), for STCH that show desirable thermodynamic and kinetics properties as well as excellent phase stability and cycling durability. LPNGSB_Mn exhibits enhanced hydrogen production (~77.5 mmol mol_{oxide}^{-1}) compared to $(La_{2/3}Sr_{1/3})MnO_3$ (~53.5 mmol mol_{oxide}^{-1}) in a short 1 h redox duration and high STCH production and phase stability for 50 cycles. This work provides a new pathway to explore A-sites with tunable redox, thermodynamic, and kinetics properties of oxides for STCH and chemical looping.[152] Table 10 summarizes the STCH production performance of various perovskite oxides.

5.7. Discussion on the Role of Inert and Reductant Gases. Inert gases, such as argon and nitrogen, are primarily used to lower the partial pressure of oxygen, thereby facilitating redox reactions in materials.[27,138,152] The main energy requirements associated with using inert gases include heating the gas to the reaction temperature and separating the generated oxygen afterward.[153]

Reductant gases, such as hydrogen or methane, play an active role in redox reactions, often enhancing oxygen release.[154,155] When methane is used as the reductant, it prompts the material to release lattice oxygen, which is fully reabsorbed when oxygen is reintroduced at the same temperature.[133] Additionally, methane consumes the permeated oxygen and produces valuable compounds, such as synthesis gas.[154,155] Hydrogen is sometimes used in reactions to simulate an up-scale scenario, as high hydrogen concentrations are present during actual experiments. It is also occasionally used as a pretreatment gas, which can affect the crystalline structure of the material.[96]

5.8. Comparative Analysis of Perovskite Families and Ceria: Pros, Cons, and Future Development. In this section, we provide a comparative analysis of different perovskite oxide families and ceria, focusing on their advantages and disadvantages, current development status, and potential for overcoming existing challenges, as shown in Table 11.

Perovskite oxides are emerging as promising materials for STCH due to their high oxygen exchange capacity. Mn-based perovskites exhibit notable redox activity and ionic conductivity, but excessive Sr doping can reduce reoxidation yields. MnAl-based perovskites have enhanced reoxidation efficiencies and an increased extent of reduction but may also suffer from high Sr doping levels, which can negatively affect the redox activity. MnX-based perovskites, doped with Ce and Cr, show high hydrogen yields but face challenges in secondary phase formation. Fe- and FeX-based perovskites, particularly $La_{1-x}Sr_xFeO_3$, are advantageous for their lower reduction temperatures, though issues with sintering and structural changes persist. Co- and CoX-based perovskites are recognized for their high oxygen release and hydrogen production, but cobalt's toxicity and cost are concerns. Other perovskite types, including high-entropy oxides, offer competitive performance but also face challenges such as irreversible structural changes.

Ceria, on the other hand, has been extensively studied as a mature material for STCH, with significant contributions from Aldo Steinfeld's group. Their work, particularly on the reticulated porous ceramic (RPC) foam structured CeO_2, featuring dual-scale porosity and composed entirely of pure CeO_2, was utilized in a solar cavity-type reactor.[156,157]

Each oxide type has distinct advantages and drawbacks. Mn-based perovskites are highly reactive but suffer from stability issues, while MnAl-based variants show better thermal stability but are complex to synthesize. MnX-based perovskites benefit from additional doping, but they face performance consistency challenges. Fe-based perovskites are cost-effective but typically have lower efficiency in oxygen exchange. Co-based perovskites are stable with high reactivity, though cobalt's toxicity is a concern. Other perovskites exhibit varied performance characteristics and stability. Ceria, while offering excellent thermal stability, suffers from a low extent of stoichiometry.

While perovskite oxides demonstrate promising properties for STCH applications, it is important to note that current research, including this study, has primarily been conducted under laboratory conditions.[26,27,39,78,152] In contrast, state-of-the-art materials like CeO_2 have been successfully tested in upscaled reactor systems powered by concentrated solar energy.[15,34,36,101] Future research should focus on scaling up the testing of perovskite materials under real-world conditions to better evaluate their performance in practical applications. Additionally, the relatively low steam-to-hydrogen conversion efficiency and incomplete reoxidation yield observed in perovskite oxides highlight the need for further exploration and optimization.[158] Advances in high-entropy and composi-

https://doi.org/10.1021/acscatal.4c03357
ACS Catal. 2024, 14, 14974−15013

Table 10. STCH Performance of Selected Other Perovskite Oxides

composition	synthesis method	cycles	$\Delta\delta$	temp. red./ox. (°C)	time red./ox. (min)	H_2O (% vol)	gas red./ox.	O_2 yield (μmol g^{-1})	H_2 yield (μmol g^{-1})	average H_2 production rate (μmol g^{-1} min^{-1})	ref
$La_{0.6}Sr_{0.4}NiO_{3-\delta}$	modified Pechini	1	0.200	1300/900	60/60	40.0	Ar/Ar	437.0	368.0	6.13	105
$La_{0.8}Al_{0.2}NiO_{3-\delta}$	modified Pechini	5		1400/800	80/60	100.0	N_2/N_2		111.61	1.86	138
$La_{0.8}Al_{0.2}NiO_{3-\delta}$	modified Pechini	5		1200/800	80/60	100.0	N_2/N_2		200.89	3.35	138
$La_{0.8}Al_{0.2}NiO_{3-\delta}$	modified Pechini	5		1000/800	80/60	100.0	N_2/N_2		380.58	6.34	138
$La_{0.8}Al_{0.2}NiO_{3-\delta}$	modified Pechini	5		800/800	80/60	100.0	N_2/N_2	94.87	196	3.27	138
$La_{0.6}Sr_{0.4}CrO_{3-\delta}$	modified Pechini	1	0.072	1300/900	60/60	40.0	Ar/Ar	166.0	280.0	4.67	105
$YCr_{0.9}Zr_{0.1}O_{3-\delta}$	sol−gel	1		1400/1300	/40		Ar/Ar		207.6	5.19	147
$YCr_{0.75}Zr_{0.25}O_{3-\delta}$	sol−gel	1		1400/1300	/40		Ar/Ar		219.6	5.49	147
$YCr_{0.6}Zr_{0.4}O_{3-\delta}$	sol−gel	1		1400/1300	/40		Ar/Ar		206	5.15	147
$YCr_{0.75}Zr_{0.25}O_{3-\delta}$-10 wt % CeO_2	sol−gel	1		1400/1300	/40		Ar/Ar		209.7	5.24	147
$YCr_{0.75}Zr_{0.25}O_{3-\delta}$-25 wt % CeO_2	sol−gel	1		1400/1300	/40		Ar/Ar		298.7	7.47	147
$YCr_{0.75}Zr_{0.25}O_{3-\delta}$-25 wt % CeO_2	sol−gel	1		1400/1300	40/60		Ar/Ar		449.8	11.25	147
$YCr_{0.75}Zr_{0.25}O_{3-\delta}$-50 wt % CeO_2	sol−gel	1		1400/1300	/40		Ar/Ar		174.6	4.37	147
$YCr_{0.9}Zr_{0.1}O_{3-\delta}$	sol−gel	3		1400/1300	/40		Ar/Ar		193.8	4.85	147
$YCr_{0.75}Zr_{0.25}O_{3-\delta}$	sol−gel	3		1400/1300	/40		Ar/Ar		210.9	5.27	147
$YCr_{0.6}Zr_{0.4}O_{3-\delta}$	sol−gel	3		1400/1300	/40		Ar/Ar		204.3	5.11	147
$YCr_{0.75}Zr_{0.25}O_{3-\delta}$-10 wt % CeO_2	sol−gel	3		1400/1300	/40		Ar/Ar		211.4	5.29	147
$YCr_{0.75}Zr_{0.25}O_{3-\delta}$-25 wt % CeO_2	sol−gel	3		1400/1300	/40		Ar/Ar		256.7	6.42	147
$YCr_{0.75}Zr_{0.25}O_{3-\delta}$-50 wt % CeO_2	sol−gel	3		1400/1300	/40		Ar/Ar		163.7	4.09	147
$YCr_{0.75}Zr_{0.25}O_{3-\delta}$-25 wt % CeO_2	sol−gel	10		1400/1300	/40		Ar/Ar		244.6	6.12	147
$La_{0.8}Al_{0.2}CuO_{3-\delta}$	modified Pechini	5		1400/800	80/60	100.0	N_2/N_2		22.32	0.37	138
$La_{0.8}Al_{0.2}CuO_{3-\delta}$	modified Pechini	5		1200/800	80/60	100.0	N_2/N_2		156.25	2.60	138
$La_{0.8}Al_{0.2}CuO_{3-\delta}$	modified Pechini	5		1000/800	80/60	100.0	N_2/N_2		178.57	2.98	138
$La_{0.8}Al_{0.2}CuO_{3-\delta}$	modified Pechini	5		800/800	80/60	100.0	N_2/N_2	50.223	93.75	1.56	138
$(La_{0.8}Sr_{0.2})(Mn_{0.28}Fe_{0.28}Co_{0.16}Al_{0.28})O_{3-\delta}$	solid-state	4	0.057	1350/1100	45/15	40.0	N_2/N_2		125.0	8.30	27
$(La_{0.8}Sr_{0.2})(Mn_{0.267}Fe_{0.267}Co_{0.20}Al_{0.267})O_{3-\delta}$	solid-state	4	0.081	1350/1100	45/15	40.0	N_2/N_2		135.0	9.00	27
$(La_{0.8}Sr_{0.2})(Mn_{0.25}Fe_{0.25}Co_{0.25}Al_{0.25})O_{3-\delta}$	solid-state	4	0.097	1350/1100	45/15	40.0	N_2/N_2		162.0	10.80	27
$(La_{0.8}Sr_{0.2})(Mn_{0.2}Fe_{0.2}Co_{0.4}Al_{0.2})O_{3-\delta}$	solid-state	4	0.14	1350/1100	45/15	40.0	N_2/N_2		219.0	14.60	27
$(La_{0.8}Sr_{0.2})(Mn_{0.16}Fe_{0.16}Co_{0.52}Al_{0.16})O_{3-\delta}$	solid-state	4	0.18	1350/1100	45/15	40.0	N_2/N_2		189.0	12.60	27
$(La_{0.8}Sr_{0.2})(Mn_{0.13}Fe_{0.13}Co_{0.61}Al_{0.13})O_{3-\delta}$	solid-state	4	0.19	1350/1100	45/15	40.0	N_2/N_2		148.0	9.87	27
$(La_{0.8}Sr_{0.2})(Mn_{0.07}Fe_{0.07}Co_{0.79}Al_{0.07})O_{3-\delta}$	solid-state	4	0.28	1350/1100	45/15	40.0	N_2/N_2		25.0	1.67	27
$(La_{0.8}Sr_{0.2})(Mn_{0.2}Fe_{0.2}Co_{0.4}Al_{0.2})O_{3-\delta}$	solid-state	4	0.14	1350/800	45/15	40.0	N_2/N_2		49.0	3.27	27
$(La_{0.8}Sr_{0.2})(Mn_{0.2}Fe_{0.2}Co_{0.4}Al_{0.2})O_{3-\delta}$	solid-state	4	0.14	1350/1000	45/15	40.0	N_2/N_2		194.0	12.93	27
$(La_{0.8}Sr_{0.2})(Mn_{0.2}Fe_{0.2}Co_{0.4}Al_{0.2})O_{3-\delta}$	solid-state	4	0.14	1350/1100	30/30	40.0	N_2/N_2		270.0	9.00	27
$(La_{0.8}Sr_{0.2})(Mn_{0.2}Fe_{0.2}Co_{0.4}Al_{0.2})O_{3-\delta}$	solid-state	4	0.14	1350/1100	30/60	40.0	N_2/N_2		351.0	5.85	27

https://doi.org/10.1021/acscatal.4c03357
ACS Catal. 2024, 14, 14974−15013

Table 10. continued

composition	synthesis method	cycles	$\Delta\delta$	temp. red./ox. (°C)	time red./ox. (min)	H_2O (% vol)	gas red./ox.	O_2 yield (μmol g^{-1})	H_2 yield (μmol g^{-1})	average H_2 production rate (μmol g^{-1} min^{-1})	ref
$(La_{0.8}Sr_{0.2})(Mn_{0.2}Fe_{0.2}Co_{0.4}Al_{0.2})O_{3-\delta}$	solid-state	12	0.14	1350/1100	30/30	40.0	N_2/N_2		386.9	12.90	27
$(La_{0.8}Sr_{0.2})(Mn_{0.2}Fe_{0.2}Co_{0.4}Al_{0.2})O_{3-\delta}$	solid-state	51	0.14	1350/1100	30/60	40.0	N_2/N_2		157.9	2.63	27
$(La_{1/6}Pr_{1/6}Nd_{1/6}Gd_{1/6}Sr_{1/6}Ba_{1/6})MnO_3$	solid-state	1	0.0822	1350/1100	5/20	40.0	N_2/N_2		91.9	4.60	152
$(La_{1/6}Pr_{1/6}Nd_{1/6}Gd_{1/6}Sr_{1/6}Ba_{1/6})MnO_3$	solid-state	2	0.0822	1350/1100	5/20	40.0	N_2/N_2		110.8	5.54	152
$(La_{1/6}Pr_{1/6}Nd_{1/6}Gd_{1/6}Sr_{1/6}Ba_{1/6})MnO_3$	solid-state	3	0.0822	1350/1100	5/20	40.0	N_2/N_2		126.4	6.32	152
$(La_{1/6}Pr_{1/6}Nd_{1/6}Gd_{1/6}Sr_{1/6}Ba_{1/6})MnO_3$	solid-state	4	0.0822	1350/1100	5/20	40.0	N_2/N_2		123.5	6.18	152
$(La_{1/6}Pr_{1/6}Nd_{1/6}Gd_{1/6}Sr_{1/6}Ba_{1/6})MnO_3$	solid-state	1	0.0822	1350/1100	30/30	40.0	N_2/N_2		214.9	7.16	152
$(La_{1/6}Pr_{1/6}Nd_{1/6}Gd_{1/6}Sr_{1/6}Ba_{1/6})MnO_3$	solid-state	2	0.0822	1350/1100	30/30	40.0	N_2/N_2		240.2	8.01	152
$(La_{1/6}Pr_{1/6}Nd_{1/6}Gd_{1/6}Sr_{1/6}Ba_{1/6})MnO_3$	solid-state	3	0.0822	1350/1100	30/30	40.0	N_2/N_2		252.8	8.43	152
$(La_{1/6}Pr_{1/6}Nd_{1/6}Gd_{1/6}Sr_{1/6}Ba_{1/6})MnO_3$	solid-state	4	0.0822	1350/1100	30/30	40.0	N_2/N_2		252.8	8.43	152
$(La_{1/6}Pr_{1/6}Nd_{1/6}Gd_{1/6}Sr_{1/6}Ba_{1/6})MnO_3$	solid-state	1	0.0822	1350/900	30/30	40.0	N_2/N_2		269.7	8.99	152
$(La_{1/6}Pr_{1/6}Nd_{1/6}Gd_{1/6}Sr_{1/6}Ba_{1/6})MnO_3$	solid-state	2	0.0822	1350/900	30/30	40.0	N_2/N_2		307.6	10.25	152
$(La_{1/6}Pr_{1/6}Nd_{1/6}Gd_{1/6}Sr_{1/6}Ba_{1/6})MnO_3$	solid-state	3	0.0822	1350/900	30/30	40.0	N_2/N_2		322.4	10.75	152
$(La_{1/6}Pr_{1/6}Nd_{1/6}Gd_{1/6}Sr_{1/6}Ba_{1/6})MnO_3$	solid-state	4	0.0822	1350/900	30/30	40.0	N_2/N_2		326.6	10.89	152

tionally complex ceramics offer a promising pathway to enhance the efficiency and stability of STCH materials. The development of new perovskite compositions and the exploration of their performance in large-scale systems will be crucial for realizing the full potential of perovskites in solar thermochemical water-splitting.

6. THEORETICAL CALCULATIONS AND MODELING STUDIES

Since $\Delta\delta$ directly impacts the H_2 production, it is important to evaluate the formation of oxygen vacancies in perovskite materials at both the reduction and oxidation conditions as a guidance. Density functional theory (DFT) calculations have been used to evaluate the oxygen vacancy formation energy. Combining DFT results and thermodynamics connects the DFT-computed vacancy formation energy to STCH performance. Thus, high-throughput DFT calculations can be used to achieve the design of computational materials. Based on the DFT generated data, it becomes possible to develop a machine learning approach to further expand the material search.

The first level of evaluation comes from the DFT computed neutral oxygen vacancy formation energy (ΔE_v^f). At 0 K,

$$\Delta E_v^f = E_{\text{defective}}^{\text{tot}} - E_{\text{pristine}}^{\text{tot}} + \frac{1}{2}E_{O_2}^{\text{tot}} \quad (18)$$

where $E_{\text{host}}^{\text{tot}}$, $E_{\text{defective}}^{\text{tot}}$, and $E_{O_2}^{\text{tot}}$ are the total energy of the pristine host structure, that of the O-deficient structure, and that of an oxygen molecule, respectively.[159] When treating strongly correlated electronic materials, the DFT+U[160] method is widely adopted to ameliorate the self-interaction inaccuracies that standard DFT has while modestly increasing the computational cost. Without the Hubbard U correction, generalized gradient approximations (GGA), such as PBE and PW91 functionals, can predict simple properties, such as lattice parameters, but can be wrong with electronic properties, magnetic properties, vacancy formation energy, and surface effects.[161] More advanced functionals, such as PBEsol (a modification of PBE) and the SCAN[162] meta-GGA functionals ideally should produce more accurate material properties. Table 12 collects the recent DFT computed oxygen vacancy formation energy (ΔE_v^f) along with the exchange-correlation functional. These DFT studies show that ΔE_v^f (T = 0 K) is determined by the elements and compositions on both A- and B-sites in ABO_3, serving as a useful tool for materials design. There are other mechanisms that contribute to the oxygen vacancy formation entropy, including the electronic entropy, which may arise due to the formation of charged oxygen vacancy defects. These emerging calculations will not be fully discussed in this Review. Instead, we will focus on charge-neutral oxygen vacancies. Since the predicted properties for transition metal oxides are sensitive to the DFT calculation details, as shown in Table 12, more caution is needed for high-throughput DFT calculations and DFT-trained machine learning approaches in complex perovskites. Here we summarize them into two sections.

6.1. Oxygen Vacancy Formation Energy in Simple ABO_3 Compositions. The effect of A elements and/or B elements on the oxygen vacancy formation energy was evaluated by comparing different simple ABO_3 perovskites using DFT calculations. Due to the simplicity of these structures, high-throughput calculations are possible.

Jia et al. calculated the E_v^f of $ABO_{3-\delta}$ (A = La, Sr, and B = Fe, Co).[163] They obtained that ΔE_v^f is in the order of $LaFeO_3$ > $LaCoO_3$ > $SrFeO_3$ > $SrCoO_3$. It should be noted that the 80-atom supercell was used for $LaBO_3$, while the 40-atom supercell was used for $SrFeO_3$.

Ghose et al. studied the effect of the B-site element in $BaMO_3$ (M = Ti−Cu).[164] ΔE_v^f decreases as this electronic

https://doi.org/10.1021/acscatal.4c03357
ACS Catal. 2024, 14, 14974−15013

Table 11. Comparative Analysis of Perovskite Oxides and Ceria: Pros and Cons, Development Status, and Future Potential

perovskite family	advantages	disadvantages	development status	potential for overcoming barriers
Mn-based perovskites	high redox activity; significant ionic conductivity; in some systems, Sr doping enhances performance and offers potential for optimization	over doping with Sr negatively impacts reoxidation yield, potential structural changes	extensive research in water-splitting and fuel cells	optimization of doping strategies; development of more stable structures
MnAl-based perovskites	enhanced reoxidation efficiency and an increased extent of reduction	high Sr doping can negatively affect redox activity	research on optimization of Sr, Mn, Al, and Ca; DFT calculations and experimental studies	optimization of doping levels; improvement of structural stability; exploration of new chemical compositions and structures
MnX-based perovskites	high H_2 yield with Ce, Cr doping; stability under high temperatures and reducing environments	formation of secondary phases	research on the effects of various dopants; development of high-purity synthesis methods	optimization of doping levels and chemical compositions
Fe- and FeX-based perovskites	lower reduction temperature required	sintering and structural changes; presence of secondary phases	research focused on fuel cells and thermochemical cycles; extensive research, particularly on $La_{1-x}Sr_xFeO_3$; studies include Co, Ni, Ir, and Ti dopants	development of antisintering materials; improved thermal stability
Co- and CoX-based perovskites	Co doping enhances oxygen vacancy formation and redox activity	structural changes and aggregation; phase changes at high temperatures	widely used in catalysis and fuel cells; research on various Co-based perovskites and doping strategies	improved stability through doping and protective layers
other perovskites	competitive H_2 production; tunable redox properties; potential high-entropy stability	irreversible structural changes; lower H_2 production with Cu dopant	emerging materials research, particularly high-entropy oxides	in-depth study of thermodynamic and kinetic properties; exploration of new compositional spaces
CeO_2	fast oxidation kinetics; thermal stability	low extent of stoichiometry	extensive doping research; proven performance in large-scale solar reactors	apply doping strategies to address volatilization at both low P_{O_2} and high temperatures

structure transitions from semiconducting character ($BaTiO_3$, $BaVO_3$) to ferromagnetic character ($BaCrO_3$, $BaMnO_3$, and $BaFeO_3$) and ultimately metallic character ($BaCoO_3$, $BaNiO_3$, and $BaCuO_3$). The decreasing trend indicates a progressive weakening of the M−O bond, which, in turn, enhances the reduction of M^{4+}. The trend was rationalized in terms of their electronic band structures and partial densities of states, which are related to the charge transfer.

Gautam et al. compared the ΔE_v^f of $CaMO_{3-0.125}$, $CeMO_{3-0.125}$, and $Ca_{0.5}Ce_{0.5}MO_{3-0.125}$, where M = Sc, Ti, V, Cr, Mn, Fe, Co, and Ni, using SCAN+U.[124] They correlated the E_v^f to the standard reduction potentials (versus the standard hydrogen electrode, SHE). It was found that the trends in standard reduction potentials are the dominant criteria indictating the monatomic decrease of ΔE_v^f in $CaMO_{3-0.125}$ and $CeMO_{3-0.125}$ as M varies from Ti to Co (the higher standard reduction potentials, the lower the E_v^f). In $Ca_{0.5}Ce_{0.5}MO_{3-0.125}$, however, structural and electronic factors play a larger role in determining ΔE_v^f.

Curnan et al. evaluated the effects of concentration, crystal structure, magnetism, and electronic structure on the ΔE_v^f of ABO_3 (A = La, Sr, Ba, K, Na and B = Sc, Ti, V, Cr, Mn, Fe, Co, Ni, Cu).[165] It was shown that the higher ΔE_v^f was observed in La-based ABO_3 when comparing A-site elements, and the cubic structure has a lower ΔE_v^f compared to the rhombohedral structure ($LaBO_3$) and to the orthorhombic structure ($SrBO_3$). They also showed that trends in ΔE_v^f are largely unaffected by the supercell size; however, the value of E_v^f varies by more than 1 eV between the 1 × 1 × 1 supercell and the 2 × 2 × 2 supercell (for example, $LaCuO_3$, $SrCrO_3$, $SrMnO_3$, and $SrFeO_3$), indicating vacancy−vacancy interaction. They have focused on characterizing the relative ordering in energetic trends.

Emery et al. investigated 5329 compounds in a high-throughput manner, as presented in Figure 15.[166] They first reported 383 thermodynamically stable compounds based on the stability of a compound with respect to all other phases present in the A−B−O phase diagram ($\Delta H_{stab}^{ABO_3}$ < 25 meV/atom). Then, the ΔE_v^f was calculated for the predicted 383 compounds and 139 compounds that fall in the target ΔE_v^f window (2.5 < ΔE_v^f/(O atom) < 5 eV). For the defect calculations, extremely small 9-atom ($A_2B_2O_5$) supercells were used to reduce the computational cost.

Deml et al. further related the DFT-computed ΔE_v^f values for 45 oxides to features such as the strength of the metal−oxygen bonds, the energy needed to transfer the electrons left behind by the neutral O vacancy, and the charge transfer between chemically bonded O and metal atoms with a linear relation[167] approach. This machine learning model can be used to predict ΔE_v^f values accurately (with an error of 0.39 eV in a subset of oxides in the NRELMatDB database) without the cost of DFT calculations.

Wexler et al. proposed a machine learning linear model based on SCAN+U that obtained ΔE_v^f values of ABO_3 perovskites, where A = Ca, Sr, Ba, La, Ce and B = Ti, V, Cr, Mn, Fe, Co, Ni, in six lattice systems.[168] They took crystal bond dissociation energies, crystal reduction potentials, band gaps, and energies above the convex hull as inputs and demonstrated that the model prevailed over the one presented by Deml et al. Its ability in material discovery was presented by predicting $BiFeO_3$ and $BiCoO_3$ as possible STCH candidates.

Baldassarri et al. discussed the importance of using DFT ground-state structures instead of a dynamically unstable

https://doi.org/10.1021/acscatal.4c03357
ACS Catal. 2024, 14, 14974−15013

Table 12. DFT-Calculated Neutral Oxygen Vacancy Formation Energies

composition							
A	B	supercell size	no. of Vo in a supercell	δ	DFT method	ΔE_v^f(eV)	ref
La	Mn	80	single	0.0625	DFT+U (GGA-PBE)	3.9	114
$Sr_{0.4}La_{0.6}$	Mn	80	single	0.0625	DFT+U (GGA-PBE)	2.6	114
$Sr_{0.2}La_{0.8}$	$Mn_{0.6}Al_{0.4}$	80	single	0.0625	DFT+U (GGA-PBE)	3.3[a]	114
$Sr_{0.4}La_{0.6}$	$Mn_{0.6}Al_{0.4}$	80	single	0.0625	DFT+U (GGA-PBE)	2.6	114
$Sr_{0.6}La_{0.4}$	$Mn_{0.6}Al_{0.4}$	80	single	0.0625	DFT+U (GGA-PBE)	1.4	114
$Sr_{0.4}La_{0.6}$	$Mn_{0.4}Al_{0.6}$	80	single	0.0625	DFT+U (GGA-PBE)	2.2	114
Sr	Fe	80	single	0.0625	DFT+U (GGA-PBE)	2.102	170
$Sr_{0.875}Ca_{0.125}$	Fe	80	single	0.0625	DFT+U (GGA-PBE)	2.018	170
$Sr_{0.75}Ca_{0.25}$	Fe	80	single	0.0625	DFT+U (GGA-PBE)	2.016	170
$Sr_{0.525}Ca_{0.375}$	Fe	80	single	0.0625	DFT+U (GGA-PBE)	1.98	170
$Sr_{0.5}Ca_{0.5}$	Fe	80	single	0.0625	DFT+U (GGA-PBE)	2.096	170
Sr	Fe	80	multiple	0.1875	DFT+U (GGA-PBE)	2.253	170
$Sr_{0.875}Ca_{0.125}$	Fe	80	multiple	0.1875	DFT+U (GGA-PBE)	2.084	170
$Sr_{0.75}Ca_{0.25}$	Fe	80	multiple	0.1875	DFT+U (GGA-PBE)	2.042	170
$Sr_{0.525}Ca_{0.375}$	Fe	80	multiple	0.1875	DFT+U (GGA-PBE)	1.951	170
$Sr_{0.5}Ca_{0.5}$	Fe	80	multiple	0.1875	DFT+U (GGA-PBE)	1.957	170
Sr	Fe	80	multiple	0.375	DFT+U (GGA-PBE)	2.587	170
$Sr_{0.875}Ca_{0.125}$	Fe	80	multiple	0.375	DFT+U (GGA-PBE)	2.58	170
$Sr_{075}Ca_{0.25}$	Fe	80	multiple	0.375	DFT+U (GGA-PBE)	2.476	170
$Sr_{0.525}Ca_{0.375}$	Fe	80	multiple	0.375	DFT+U (GGA-PBE)	2.484	170
$Sr_{0.5}Ca_{0.5}$	Fe	80	multiple	0.375	DFT+U (GGA-PBE)	2.532	170
Sr	Fe	80	multiple	0.5625	DFT+U (GGA-PBE)	2.862	170
$Sr_{0.875}Ca_{0.125}$	Fe	80	multiple	0.5625	DFT+U (GGA-PBE)	2.762	170
$Sr_{0.75}Ca_{0.25}$	Fe	80	multiple	0.5625	DFT+U (GGA-PBE)	2.749	170
$Sr_{0.525}Ca_{0.375}$	Fe	80	multiple	0.5625	DFT+U (GGA-PBE)	2.749	170
$Sr_{0.5}Ca_{0.5}$	Fe	80	multiple	0.5625	DFT+U (GGA-PBE)	2.755	170
Sr	$Co_{0.8}Fe_{0.2}$	40	single	0.125	GGA-PBE	1.58	171
$Ba_{0.5}Sr_{0.5}$	Co	40	single	0.125	GGA-PBE	1.03	171
$Ba_{0.5}Sr_{0.5}$	$Co_{0.75}Fe_{0.25}$	40	single	0.125	GGA-PBE	1.34	171
$Ba_{0.5}Sr_{0.5}$	$Co_{0.5}Fe_{0.5}$	40	single	0.125	GGA-PBE	1.63	171
$Ba_{0.5}Sr_{0.5}$	$Co_{0.25}Fe_{0.75}$	40	single	0.125	GGA-PBE	1.82	171
$Ba_{0.5}Sr_{0.5}$	Fe	40	single	0.125	GGA-PBE	2.07	171
La	Ga	80	single	0.0625	DFT+U (GGA-PBE)	5.3	119
La	$Ga_{0.75}Co_{0.25}$	80	single	0.0625	DFT+U (GGA-PBE)	3.0	119
La	$Ga_{0.5}Co_{0.5}$	80	single	0.0625	DFT+U (GGA-PBE)	2.9	119
La	$Ga_{0.25}Co_{0.75}$	80	single	0.0625	DFT+U (GGA-PBE)	2.2	119
La	Co	80	single	0.0625	DFT+U (GGA-PBE)	2.9	119
$La_{0.875}Sr_{0.125}$	$Ga_{0.5}Co_{0.5}$	80	single	0.0625	DFT+U (GGA-PBE)	1.5[a]	119
$La_{0.75}Sr_{0.25}$	$Ga_{0.5}Co_{0.5}$	80	single	0.0625	DFT+U (GGA-PBE)	0.7	119
$La_{0.5}Sr_{0.5}$	Fe	40	multiple	0.125	DFT+U (GGA-PW91)	0.3992	172
$La_{0.5}Sr_{0.5}$	$Fe_{0.5}Co_{0.5}$	40	multiple	0.125	DFT+U (GGA-PW91)	0.3255	172
$La_{0.5}Sr_{0.5}$	Co	40	multiple	0.125	DFT+U (GGA-PW91)	0.2483	172
$La_{0.5}Sr_{0.5}$	Fe	40	multiple	0.25	DFT+U (GGA-PW91)	0.8276	172
$La_{0.5}Sr_{0.5}$	$Fe_{0.5}Co_{0.5}$	40	multiple	0.25	DFT+U (GGA-PW91)	0.6687	172
$La_{0.5}Sr_{0.5}$	Co	40	multiple	0.25	DFT+U (GGA-PW91)	0.5553	172
$La_{0.5}Sr_{0.5}$	Fe	40	multiple	0.375	DFT+U (GGA-PW91)	1.2299	172
La0.5Sr0.5	$Fe_{0.5}Co_{0.5}$	40	multiple	0.375	DFT+U (GGA-PW91)	1.0375	172
La0.5Sr0.5	Co	40	multiple	0.375	DFT+U (GGA-PW91)	0.8712	172
Ca	Mn	20	single	0.25	DFT (GGA-PW91)	1.47	173
Ca	$Co_{0.25}Mn_{0.75}$	20	single	0.25	DFT (GGA-PW91)	0.60	173
Ca	$Co_{0.5}Mn_{0.5}$	21	single	0.25	DFT (GGA-PW91)	0.47	173
Ca	$Co_{0.75}Mn_{0.25}$	22	single	0.25	DFT (GGA-PW91)	0.38	173
Ca	Co	23	single	0.25	DFT (GGA-PW91)	0.36	173
La	Fe	80	single	0.0625	DFT+U (GGA-PBE)	4.98	163
La	Co	80	single	0.0625	DFT+U (GGA-PBE)	4.02	163
Sr	Fe	40	single	0.125	DFT+U (GGA-PBE)	2.34	163
Sr	Co	40	single	0.125	DFT+U (GGA-PBE)	1.30	163
Ba	Ti	40	single	0.125	PBEsol	5.18[a]	164
Ba	V	40	single	0.125	PBEsol	4.46[a]	164

https://doi.org/10.1021/acscatal.4c03357
ACS Catal. 2024, 14, 14974−15013

Table 12. continued

composition							
A	B	supercell size	no. of Vo in a supercell	δ	DFT method	ΔE_v^f(eV)	ref
Ba	Cr	40	single	0.125	PBEsol	3.42	164
Ba	Mn	40	single	0.125	PBEsol	1.35[a]	164
Ba	Fe	40	single	0.125	PBEsol	1.30[a]	164
Ba	Co	40	single	0.125	PBEsol	0.52[a]	164
Ba	Ni	40	single	0.125	PBEsol	−0.41[a]	164
Ba	Cu	40	single	0.125	PBEsol	−1.04[a]	164
Ca	Ti	40	single	0.125	SCAN+U	6.48	124
Ca	V	40	single	0.125	SCAN+U	4.18	124
Ca	Cr	40	single	0.125	SCAN+U	2.25	124
Ca	Mn	40	single	0.125	SCAN+U	2.25	124
Ca	Fe	40	single	0.125	SCAN+U	0.80[a]	124
Ca	Co	40	single	0.125	SCAN+U	−1.37	124
Ca	Ni	40	single	0.125	SCAN+U	1.20[a]	124
Ce	Sc	40	single	0.125	SCAN+U	6.70[a]	124
Ce	V	40	single	0.125	SCAN+U	6.30[a]	124
Ce	Cr	40	single	0.125	SCAN+U	5.22	124
Ce	Co	40	single	0.125	SCAN+U	3.68	124
Ce	Ni	40	single	0.125	SCAN+U	4.25	124
$Ca_{0.5}Ce_{0.5}$	Sc	40	single	0.125	SCAN+U	4.40[a]	124
$Ca_{0.5}Ce_{0.5}$	Ti	40	single	0.125	SCAN+U	6.30[a]	124
$Ca_{0.5}Ce_{0.5}$	V	40	single	0.125	SCAN+U	5.00[a]	124
$Ca_{0.5}Ce0_{.5}$	Cr	40	single	0.125	SCAN+U	4.80[a]	124
$Ca_{0.5}Ce_{0.5}$	Mn	40	single	0.125	SCAN+U	3.65[a]	124
$Ca_{0.5}Ce_{0.5}$	Fe	40	single	0.125	SCAN+U	3.77[a]	124
$Ca_{0.5}Ce_{0.5}$	Co	40	single	0.125	SCAN+U	−0.1[a]	124
$Ca_{0.5}Ce_{0.5}$	Ni	40	single	0.125	SCAN+U	0.2[a]	124

[a]Values obtained from plot.

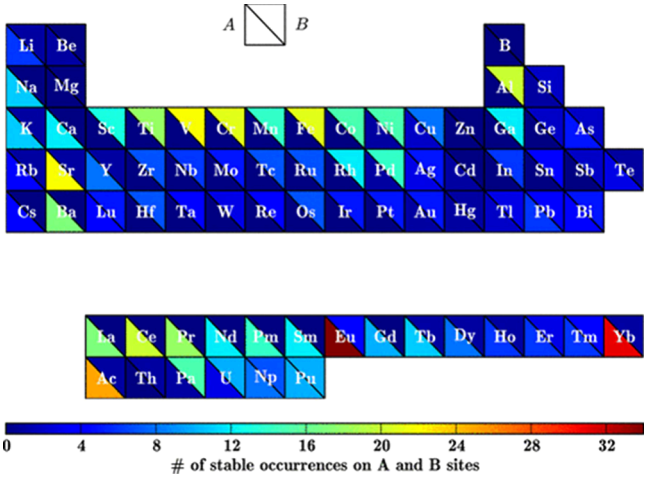

Figure 15. High-throughput density functional theory analysis of 5329 cubic and distorted perovskite ABO_3 compounds for screening thermodynamically suitable materials for two-step thermochemical water-splitting. Stability of ABO_3 perovskites was assessed by the frequency of A- and B-site cations: a periodic table highlights all elements considered for A and B sites. Elements are color-coded according to their frequency of stable occurrences on either the A- or B-site.[166] Reproduced from ref 166. Copyright 2016 American Chemical Society.

structure that was observed by experiment, since ΔE_v^f is very sensitive to the structure used in computation.[169] They applied this approach to revise and expand their high-throughput framework for STCH ABO_3 material screening and reduced the error from 0.86 to 0.54 eV. They predicted ΔE_v^f values for ∼2200 compositions and found ∼180 compounds within the STCH window (2−5 eV). Based on the appearance frequency in the lower end of the STCH window, Mn^{4+}, Mn^{3+}, and Co^{3+} were identified as the more promising redox-active B cations for STCH applications.

6.2. Effect of A- or B-Site Doping on Oxygen Vacancy Formation Energy. In practice, most perovskite oxides used for STCH contain either A-site mixing, B-site mixing, or both. Computing the oxygen vacancy formation energy with mixed A- and/or B-sites requires larger structures and mixed sites.

Deml et al. investigated the composition dependency of ΔE_v^f in $Sr_xLa_{1-x}Mn_yAl_{1-y}O_{3-0.0625}$ (x, y = 0.2, 0.4, 0.6, and 0.8), as shown in Figure 16.[114] The ΔE_v^f value decreases as the Sr content increases. When $x > y$, increases in Mn contents result in an increase of ΔE_v^f, while ΔE_v^f is approximately constant as the Mn contents increase for $y > x$. It was concluded that $Sr_{0.4}La_{0.6}Mn_{0.6}Al_{0.4}O_3$ has a E_v^f = 2.6 eV predicted by DFT calculation and is the optimal composition based on the design parameters including redox thermodynamics, kinetics, utilized redox capacity, and material stability.

Jia et al. studied the effect of Ca^{2+} doping in $Sr_{1-x}Ca_xFeO_{3-0.0625}$ (x = 0, 0.125, 0.25, 0.375, 0.5).[170] It was shown that the ΔE_v^f has its minimum value at x = 0.375 and the dominant mechanism behind this is a change of the Fe−O. For x = 0−0.375, the ΔE_v^f decreases due to the shortening of Fe−O bonds through Ca^{2+} doping, while for x = 0.375−0.5 it increases since the Fe−O bonds increase in length to a more stable length due to the FeO_6 octahedron distortion. They also calculated the ΔE_v^f for $Sr_{1-x}Ca_xFeO_{3-\delta}$, where δ = 0.1875, 0.375, and 0.5625, by removing 3, 6, and 9 O atoms from the 80-atom supercell randomly. The trend of ΔE_v^f decreasing first

https://doi.org/10.1021/acscatal.4c03357
ACS Catal. 2024, 14, 14974−15013

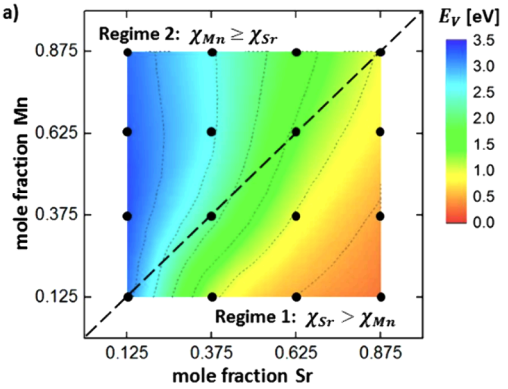

Figure 16. Relationship between composition and oxygen vacancy formation energies (ΔE_v^f) in $Sr_xLa_{1-x}Mn_yAl_{1-y}O_{3-0.0625}$ (x, y = 0.2, 0.4, 0.6, and 0.8).[114] Reproduced from ref 114. Copyright 2014 American Chemical Society.

and then increasing upon Ca^{2+} doping is unchanged for those cases; however, a vacancy−vacancy interaction has not been explored.

Merkle et al. analyzed the dependence of the ΔE_v^f on the Fe content in $Ba_{1-x}Sr_xCo_{1-y}Fe_yO_{3-0.125}$.[171] The ΔE_v^f linearly increases with increasing Fe content, which was rationalized based on the calculated electronic density of states, with unoccupied Fe states located higher in energy than Co states. Fe exhibits a peak about 1 eV higher than the Fermi level, whereas Co shows a considerable density of states close to the Fermi level so that Co^{4+} can easily is reduced to Co^{3+}.

Chen et al. demonstrated that doping of Sr or Co in A- or B-site, respectively, is useful to reduce the ΔE_v^f in $La_{1-x}Sr_xGa_{1-y}Co_yO_{3-0.0625}$ because the metal oxygen bonds (M−O) are weakened after doping.[119] They experimentally found that undoped $LaGaO_3$ is inactive for water-splitting and thus doping Co makes it redox active.

Maiti et al. showed a systematic trend of ΔE_v^f: the value of ΔE_v^f is smaller as the Sr content increases in the A-site and as the Fe content decreases in the B-site in $La_{1-x}Sr_xFe_{1-y}Co_yO_{3-\delta}$ (δ = 0.125, 0.25, 0.375).[172] They also found that oxygen removal from the La layer is more favorable than that from a Sr layer due to the d orbitals in La and the smaller ionic radius. The ΔE_v^f values with δ = 0.125, 0.25, and 0.375 were calculated by removing 1, 2, and 3 atoms of the 40-atom supercell. A vacancy−vacancy interaction has not been included even though the 40-atom supercell is small.

Jin et al. investigated the ΔE_v^f of Co-doped $CaCo_xMn_{1-x}O_{3-\delta}$ with different Co content levels (x = 0−1).[173] It was shown that even with a small amount of Co-doping (x = 0.25), the value of ΔE_v^f is reduced by almost half (1.47 to 0.60 eV). As the Co content increases further, ΔE_v^f decreases so that the oxygen release process is facilitated. However, it should be noted that the 2 × 2 × 1 supercell (20 atoms) is very small, vacancy−vacancy interaction is likely in such a small cell.

Witman et al. presented a graph neural network model applicable to arbitrary structures to predict vacancy formation enthalpies.[153] The model was trained with DFT data from all seven crystal structure systems, and the authors showed its ability to handle mixed ABO_3 systems by cross validating $(Ba_xA_{1-x})MnO_3$ (A = Ce, Nb, Pr) and $Sr_{1-x}Ce_xMnO_3$ with DFT. The prediction error of this more generalizable model is below 0.45 eV, which is comparable to the model from Demel or Wexler.[114,168] In most of these studies, a vacancy−vacancy interaction has been ignored. In detail, most of the studies investigated the formation of single neutral oxygen vacancy.[114,119,124,163−166,171,173] Several studies used a small cell size,[166,173] where the vacancy in the simulation cell and the vacancy in the image cells are likely to interact. Some have shown cell size (or concentration) dependent ΔE_v^f,[165] and others have explored multiple vacancies in a supercell, but these studies have not discussed the vacancy−vacancy interaction.[170,172] Das et al. showed oxygen vacancies start to interact around $\delta \sim 0.05$, and this interaction becomes stronger when $\delta > 0.1$ in $SrFeO_{3-\delta}$ and $La_{0.5}Sr_{0.5}FeO_{3-\delta}$.[159,174] It was shown that long-range charge transfer results in a large oxygen vacancy polaron size, which leads to a significant increase of E_v^f when $\delta > 0.1$. Mixed cations on A- and/or B-sites will significantly increase the search space. Vieten et al. calculated the perovskite to brownmillerite reaction enthalpy as an indication of the oxygen vacancy formation energy with at most two different elements mixed at both A- and B-sites.[175] To reach a better agreement with experiments, they had to consider vacancy interactions by introducing δ-dependent ΔH. A high-entropy perovskite was modeled recently for a different application; chemical looping involves oxygen vacancy reactions with CO_2. Wang et al. first applied high-throughput DFT calculations for the $Sr_xA_{1-x}Fe_yB_{1-y}O_{3-\delta}$ perovskite at various oxygen nonstoichiometries and different A (alkaline earth, alkali, or rare earth metals) and B (transition metals).[176] These DFT results were used to train a machine-learned random forest model to investigate the redox thermodynamics of 227 and 273 perovskites with 5 cation elements. Validation with experiments of the predicted compositions gave satisfactory results, but the authors admitted that their DFT model could not cover complicated spin couplings and electronic states in systems containing more than 5 cation elements. Detailed DFT calculations combined with Monte Carlo sampling have been used to investigate the oxygen vacancy formation in $LaSr\{CoFeMnCo\}O_{3-\delta}$. It was revealed that Co is the redox-active B-site element (agreeing with experiments), mainly due to the elongated bonds around Co in the high-entropy perovskite.[27]

6.3. Directly Predicting the $\Delta\delta$ for STCH Performance. To compare the DFT-computed oxygen vacancy formation energy at 0 K with the experimentally measurable properties under the oxygen gas at a given temperature (T) and partial pressure of oxygen (P_{O_2}), the oxygen vacancy formation free energy ($\Delta G_v^f(T, P_{O_2})$) can be employed and is calculated as

$$\Delta G_v^f(T, P_{O_2}) = \Delta E_v^f + \frac{1}{2}(\Delta \mu_{O_2}^0(T) + kT \ln P_{O_2}) \quad (19)$$

where $\Delta \mu_{O_2}^0(T)$ is the change in the chemical potential of oxygen from 0 K to T and k is the Boltzmann constant.

In $ABO_{3-\delta}$, δ is the oxygen nonstoichiometry and the site fraction of oxygen vacancies (X) is given by $X = \delta/3$. If the oxygen vacancy formation energy is independent of the oxygen nonstoichiometry (dilute scenario), the oxygen nonstoichiometry (δ) is typically described by[159,177]

$$\frac{\delta}{3-\delta} = \exp\left(-\frac{\Delta G_v^f(T, P_{O_2})}{RT}\right) \quad (20)$$

https://doi.org/10.1021/acscatal.4c03357
ACS Catal. 2024, 14, 14974−15013

With increasing δ, ΔG_v^f starts to increase with δ, due to vacancy−vacancy interaction, in a nondilute scenario, which is commonly observed in perovskites.[178,179] So, the right-hand side of eq 20 is modified as

$$\frac{\delta}{3-\delta} = \exp\left(-\frac{\Delta G_v^f(T, P_{O_2}, \delta)}{RT}\right) \quad (21)$$

Qian et al. further simplified ΔG_v^f as a linear function of δ and fitted it to experimental data to determine both the enthalpy and entropy of oxygen vacancy formation.[178,179] Das et al. also fitted DFT-computed ΔE_v^f as a linear function of δ and used eq 21 to predict the δ in $SrFeO_{3-\delta}$ and $La_{0.5}Sr_{0.5}FeO_{3-\delta}$.[159,174] They demonstrated that the increase of the vacancy formation energy with the vacancy concentration must be included to predict the δ measured in the experiments. In perovskites with mixed cations, especially in high-entropy or compositionally complex perovskite oxides, the oxygen vacancy formation energy is no longer a single value but rather has a distribution. Recently, Park et al. introduced distributed ΔE_v^f for eqs 18 −21 and predicted $\Delta\delta$ under the STCH reduction and oxidation conditions. By comparing dry TGA data, they illustrated that both the oxygen vacancy interaction and the vacancy formation energy distribution must be considered to predict the experimental trend.[135]

As described above, the chemical potential of oxygen (μ_O) varies with temperature and the oxygen partial pressure under dry conditions. Under wet conditions, the oxygen partial pressure is determined by the partial pressure of H_2O steam and the partial pressure of H_2 gas in a reactor.[91,180,181] Accordingly, μ_O changes with various testing conditions such as temperature, the gas composition in the reactor, and the oxygen nonstoichiometry. Thus, diverse experimental conditions can be unified through μ_O, which is beneficial for a fair comparison of the H_2 yields under different temperatures and steam concentrations.

7. CONCLUSIONS, CHALLENGES, AND PERSPECTIVES

Two-step solar-driven thermochemical hydrogen (STCH) is a promising renewable fuel technology that efficiently stores and converts solar light to hydrogen fuel. The oxygen storage capacity (OSC) plays a crucial role in assessing the suitability of metal oxides for thermochemical processes. Ideal metal oxides for STCH reactions exhibit a large redox extent, favorable thermodynamic properties (such as reduction of entropy and enthalpy), fast reaction kinetics, high resistance to sintering, and thermal stability. These characteristics contribute to efficient and reliable STCH processes.

Perovskite oxides, with their exceptional properties, have captivated researchers and sparked investigations of their potential for solar-to-hydrogen (H_2) conversion. The structural stability of perovskites enables them to accommodate significant oxygen vacancies during solar-to-fuel conversion. Their tunability also allows for the incorporation of various chemical elements, providing numerous possibilities for future investigations. This flexibility in tuning thermodynamic parameters makes perovskite materials ideal for designing favorable systems for STCH applications. Moreover, perovskites have the advantage of requiring lower reaction temperatures for reduction and offering a larger possible change of nonstoichiometry compared to ceria. Additionally, perovskites not only are promising for water-splitting but also show potential for CO_2 thermochemical reduction. Their ability to undergo redox reactions at high temperatures makes them suitable for both applications. The same properties that make perovskites effective for H_2O activation, such as the ability to accommodate multiple oxidation states and the presence of oxygen vacancies, are also beneficial for CO_2 reduction.

However, it should be noted, that unlike ceria, perovskite materials are still primarily at the laboratory scale and have not been demonstrated in upscaled reactor systems. The primary challenge faced by perovskites is the low efficiency of the solar-to-fuel conversion. Therefore, the next research direction is to search for novel perovskites with a higher efficiency that can yield greater hydrogen production in water-splitting reactions. Furthermore, another limitation associated with perovskite utilization is the incomplete reoxidation yield, resulting from low kinetics and insufficient thermodynamic driving forces. Additionally, high-entropy oxides, which consist of multiple principal elements, exhibit high configurational entropy. These materials demonstrate remarkable properties, such as stabilizing their structure at high temperatures, tunable water-splitting properties, and potential utilization for hydrogen production.

This study has compiled information about all perovskites used in STCH and has summarized various methods employed to investigate reaction kinetics and thermodynamics concerning nonstoichiometric perovskites, providing valuable insights into the diverse available techniques, along with their pros, cons, and related performance data. These characterizations are beneficial for identifying suitable perovskites with favorable thermodynamics and rapid reaction kinetics. Additionally, the crystallographic stability of perovskites over thermochemical cycling is also an important factor that affects the performance of solar thermochemical water-splitting. It is important to note that the B-site in perovskite materials is likely a key active site for H_2O activation; however, this hypothesis requires further validation, offering a promising avenue for future research.

Overall, the future prospects of perovskites in solar thermochemical water-splitting show considerable potential. However, the search for perovskites with high solar-to-fuel efficiency, favorable thermodynamics, fast kinetic properties, and crystallographic stability.

Recent advancements in high-entropy and compositionally complex ceramics open additional opportunities to tune the thermodynamic and kinetic properties of STCH materials via their vast, unexplored compositional space. These have been demonstrated in a few recent studies of HEPOs and CCPOs in the perovskite structure (without phase transformation during the STCH cycling),[27,158] as well as an equimolar polycation $(Fe_{0.25}Mg_{0.25}Co_{0.25}Ni_{0.25})O_x$ in the rocksalt/spinel structure (with phase transformation during STCH cycling).[182] In addition to the vast compositional spaces, compositionally complex ceramics (CCCs) also offer new mechanisms, e.g., using the distribution of oxygen vacancy formation enthalpies to tune STCH performance.[27,135] The benefits and new opportunities brought about by CCCs may also be extended to other oxides. For example, we can envision the tuning of oxygen vacancies and thereby STCH performance in ceria-based (or ceria-containing or even ceria-free) compositionally complex fluorite-based oxides (CCFBOs) that have been fabricated with a variety of compositions in the fluorite or fluorite-derived structure with long- and short-range order but not yet optimized for STCH performance.[151,183−187]

https://doi.org/10.1021/acscatal.4c03357
ACS Catal. 2024, 14, 14974−15013

AUTHOR INFORMATION

Corresponding Authors

Wei Li − *Department of Mechanical, Materials and Aerospace Engineering, Benjamin M. Statler College of Engineering and Mineral Resources, West Virginia University, Morgantown, West Virginia 26506, United States;* orcid.org/0000-0003-2802-7443; Email: liweicsiro@gmail.com

Yue Qi − *School of Engineering, Brown University, Providence, Rhode Island 02912, United States;* orcid.org/0000-0001-5331-1193; Email: YueQi@brown.edu

Jian Luo − *Program in Materials Science and Engineering, University of California San Diego, La Jolla, California 92093, United States; Department of NanoEngineering, University of California San Diego, La Jolla, California 92093, United States;* orcid.org/0000-0002-5424-0216; Email: jluo@alum.mit.edu

Xingbo Liu − *Department of Mechanical, Materials and Aerospace Engineering, Benjamin M. Statler College of Engineering and Mineral Resources, West Virginia University, Morgantown, West Virginia 26506, United States;* orcid.org/0000-0001-8720-7175; Email: xingbo.liu@mail.wvu.edu

Authors

Cijie Liu − *Department of Mechanical, Materials and Aerospace Engineering, Benjamin M. Statler College of Engineering and Mineral Resources, West Virginia University, Morgantown, West Virginia 26506, United States*

Jiyun Park − *School of Engineering, Brown University, Providence, Rhode Island 02912, United States*

Héctor A. De Santiago − *Department of Mechanical, Materials and Aerospace Engineering, Benjamin M. Statler College of Engineering and Mineral Resources, West Virginia University, Morgantown, West Virginia 26506, United States*

Boyuan Xu − *Department of Physics, Brown University, Providence, Rhode Island 02912, United States;* orcid.org/0000-0002-7611-1706

Dawei Zhang − *Program in Materials Science and Engineering, University of California San Diego, La Jolla, California 92093, United States*

Lingfeng Zhou − *Department of Chemical and Biomedical Engineering, Benjamin M. Statler College of Engineering and Mineral Resources, West Virginia University, Morgantown, West Virginia 26506, United States*

Complete contact information is available at: https://pubs.acs.org/10.1021/acscatal.4c03357

Notes

The authors declare no competing financial interest.

ACKNOWLEDGMENTS

This work was initially and primarily supported by the U.S. Department of Energy (DOE), Office of Energy Efficiency and Renewable Energy (EERE), under Agreement DE-EE0008839, managed by the Hydrogen and Fuel Cell Technologies Office in the Fiscal Year 2019 H_2@SCALE program. The UCSD team also acknowledges partial support from the National Science Foundation (Grant DMR-2026193) after the completion of the DOE project.

REFERENCES

(1) Kannan, N.; Vakeesan, D. Solar energy for future world: - A review. *Renew Sust Energ Rev.* **2016**, *62*, 1092−1105.

(2) Panwar, N. L.; Kaushik, S. C.; Kothari, S. Role of renewable energy sources in environmental protection: A review. *Renew Sust Energ Rev.* **2011**, *15* (3), 1513−1524.

(3) Nozik, A. J. Photoelectrochemistry-applications to solar-energy conversion. *Annu. Rev. Phys. Chem.* **1978**, *29*, 189−222.

(4) Schlamadinger, B.; Apps, M.; Bohlin, F.; Gustavsson, L.; Jungmeier, G.; Marland, G.; Pingoud, K.; Savolainen, I. Towards a standard methodology for greenhouse gas balances of bioenergy systems in comparison with fossil energy systems. *Biomass Bioenergy* **1997**, *13* (6), 359−375.

(5) Bayon, A.; de la Calle, A.; Ghose, K. K.; Page, A.; McNaughton, R. Experimental, computational and thermodynamic studies in perovskites metal oxides for thermochemical fuel production: A review. *Int. J. Hydrogen Energ* **2020**, *45* (23), 12653−12679.

(6) Mekhilef, S.; Saidur, R.; Safari, A. A review on solar energy use in industries. *Renew Sust Energ Rev.* **2011**, *15* (4), 1777−1790.

(7) Gong, J. L.; Li, C.; Wasielewski, M. R. Advances in solar energy conversion. *Chem. Soc. Rev.* **2019**, *48* (7), 1862−1864.

(8) Lewis, N. S. Introduction: Solar Energy Conversion. *Chem. Rev.* **2015**, *115* (23), 12631−12632.

(9) Kubicek, M.; Bork, A. H.; Rupp, J. L. M. Perovskite oxides - a review on a versatile material class for solar-to-fuel conversion processes. *J. Mater. Chem. A* **2017**, *5* (24), 11983−12000.

(10) Concepcion, J. J.; House, R. L.; Papanikolas, J. M.; Meyer, T. J. Chemical approaches to artificial photosynthesis. *Proc. Natl. Acad. Sci.* **2012**, *109* (39), 15560−15564.

(11) Blankenship, R. E.; Tiede, D. M.; Barber, J.; Brudvig, G. W.; Fleming, G.; Ghirardi, M.; Gunner, M. R.; Junge, W.; Kramer, D. M.; Melis, A.; Moore, T. A.; Moser, C. C.; Nocera, D. G.; Nozik, A. J.; Ort, D. R.; Parson, W. W.; Prince, R. C.; Sayre, R. T. Comparing Photosynthetic and Photovoltaic Efficiencies and Recognizing the Potential for Improvement. *Science* **2011**, *332* (6031), 805−809.

(12) Chueh, W. C.; Falter, C.; Abbott, M.; Scipio, D.; Furler, P.; Haile, S. M.; Steinfeld, A. High-Flux Solar-Driven Thermochemical Dissociation of CO2 and H2O Using Nonstoichiometric Ceria. *Science* **2010**, *330* (6012), 1797−1801.

(13) Dry, M. E. The Fischer−Tropsch process: 1950−2000. *Catal. Today* **2002**, *71* (3−4), 227−241.

(14) Zhang, Q. H.; Deng, W. P.; Wang, Y. Recent advances in understanding the key catalyst factors for Fischer−Tropsch synthesis. *J. Energy Chem.* **2013**, *22* (1), 27−38.

(15) Romero, M.; Steinfeld, A. Concentrating solar thermal power and thermochemical fuels. *Energy Environ. Sci.* **2012**, *5* (11), 9234−9245.

(16) Kodama, T.; Gokon, N. Thermochernical cycles for high-temperature solar hydrogen production. *Chem. Rev.* **2007**, *107* (10), 4048−4077.

(17) Balta, M. T.; Dincer, I.; Hepbasli, A. Comparative assessment of various chlorine family thermochemical cycles for hydrogen production. *Int. J. Hydrogen Energ* **2016**, *41* (19), 7802−7813.

(18) Sturzenegger, M.; Nüesch, P. Efficiency analysis for a manganese-oxide-based thermochemical cycle. *Energy* **1999**, *24* (11), 959−970.

(19) Bayon, A.; de la Peña O'Shea, V. A.; Serrano, D. P.; Coronado, J. M. Influence of structural and morphological characteristics on the hydrogen production and sodium recovery in the NaOH-MnO thermochemical cycle. *Int. J. Hydrogen Energy* **2013**, *38* (30), 13143−13152.

(20) Steinfeld, A.; Frei, A.; Kuhn, P.; Wuillemin, D. Solar Thermal Production of Zinc and Syngas via Combined ZnO-Reduction and CH4-Reforming process. *Int. J. Hydrogen Energ* **1995**, *20* (10), 793−804.

(21) Abanades, S.; Charvin, P.; Lemont, F.; Flamant, G. Novel two-step SnO2/Sno water-splitting cycle for solar thermochemical production of hydrogen. *Int. J. Hydrogen Energ* **2008**, *33* (21), 6021−6030.

(22) Charvin, P.; Abanades, S.; Flamant, G.; Lemort, F. Two-step water splitting thermochemical cycle based on iron oxide redox pair for solar hydrogen production. *Energy* **2007**, *32* (7), 1124−1133.
(23) Chueh, W. C.; Haile, S. M. Ceria as a Thermochemical Reaction Medium for Selectively Generating Syngas or Methane from H2O and CO2. *ChemSusChem* **2009**, *2* (8), 735−739.
(24) Chueh, W. C.; Haile, S. M. A thermochemical study of ceria: exploiting an old material for new modes of energy conversion and CO2 mitigation. *Philos. Trans. R. Soc. A-Math. Phys. Eng. Sci.* **2010**, *368* (1923), 3269−3294.
(25) Takacs, M.; Hoes, M.; Caduff, M.; Cooper, T.; Scheffe, J. R.; Steinfeld, A. Oxygen nonstoichiometry, defect equilibria, and thermodynamic characterization of LaMnO3 perovskites with Ca/Sr A-site and Al B-site doping. *Acta Mater.* **2016**, *103*, 700−710.
(26) Barcellos, D. R.; Sanders, M. D.; Tong, J. H.; McDaniel, A. H.; O'Hayre, R. P. BaCe0.25Mn0.75O3-delta-a promising perovskite-type oxide for solar thermochemical hydrogen production. *Energy Environ. Sci.* **2018**, *11* (11), 3256−3265.
(27) Zhang, D. W.; De Santiago, H. A.; Xu, B. Y.; Liu, C. J.; Trindell, J. A.; Li, W.; Park, J.; Rodriguez, M. A.; Coker, E. N.; Sugar, J. D.; McDaniel, A. H.; Lany, S.; Ma, L.; Wang, Y.; Collins, G.; Tian, H. C.; Li, W. Y.; Qi, Y.; Liu, X. B.; Luo, J. Compositionally Complex Perovskite Oxides for Solar Thermochemical Water Splitting. *Chem. Mater.* **2023**, *35* (5), 1901−1915.
(28) Ma, Z. W.; Martinek, J. Analysis of Solar Receiver Performance for Chemical-Looping Integration With a Concentrating Solar Thermal System. *J. Sol Energy Eng.* **2019**, *141* (2), No. 021003.
(29) Carrillo, R. J.; Scheffe, J. R. Advances and trends in redox materials for solar thermochemical fuel production. *Sol Energy* **2017**, *156*, 3−20.
(30) Oudejans, D.; Offidani, M.; Constantinou, A.; Albonetti, S.; Dimitratos, N.; Bansode, A. A Comprehensive Review on Two-Step Thermochemical Water Splitting for Hydrogen Production in a Redox Cycle. *Energies* **2022**, *15* (9), 3044.
(31) Safari, F.; Dincer, I. A review and comparative evaluation of thermochemical water splitting cycles for hydrogen production. *Energ Convers Manag* **2020**, *205*, 112182.
(32) Muhich, C. L.; Ehrhart, B. D.; Al-Shankiti, I.; Ward, B. J.; Musgrave, C. B.; Weimer, A. W. A review and perspective of efficient hydrogen generation via solar thermal water splitting. *Wiley Interdiscip. Rev. Energy Environ.* **2016**, *5* (3), 261−287.
(33) Xiao, L.; Wu, S. Y.; Li, Y. R. Advances in solar hydrogen production via two-step water-splitting thermochemical cycles based on metal redox reactions. *Renew Energ* **2012**, *41*, 1−12.
(34) Steinfeld, A. Solar thermochemical production of hydrogen - a review. *Sol Energy* **2005**, *78* (5), 603−615.
(35) Romero, M.; Steinfeld, A. Concentrating solar thermal power and thermochemical fuels. *Energy Environ. Sci.* **2012**, *5* (11), 9234−9245.
(36) Steinfeld, A.; Weimer, A. W. Thermochemical Production of Fuels with Concentrated Solar Energy. *Opt Express* **2010**, *18* (9), A100−A111.
(37) Scheffe, J. R.; Steinfeld, A. Oxygen exchange materials for solar thermochemical splitting of H2O and CO2: a review. *Mater. Today* **2014**, *17* (7), 341−348.
(38) Haeussler, A.; Abanades, S.; Jouannaux, J.; Julbe, A. Non-Stoichiometric Redox Active Perovskite Materials for Solar Thermochemical Fuel Production: A Review. *Catalysts* **2018**, *8* (12), 611.
(39) Abanades, S. Metal Oxides Applied to Thermochemical Water-Splitting for Hydrogen Production Using Concentrated Solar Energy. *ChemEngineering* **2019**, *3* (3), 63.
(40) Cheng, W. H.; de la Calle, A.; Atwater, H. A.; Stechel, E. B.; Xiang, C. X. Hydrogen from Sunlight and Water: A Side-by-Side Comparison between Photoelectrochemical and Solar Thermochemical Water-Splitting. *Acs Energy Letters* **2021**, *6* (9), 3096−3113.
(41) Grabowska, E. Selected perovskite oxides: Characterization, preparation and photocatalytic properties-A review. *Appl. Catal. B-environ* **2016**, *186*, 97−126.
(42) Tanaka, H.; Misono, M. Advances in designing perovskite catalysts. *Curr. Opin Solid St M* **2001**, *5* (5), 381−387.
(43) Pena, M. A.; Fierro, J. L. G. Chemical structures and performance of perovskite oxides. *Chem. Rev.* **2001**, *101* (7), 1981−2017.
(44) Santomauro, F. G.; Grilj, J.; Mewes, L.; Nedelcu, G.; Yakunin, S.; Rossi, T.; Capano, G.; Al Haddad, A.; Budarz, J.; Kinschel, D.; Ferreira, D. S.; Rossi, G.; Tovar, M. G.; Grolimund, D.; Samson, V.; Nachtegaal, M.; Smolentsev, G.; Kovalenko, M. V.; Chergui, M. Localized holes and delocalized electrons in photoexcited inorganic perovskites: Watching each atomic actor by picosecond X-ray absorption spectroscopy. *Struct. Dyn.* **2017**, *4* (4), No. 044002.
(45) De Santiago Hernandez, H. A., Thermochemical Water-Splitting using Novel High-Entropy Perovskite Oxides. Master's Thesis, West Virginia University, Morgantown, WV, 2022. DOI: 10.33915/etd.11222
(46) Ishihara, T. Inorganic Perovskite Oxides. In *Springer Handbook of Electronic and Photonic Materials*; Kasap, S., Capper, P., Eds.; Springer, 2017; p 1405−1420.
(47) Irvine, J.; Rupp, J. L. M.; Liu, G.; Xu, X. X.; Haile, S.; Qian, X.; Snyder, A.; Freer, R.; Ekren, D.; Skinner, S.; Celikbilek, O.; Chen, S. G.; Tao, S. W.; Shin, T. H.; O'Hayre, R.; Huang, J. K.; Duan, C. C.; Papac, M.; Li, S. B.; Celorrio, V.; Russell, A.; Hayden, B.; Nolan, H.; Huang, X. B.; Wang, G.; Metcalfe, I.; Neagu, D.; Martin, S. G. Roadmap on inorganic perovskites for energy applications. *J. Phys-Energy* **2021**, *3* (3), No. 031502.
(48) Amiri, A.; Shahbazian-Yassar, R. Recent progress of high-entropy materials for energy storage and conversion. *J. Mater. Chem. A* **2021**, *9* (2), 782−823.
(49) Li, Z. Q.; Guan, B.; Xia, F.; Nie, J. Y.; Li, W. Y.; Ma, L.; Li, W.; Zhou, L. F.; Wang, Y.; Tian, H. C.; Luo, J.; Chen, Y.; Frost, M.; An, K.; Liu, X. B. High-Entropy Perovskite as a High-Performing Chromium-Tolerant Cathode for Solid Oxide Fuel Cells. *Acs Appl. Mater. Interfaces* **2022**, *14* (21), 24363−24373.
(50) Yang, X.; Guo, R. K.; Cai, R.; Ouyang, Y. J.; Yang, P. P.; Xiao, J. F. Engineering high-entropy materials for electrocatalytic water splitting. *Int. J. Hydrogen Energ* **2022**, *47* (28), 13561−13578.
(51) Zhang, D. W.; Park, J.; Xu, B. Y.; Liu, C. J.; Li, W.; Liu, X. B.; Qi, Y.; Luo, J. Unusual aliovalent doping effects on oxygen non-stoichiometry in medium-entropy compositionally complex perovskite oxides. *Dalton Trans* **2023**, *52* (4), 1082−1088.
(52) Beskow, G.; Goldschmidt, V. M. Geochemische Verteilungsgesetze der Elemente. *Geologiska Föreningen i Stockholm Förhandlingar* **1924**, *46* (6−7), 738−743.
(53) Goldschmidt, V. V. M. Die Gesetze der Krystallochemie. *Die Naturwissenschaften* **1926**, *14* (21), 477−485.
(54) Li, Z.; Yang, M. J.; Park, J. S.; Wei, S. H.; Berry, J. J.; Zhu, K. Stabilizing Perovskite Structures by Tuning Tolerance Factor: Formation of Formamidinium and Cesium Lead Iodide Solid-State Alloys. *Chem. Mater.* **2016**, *28* (1), 284−292.
(55) Goldschmidt, V. M. The laws of crystal chemistry. *Naturwissenschaften* **1926**, *14*, 477−485.
(56) Jiang, S. C.; Hu, T.; Gild, J.; Zhou, N. X.; Nie, J. Y.; Qin, M. D.; Harrington, T.; Vecchio, K.; Luo, J. A new class of high-entropy perovskite oxides. *Scripta Mater.* **2018**, *142*, 116−120.
(57) Goodenough, J. B. Electronic and ionic transport properties and other physical aspects of perovskites. *Rep. Prog. Phys.* **2004**, *67* (11), 1915−1993.
(58) Kubicek, M.; Bork, A. H.; Rupp, J. L. M. Perovskite oxides - a review on a versatile material class for solar-to-fuel conversion processes. *J. MATER CHEM A* **2017**, *5* (24), 11983−12000.
(59) Maiti, T.; Saxena, M.; Roy, P. Double perovskite (Sr2B′B″O6) oxides for high-temperature thermoelectric power generation—A review. *J. Mater. Res.* **2019**, *34* (1), 107−125.
(60) Banerjee, R.; Chatterjee, S.; Ranjan, M.; Bhattacharya, T.; Mukherjee, S.; Jana, S. S.; Dwivedi, A.; Maiti, T. High-Entropy Perovskites: An Emergent Class of Oxide Thermoelectrics with Ultralow Thermal Conductivity. *ACS Sustainable Chem. Eng.* **2020**, *8* (46), 17022−17032.

(61) Vieten, J.; Bulfin, B.; Huck, P.; Horton, M.; Guban, D.; Zhu, L.; Lu, Y.; Persson, K. A.; Roeb, M.; Sattler, C. Materials design of perovskite solid solutions for thermochemical applications. *Energy Environ. Sci.* **2019**, *12* (4), 1369−1384.
(62) Jiang, S.; Hu, T.; Gild, J.; Zhou, N.; Nie, J.; Qin, M.; Harrington, T.; Vecchio, K.; Luo, J. A new class of high-entropy perovskite oxides. *Scripta Materialia* **2018**, *142*, 116−120.
(63) Bartel, C. J.; Sutton, C.; Goldsmith, B. R.; Ouyang, R. H.; Musgrave, C. B.; Ghiringhelli, L. M.; Scheffler, M. New tolerance factor to predict the stability of perovskite oxides and halides. *Sci. Adv.* **2019**, *5* (2), eaav0693.
(64) Haile, S. M. Fuel cell materials and components. *Acta Mater.* **2003**, *51* (19), 5981−6000.
(65) Richter, J.; Holtappels, P.; Graule, T.; Nakamura, T.; Gauckler, L. J. Materials design for perovskite SOFC cathodes. *Monatsh. Chem.* **2009**, *140* (9), 985−999.
(66) Qian, X.; He, J. G.; Mastronardo, E.; Baldassarri, B.; Yuan, W. Z.; Wolverton, C.; Haile, S. M. Outstanding Properties and Performance of CaTi0.5Mn0.5O3-delta for Solar-Driven Thermochemical Hydrogen Production. *Matter* **2021**, *4* (2), 688−708.
(67) Mastronardo, E.; Qian, X.; Coronado, J. M.; Haile, S. M. The favourable thermodynamic properties of Fe-doped CaMnO3 for thermochemical heat storage. *Journal of Materials Chemistry A* **2020**, *8* (17), 8503−8517.
(68) Hao, Y.; Yang, C. K.; Haile, S. M. Ceria-Zirconia Solid Solutions (Ce1-xZrxO2-delta, $x \leq 0.2$) for Solar Thermochemical Water Splitting: A Thermodynamic Study. *Chem. Mater.* **2014**, *26* (20), 6073−6082.
(69) Leonidova, E. I.; Leonidov, I. A.; Patrakeev, M. V.; Kozhevnikov, V. L. Oxygen non-stoichiometry, high-temperature properties, and phase diagram of CaMnO3-*δ*. *J. Solid State Electrochem* **2011**, *15* (5), 1071−1075.
(70) Pein, M.; Agrafiotis, C.; Vieten, J.; Giasafaki, D.; Brendelberger, S.; Roeb, M.; Sattler, C. Redox thermochemistry of Ca-Mn-based perovskites for oxygen atmosphere control in solar-thermochemical processes. *Sol Energy* **2020**, *198*, 612−622.
(71) Qian, X.; Haile, S. M.; Davenport, T. C.; Mastronardo, E. Experimental protocols for the assessment of redox thermodynamics of nonstoichiometric oxides: A case study of YMnO3-delta. *J. Am. Ceram. Soc.* **2022**, *105* (6), 4375−4386.
(72) Lenarduzzi, G.; Cooper, T. A. The role of entropy in the success of nonstoichiometric oxides for two-step thermochemical water and CO2 splitting. *Appl. Phys. Lett.* **2021**, *119* (26), No. 263902.
(73) Meredig, B.; Wolverton, C. First-principles thermodynamic framework for the evaluation of thermochemical H2O- or CO2-splitting materials. *Phys. Rev. B* **2009**, *80* (24), 245119.
(74) Khawam, A.; Flanagan, D. R. Solid-state kinetic models: Basics and mathematical fundamentals. *J. Phys. Chem. B* **2006**, *110* (35), 17315−17328.
(75) Vyazovkin, S.; Burnham, A. K.; Criado, J. M.; Perez-Maqueda, L. A.; Popescu, C.; Sbirrazzuoli, N. ICTAC Kinetics Committee recommendations for performing kinetic computations on thermal analysis data. *Thermochim. Acta* **2011**, *520* (1−2), 1−19.
(76) Scheffe, J. R.; McDaniel, A. H.; Allendorf, M. D.; Weimer, A. W. Kinetics and mechanism of solar-thermochemical H-2 production by oxidation of a cobalt ferrite-zirconia composite. *Energy Environ. Sci.* **2013**, *6* (3), 963−973.
(77) McDaniel, A. H.; Ambrosini, A.; Coker, E. N.; Miller, J. E.; Chueh, W. C.; O'Hayre, R.; Tong, J. Nonstoichiometric perovskite oxides for solar thermochemical H2 and CO production. *energy Procedia* **2014**, *49*, 2009−2018, DOI: 10.1016/j.egypro.2014.03.213.
(78) Haeussler, A.; Abanades, S.; Jouannaux, J.; Julbe, A. Non-Stoichiometric Redox Active Perovskite Materials for Solar Thermochemical Fuel Production: A Review. *Catalysts* **2018**, *8* (12), 611.
(79) Arifin, D.; Weimer, A. W. Kinetics and mechanism of solar-thermochemical H-2 and CO production by oxidation of reduced CeO2. *Sol Energy* **2018**, *160*, 178−185.
(80) Kim, Y.; Jeong, S. J.; Koo, B.; Lee, S.; Kwak, N. W.; Jung, W. Study of the surface reaction kinetics of (La,Sr)MnO3- oxygen carriers for solar thermochemical fuel production. *Journal of Materials Chemistry A* **2018**, *6* (27), 13082−13089.
(81) Gopal, C. B.; Haile, S. M. An electrical conductivity relaxation study of oxygen transport in samarium doped ceria. *Journal of Materials Chemistry A* **2014**, *2* (7), 2405−2417.
(82) Villafan-Vidales, H. I.; Arancibia-Bulnes, C. A.; Riveros-Rosas, D.; Romero-Paredes, H.; Estrada, C. A. An overview of the solar thermochemical processes for hydrogen and syngas production: Reactors, and facilities. *Renew Sust Energ Rev.* **2017**, *75*, 894−908.
(83) Steinfeld, A. Solar thermochemical production of hydrogen−−a review. *Sol. Energy* **2005**, *78* (5), 603−615.
(84) Kodama, T.; Gokon, N. Thermochemical cycles for high-temperature solar hydrogen production. *Chem. Rev.* **2007**, *107* (10), 4048−4077.
(85) Bilgen, E.; Ducarroir, M.; Foex, M.; Sibieude, F.; Trombe, F. Use of solar energy for direct and two-step water decomposition cycles. *Int. J. Hydrogen Energy* **1977**, *2* (3), 251−257.
(86) Li, S.; Wheeler, V. M.; Kumar, A.; Venkataraman, M. B.; Muhich, C. L.; Hao, Y.; Lipinski, W. Thermodynamic Guiding Principles for Designing Nonstoichiometric Redox Materials for Solar Thermochemical Fuel Production: Ceria, Perovskites, and Beyond. *Energy Technol.* **2022**, *10* (1), No. 2000925.
(87) Ezbiri, M.; Takacs, M.; Theiler, D.; Michalsky, R.; Steinfeld, A. Tunable thermodynamic activity of LaxSr1-xMnyAl1-yO3-delta ($0 \leq x \leq 1$, $0 \leq y \leq 1$) perovskites for solar thermochemical fuel synthesis. *Journal of Materials Chemistry A* **2017**, *5* (8), 4172−4182.
(88) Lou, J. H.; Tian, Z. Y.; Wu, Y. Y.; Li, X.; Qian, X.; Haile, S. M.; Hao, Y. Thermodynamic assessment of nonstoichiometric oxides for solar thermochemical fuel production. *Sol Energy* **2022**, *241*, 504−514.
(89) Yang, C.-K. *An Exploration of Perovskite Materials for Thermochemical Water Splitting*. Ph.D. Dissertation, California Institute of Technology, Pasadena, CA, 2015. DOI: 10.7907/Z91834GB
(90) Gokon, N.; Hara, K.; Sugiyama, Y.; Bellan, S.; Kodama, T.; Hyun-seok, C. Thermochemical two-step water splitting cycle using perovskite oxides based on LaSrMnO3 redox system for solar H-2 production. *Thermochim. Acta* **2019**, *680*, No. 178374.
(91) Yang, C. K.; Yamazaki, Y.; Aydin, A.; Haile, S. M. Thermodynamic and kinetic assessments of strontium-doped lanthanum Manganite perovskites for two-step thermochemical water splitting. *Journal of Materials Chemistry A* **2014**, *2* (33), 13612−13623.
(92) Agrafiotis, C.; Roeb, M.; Sattler, C. A review on solar thermal syngas production via redox pair-based water/carbon dioxide splitting thermochemical cycles. *Renew Sust Energ Rev.* **2015**, *42*, 254−285.
(93) Demont, A.; Abanades, S. High redox activity of Sr-substituted lanthanum Manganite perovskites for two-step thermochemical dissociation of CO2. *Rsc Advances* **2014**, *4* (97), 54885−54891.
(94) Scheffe, J. R.; Weibel, D.; Steinfeld, A. Lanthanum-Strontium-Manganese Perovskites as Redox Materials for Solar Thermochemical Splitting of H2O and CO2. *Energy Fuel* **2013**, *27* (8), 4250−4257.
(95) Demont, A.; Abanades, S.; Beche, E. Investigation of Perovskite Structures as Oxygen-Exchange Redox Materials for Hydrogen Production from Thermochemical Two-Step Water-Splitting Cycles. *J. Phys. Chem. C* **2014**, *118* (24), 12682−12692.
(96) Luciani, G.; Landi, G.; Aronne, A.; Di Benedetto, A. Partial substitution of B cation in La0.6Sr0.4MnO3 perovskites: A promising strategy to improve the redox properties useful for solar thermochemical water and carbon dioxide splitting. *Sol Energy* **2018**, *171*, 1−7.
(97) Orfila, M.; Linares, M.; Molina, R.; Botas, J. A.; Sanz, R.; Marugan, J. Perovskite materials for hydrogen production by thermochemical water splitting. *Int. J. Hydrogen Energy* **2016**, *41* (42), 19329−19338.
(98) Bork, A. H.; Povoden-Karadeniz, E.; Rupp, J. L. M. Modeling Thermochemical Solar-to-Fuel Conversion: CALPHAD for Thermo-

dynamic Assessment Studies of Perovskites, Exemplified for (La, Sr)MnO3. *Adv. Energy Mater.* **2017**, *7* (1), No. 1601086.
(99) Gager, E.; Frye, M.; McCord, D.; Scheffe, J.; Nino, J. C. Reticulated porous lanthanum strontium Manganite structures for solar thermochemical hydrogen production. *Int. J. Hydrogen Energ* **2022**, *47* (73), 31152−31164.
(100) Lee, K.; McCord, D. C.; Carrillo, R. J.; Guyll, B.; Scheffe, J. R. Improved Performance and Efficiency of Lanthanum-Strontium-Manganese Perovskites Undergoing Isothermal Redox Cycling under Controlled pH(2)O/pH(2). *Energ Fuel* **2020**, *34* (12), 16918−16926.
(101) Lee, K.; Scheffe, J. R. A Laser-Based Heating System for Studying the Morphological Stability of Porous Ceria and Porous La0.6Sr0.4MnO3 Perovskite during Solar Thermochemical Redox Cycling. *Energies* **2020**, *13* (22), 5935.
(102) Dey, S.; Naidu, B. S.; Govindaraj, A.; Rao, C. N. R. Noteworthy performance of La1-xCaxMnO3 perovskites in generating H-2 and CO by the thermochemical splitting of H2O and CO2. *Phys. Chem. Chem. Phys.* **2015**, *17* (1), 122−125.
(103) Dey, S.; Naidu, B. S.; Rao, C. N. R. Ln(0.5)A(0.5)MnO(3) (Ln = Lanthanide, A = Ca, Sr) Perovskites Exhibiting Remarkable Performance in the Thermochemical Generation of CO and H-2 from CO2 and H2O. *Chem.-Eur. J.* **2015**, *21* (19), 7077−7081.
(104) Wang, L. L.; Al-Mamun, M.; Liu, P. R.; Zhong, Y. L.; Wang, Y.; Yang, H. G.; Zhao, H. J. Enhanced Thermochemical H-2 Production on Ca-Doped Lanthanum Manganite Perovskites Through Optimizing the Dopant Level and Re-oxidation Temperature. *Acta Metall. Sin.-Engl. Lett.* **2018**, *31* (4), 431−439.
(105) Wang, L.; Al-Mamun, M.; Zhong, Y. L.; Liu, P.; Wang, Y.; Yang, H. G.; Zhao, H. Enhanced Thermochemical Water Splitting through Formation of Oxygen Vacancy in $La_{0.6}Sr_{0.4}BO_{3-\delta}$ (B = Cr, Mn, Fe, Co, and Ni) Perovskites. *ChemPlusChem.* **2018**, *83* (10), 924−928.
(106) Muhich, C. L.; Blaser, S.; Hoes, M. C.; Steinfeld, A. Comparing the solar-to-fuel energy conversion efficiency of ceria and perovskite based thermochemical redox cycles for splitting H2O and CO2. *Int. J. Hydrogen Energ* **2018**, *43* (41), 18814−18831.
(107) Motohashi, T.; Kimura, M.; Masubuchi, Y.; Kikkawa, S.; George, J.; Dronskowski, R. Significant Lanthanoid Substitution Effect on the Redox Reactivity of the Oxygen-Storage Material BaYMn2O5+delta. *Chem. Mater.* **2016**, *28* (12), 4409−4414.
(108) Barcellos, D. R.; Coury, F. G.; Emery, A.; Sanders, M.; Tong, J. H.; McDaniel, A.; Wolverton, C.; Kaufman, M.; O'Hayre, R. Phase Identification of the Layered Perovskite CexSr2-xMnO4 and Application for Solar Thermochemical Water Splitting. *Inorg. Chem.* **2019**, *58* (12), 7705−7714.
(109) Bergeson-Keller, A. M.; Sanders, M. D.; O'Hayre, R. P. Reduction Thermodynamics of Sr1-xCexMnO3 and CexSr2-xMnO4 Perovskites for Solar Thermochemical Hydrogen Production. *Energy Technol.* **2022**, *10* (1), No. 2100515.
(110) Wang, L. L.; Al-Mamun, M.; Zhong, Y. L.; Jiang, L. X.; Liu, P. R.; Wang, Y.; Yang, H. G.; Zhao, H. J. Ca2+ and Ga3+ doped LaMnO3 perovskite as a highly efficient and stable catalyst for two-step thermochemical water splitting. *Sustainable Energy & Fuels* **2017**, *1* (5), 1013−1017.
(111) Ignatowich, M. J.; Bork, A. H.; Davenport, T. C.; Rupp, J. L. M.; Yang, C. K.; Yamazaki, Y.; Haile, S. M. Impact of enhanced oxide reducibility on rates of solar-driven thermochemical fuel production. *MRS Commun.* **2017**, *7* (4), 873−878.
(112) Cooper, T.; Scheffe, J. R.; Galvez, M. E.; Jacot, R.; Patzke, G.; Steinfeld, A. Lanthanum Manganite Perovskites with Ca/Sr A-site and Al B-site Doping as Effective Oxygen Exchange Materials for Solar Thermochemical Fuel Production. *Energy Technology* **2015**, *3* (11), 1130−1142.
(113) McDaniel, A. H.; Miller, E. C.; Arifin, D.; Ambrosini, A.; Coker, E. N.; O'Hayre, R.; Chueh, W. C.; Tong, J. H. Sr- and Mn-doped LaAlO3-delta for solar thermochemical H-2 and CO production. *Energy Environ. Sci.* **2013**, *6* (8), 2424−2428.
(114) Deml, A. M.; Stevanović, V.; Holder, A. M.; Sanders, M.; O'Hayre, R.; Musgrave, C. B. Tunable Oxygen Vacancy Formation Energetics in the Complex Perovskite Oxide SrxLa1−xMnyAl1−yO3. *Chem. Mater.* **2014**, *26* (22), 6595−6602.
(115) Sanli, S. B.; Piskin, B. Effect of B-site Al substitution on hydrogen production of La0.4Sr0.6Mn1-xAlx (x1/40.4, 0.5 and 0.6) perovskite oxides. *Int. J. Hydrogen Energ* **2022**, *47* (45), 19411−19421.
(116) Ezbiri, M.; Becattini, V.; Hoes, M.; Michalsky, R.; Steinfeld, A. High Redox Capacity of Al-Doped La1-xSrxMnO3- Perovskites for Splitting CO2 and H2O at Mn-Enriched Surfaces. *ChemSusChem* **2017**, *10* (7), 1517−1525.
(117) Wang, L. L.; Al-Mamun, M.; Liu, P.; Wang, Y.; Yang, H. G.; Zhao, H. J. La1-xCaxMn1-yAlyO3 perovskites as efficient catalysts for two-step thermochemical water splitting in conjunction with exceptional hydrogen yields. *Chin. J. Catal.* **2017**, *38* (6), 1079−1086.
(118) Carrillo, R. J.; Hill, C. M.; Warren, K. J.; Scheffe, J. R. Oxygen Nonstoichiometry and Defect Equilibria of Yttrium Manganite Perovskites with Strontium A-Site and Aluminum B-Site Doping. *J. Phys. Chem. C* **2020**, *124* (8), 4448−4458.
(119) Chen, Z.; Jiang, Q.; Cheng, F.; Tong, J.; Yang, M.; Jiang, Z.; Li, C. Sr- and Co-doped $LaGaO_{3-\delta}$ with high O2 and H2 yields in solar thermochemical water splitting. *Journal of Materials Chemistry A* **2019**, *7* (11), 6099−6112.
(120) Trindell, J. A.; McDaniel, A. H.; Ogitsu, T.; Ambrosini, A.; Sugar, J. D. Probing Electronic and Structural Transformations during Thermal Reduction of the Promising Water Splitting Perovskite BaCe0.25Mn0.75O3. *Chem. Mater.* **2022**, *34* (17), 7712−7720.
(121) Strange, N. A.; Park, J. E.; Goyal, A.; Bell, R. T.; Trindell, J. A.; Sugar, J. D.; Stone, K. H.; Coker, E. N.; Lany, S.; Shulda, S.; Ginley, D. S. Formation of 6H-Ba(3)Ce(0.75)Mn(2.25)O(9)during Thermochemical Reduction of 12R-Ba4CeMn3O12: Identification of a Polytype in the Ba(Ce,Mn)O-3 Family. *Inorg. Chem.* **2022**, *61* (16), 6128−6137.
(122) Roychoudhury, S.; Shulda, S.; Goyal, A.; Bell, R. T.; Sainio, S.; Strange, N. A.; Park, J. E.; Coker, E. N.; Lany, S.; Ginley, D. S.; Prendergast, D. Investigating the Electronic Structure of Prospective Water-Splitting Oxide BaCe0.25Mn0.75O3-delta before and after Thermal Reduction. *Chem. Mater.* **2023**, *35* (5), 1935−1947.
(123) Heo, S. J.; Sanders, M.; O'Hayre, R.; Zakutayev, A. Double-Site Substitution of Ce into (Ba, Sr)MnO3 Perovskites for Solar Thermochemical Hydrogen Production. *Acs Energy Letters* **2021**, *6* (9), 3037−3043.
(124) Sai Gautam, G.; Stechel, E. B.; Carter, E. A. Exploring Ca−Ce−M−O (M = 3d Transition Metal) Oxide Perovskites for Solar Thermochemical Applications. *Chem. Mater.* **2020**, *32* (23), 9964−9982.
(125) Wexler, R. B.; Gautam, G. S.; Bell, R. T.; Shulda, S.; Strange, N. A.; Trindell, J. A.; Sugar, J. D.; Nygren, E.; Sainio, S.; McDaniel, A. H.; Ginley, D.; Carter, E. A.; Stechel, E. B. Multiple and nonlocal cation redox in Ca-Ce-Ti-Mn oxide perovskites for solar thermochemical applications. *Energy Environ. Sci.* **2023**, *16* (6), 2550−2560.
(126) Dey, S.; Naidu, B. S.; Rao, C. N. R. Beneficial effects of substituting trivalent ions in the B-site of La(0.5)Sr(0.5)Mn(1-x)A(x)O(3) (A = Al, Ga, Sc) on the thermochemical generation of CO and H-2 from CO2 and H2O. *Dalton Trans* **2016**, *45* (6), 2430−2435.
(127) Gokon, N.; Hara, K.; Ito, N.; Sawaguri, H.; Bellan, S.; Kodama, T.; Cho, H. S. Thermochemical H2O Splitting Using LaSrMnCrO3 of Perovskite Oxides for Solar Hydrogen Production. *AIP Conf. Proc.* **2020**, *2303*, No. 170007.
(128) Yigiter, I. E.; Piskin, B. Investigation into Ca-Doped LaMnCoO3 Perovskite Oxides for Thermochemical Water Splitting. *Jom* **2022**, *74* (12), 4682−4694.
(129) Chen, Z.; Jiang, Q.; Tong, J.; Yang, M.; Jiang, Z.; Li, C. Enhancement effects of dopants and SiO_2 support on mixed metal ferrites based two-step thermochemical water splitting. *Sol. Energy* **2017**, *144*, 643−659.

https://doi.org/10.1021/acscatal.4c03357
ACS Catal. 2024, 14, 14974−15013

(130) Naik, J. M.; Bulfin, B.; Triana, C. A.; Stoian, D. C.; Patzke, G. R. Cation-Deficient Ce-Substituted Perovskite Oxides with Dual-Redox Active Sites for Thermochemical Applications. *Acs Appl. Mater. Interfaces* **2023**, *15* (1), 806−817.
(131) Haeussler, A.; Abanades, S.; Julbe, A.; Jouannaux, J.; Cartoixa, B. Two-step CO2 and H2O splitting using perovskite-coated ceria foam for enhanced green fuel production in a porous volumetric solar reactor. *Journal of Co2 Utilization* **2020**, *41*, No. 101257.
(132) Haeussler, A.; Julbe, A.; Abanades, S. Investigation of reactive perovskite materials for solar fuel production via two-step redox cycles: Thermochemical activity, thermodynamic properties and reduction kinetics. *Mater. Chem. Phys.* **2022**, *276*, No. 125358.
(133) Nalbandian, L.; Evdou, A.; Zaspalis, V. La1−xSrxMO3 (M = Mn, Fe) perovskites as materials for thermochemical hydrogen production in conventional and membrane reactors. *Int. J. Hydrogen Energ* **2009**, *34* (17), 7162−7172.
(134) Jin, J. H.; Fu, M. K.; Wang, L.; Ma, T. Z.; Li, X.; Jin, F.; Lu, Y. W. Water-splitting mechanism analysis of Sr/Ca doped LaFeO3 towards commercial efficiency of solar thermochemical H-2 production. *Int. J. Hydrogen Energ* **2021**, *46* (2), 1634−1641.
(135) Park, J.; Xu, B. Y.; Pan, J.; Zhang, D. W.; Lany, S.; Liu, X. B.; Luo, J.; Qi, Y. Accurate prediction of oxygen vacancy concentration with disordered A-site cations in high-entropy perovskite oxides. *npj Comput. Mater.* **2023**, *9*, 29.
(136) Batuk, M.; Vandemeulebroucke, D.; Ceretti, M.; Paulus, W.; Hadermann, J. Topotactic redox cycling in SrFeO2.5+delta explored by 3D electron diffraction in different gas atmospheres. *Journal of Materials Chemistry A* **2022**, *11* (1), 213−220.
(137) Ngoensawat, A.; Tongnan, V.; Laosiripojana, N.; Kim-Lohsoontorn, P.; Hartley, U. W. Effect of La and Gd substitution in BaFeO3-delta perovskite structure on its catalytic performance for thermochemical water splitting. *Catal. Commun.* **2020**, *135*, No. 105901.
(138) Perez, A.; Orfila, M.; Linares, M.; Sanz, R.; Marugan, J.; Molina, R.; Botas, J. A. Hydrogen production by thermochemical water splitting with La0.8Al0.2MeO3-delta (Me= Fe, Co, Ni and Cu) perovskites prepared under controlled pH. *Catal. Today* **2022**, *390*, 22−33.
(139) Fu, M. K.; Ma, H. T.; Li, X.; Xu, H. J. Mechanism and thermodynamic study of solar H-2 production on LaFeO3 defected surface: Effect of H2O to H-2 conversion ratio and kinetics on optimization of energy conversion efficiency. *J. Clean Prod.* **2020**, *268*, No. 122293.
(140) Jiang, Q. Q.; Chen, Z. P.; Tong, J. H.; Yang, M.; Jiang, Z. X.; Li, C. Catalytic Function of IrOx in the Two-Step Thermochemical CO2-Splitting Reaction at High Temperatures. *ACS Catal.* **2016**, *6* (2), 1172−1180.
(141) Chen, S.; Cheng, H. W.; Liu, Y. B.; Xiong, X. L.; Sun, Q. C.; Xu, Q.; Lu, X. G.; Li, S. G. Water interaction with B-site (B = Al, Zr, Nb, and W) doped SrFeO3-delta-based perovskite surfaces for thermochemical water splitting applications. *Phys. Chem. Chem. Phys.* **2022**, *24* (47), 28975−28983.
(142) Wang, L.; Al-Mamun, M.; Liu, P.; Wang, Y.; Yang, H. G.; Zhao, H. Notable hydrogen production on $La_xCa_{1-x}CoO_3$ perovskites via two-step thermochemical water splitting. *J. Mater. Sci.* **2018**, *53* (9), 6796−6806.
(143) Orfila, M.; Linares, M.; Perez, A.; Barras-Garcia, I.; Molina, R.; Marugan, J.; Botas, J. A.; Sanz, R. Experimental evaluation and energy analysis of a two-step water splitting thermochemical cycle for solar hydrogen production based on La0.8Sr0.2CoO3-d perovskite. *Int. J. Hydrogen Energ* **2022**, *47* (97), 41209−41222.
(144) Azcondo, M. T.; Orfila, M.; Marugan, J.; Sanz, R.; Munoz-Noval, A.; Salas-Colera, E.; Ritter, C.; Garcia-Alvarado, F.; Amador, U. Novel Perovskite Materials for Thermal Water Splitting at Moderate Temperature. *ChemSusChem* **2019**, *12* (17), 4029−4037.
(145) Bork, A. H.; Kubicek, M.; Struzik, M.; Rupp, J. L. M. Perovskite La0.6Sr0.4Cr1-xCoxO3-delta solid solutions for solar-thermochemical fuel production: strategies to lower the operation temperature. *Journal of Materials Chemistry A* **2015**, *3* (30), 15546−15557.
(146) Park, J. E.; Bare, Z. J. L.; Morelock, R. J.; Rodriguez, M. A.; Ambrosini, A.; Musgrave, C. B.; McDaniel, A. H.; Coker, E. N. Computationally Accelerated Discovery and Experimental Demonstration of Gd0.5La0.5Co0.5Fe0.5O3 for Solar Thermochemical Hydrogen Production. *Front. Energy Res.* **2021**, *9*, 750600.
(147) Cong, J.; Ma, T. Z.; Chang, Z. S.; Akhatov, J. S.; Fu, M. K.; Li, X. Coupling of the water-splitting mechanism and doping-mixture method to design a novel Cr-perovskite for rapid and efficient solar thermochemical H-2 production. *Inorganic Chemistry Frontiers* **2022**, *9* (22), 5714−5724.
(148) Rost, C. M.; Sachet, E.; Borman, T.; Moballegh, A.; Dickey, E. C.; Hou, D.; Jones, J. L.; Curtarolo, S.; Maria, J. P. Entropy-stabilized oxides. *Nat. Commun.* **2015**, *6*, 8485.
(149) Le Gal, A.; Valles, M.; Julbe, A.; Abanades, S. Thermochemical Properties of High Entropy Oxides Used as Redox-Active Materials in Two-Step Solar Fuel Production Cycles. *Catalysts* **2022**, *12* (10), 1116.
(150) Wright, A. J.; Luo, J. A step forward from high-entropy ceramics to compositionally complex ceramics: a new perspective. *J. Mater. Sci.* **2020**, *55* (23), 9812−9827.
(151) Wright, A. J.; Wang, Q. Y.; Huang, C. Y.; Nieto, A.; Chen, R. K.; Luo, J. From high-entropy ceramics to compositionally-complex ceramics: A case study of fluorite oxides. *J. Eur. Ceram Soc.* **2020**, *40* (54), 2120−2129.
(152) Liu, C. J.; Zhang, D. W.; Li, W.; Trindell, J. A.; King, K. A.; Bishop, S. R.; Sugar, J. D.; McDaniel, A. H.; Smith, A. I.; Salinas, P. A.; Coker, E. N.; Clauser, A. L.; Velayutham, M.; Neuefeind, J. C.; Yang, J. J.; De Santiago, H. A.; Ma, L.; Wang, Y.; Wang, Q.; Li, W. Y.; Wang, Q. S.; Li, Q. Y.; Tian, H. C.; Ngan Tran, H. N.; Li, X. M.; Robinson, B.; Deibel, A. M.; Collins, G.; Thieu, N. A.; Hu, J. L.; Khramtsov, V. V.; Luo, J.; Liu, X. B. Manganese-based A-site high-entropy perovskite oxide for solar thermochemical hydrogen production. *J. Mater. Chem. A* **2024**, *12* (7), 3910−3922.
(153) Krenzke, P. T.; Davidson, J. H. On the Efficiency of Solar H2 and CO Production via the Thermochemical Cerium Oxide Redox Cycle: The Option of Inert-Swept Reduction. *Energ Fuel* **2015**, *29* (2), 1045−1054.
(154) Evdou, A.; Nalbandian, L.; Zaspalis, V. Perovskite membrane reactor for continuous and isothermal redox hydrogen production from the dissociation of water (vol 325, pg 704, 2008). *J. Membr. Sci.* **2009**, *334* (1−2), 148−148.
(155) Jiang, H. Q.; Wang, H. H.; Werth, S.; Schiestel, T.; Caro, J. Simultaneous Production of Hydrogen and Synthesis Gas by Combining Water Splitting with Partial Oxidation of Methane in a Hollow-Fiber Membrane Reactor. *Angew. Chem. Int. Ed* **2008**, *47* (48), 9341−9344.
(156) Marxer, D.; Furler, P.; Scheffe, J.; Geerlings, H.; Falter, C.; Batteiger, V.; Sizmann, A.; Steinfeld, A. Demonstration of the Entire Production Chain to Renewable Kerosene via Solar Thermochemical Splitting of H2O and CO2. *Energ Fuel* **2015**, *29* (5), 3241−3250.
(157) Furler, P.; Scheffe, J.; Gorbar, M.; Moes, L.; Vogt, U.; Steinfeld, A. Solar thermochemical CO2 splitting utilizing a reticulated porous ceria redox system. *Abstr. Pap. Am. Chem. Soc.* **2012**, *26* (11), 7051−7059.
(158) Liu, C.; Zhang, D.; Li, W.; Trindell, J. A.; King, K. A.; Bishop, S. R.; Sugar, J. D.; McDaniel, A. H.; Smith, A. I.; Salinas, P. A.; et al. Manganese-based A-site high-entropy perovskite oxide for solar thermochemical hydrogen production. *J. Mater. Chem. A* **2024**, *12*, 3910−3922.
(159) Das, T.; Nicholas, J. D.; Qi, Y. Long-range charge transfer and oxygen vacancy interactions in strontium ferrite. *Journal of Materials Chemistry A* **2017**, *5* (9), 4493−4506.
(160) Dudarev, S. L.; Botton, G. A.; Savrasov, S. Y.; Humphreys, C. J.; Sutton, A. P. Electron-energy-loss spectra and the structural stability of nickel oxide: An LSDA+U study. *Phys. Rev. B* **1998**, *57* (3), 1505−1509.

https://doi.org/10.1021/acscatal.4c03357
ACS Catal. 2024, 14, 14974−15013

(161) Mattsson, A. E.; Armiento, R.; Schultz, P. A.; Mattsson, T. R. Nonequivalence of the generalized gradient approximations PBE and PW91. *Phys. Rev. B* **2006**, *73* (19), No. 195123.
(162) Sun, J. W.; Ruzsinszky, A.; Perdew, J. P. Strongly Constrained and Appropriately Normed Semilocal Density Functional. *Phys. Rev. Lett.* **2015**, *115* (3), No. 036402.
(163) Jia, T.; Zeng, Z.; Zhang, X.; Ohodnicki, P.; Chorpening, B.; Hackett, G.; Lekse, J.; Duan, Y. The influence of oxygen vacancy on the electronic and optical properties of ABO3-delta (A = La, Sr, B = Fe, Co) perovskites. *Phys. Chem. Chem. Phys.* **2019**, *21* (36), 20454−20462.
(164) Ghose, K. K.; Bayon, A.; Page, A. J. Electronic Structure and High-Temperature Thermochemistry of Oxygen-Deficient BaMO3 (M = Ti − Cu) Perovskites. *J. Phys. Chem. C* **2020**, *124* (49), 27055−27063.
(165) Curnan, M. T.; Kitchin, J. R. Effects of Concentration, Crystal Structure, Magnetism, and Electronic Structure Method on First-Principles Oxygen Vacancy Formation Energy Trends in Perovskites. *J. Phys. Chem. C* **2014**, *118* (49), 28776−28790.
(166) Emery, A. A.; Saal, J. E.; Kirklin, S.; Hegde, V. I.; Wolverton, C. High-Throughput Computational Screening of Perovskites for Thermochemical Water Splitting Applications. *Chem. Mater.* **2016**, *28* (16), 5621−5634.
(167) Deml, A. M.; Holder, A. M.; O'Hayre, R. P.; Musgrave, C. B.; Steyanović, V. Intrinsic Material Properties Dictating Oxygen Vacancy Formation Energetics in Metal Oxides. *J. Phys. Chem. Lett.* **2015**, *6* (10), 1948−1953.
(168) Wexler, R. B.; Gautam, G. S.; Stechel, E. B.; Carter, E. A. Factors Governing Oxygen Vacancy Formation in Oxide Perovskites. *J. Am. Chem. Soc.* **2021**, *143* (33), 13212−13227.
(169) Baldassarri, B.; He, J.; Qian, X.; Mastronardo, E.; Griesemer, S.; Haile, S. M.; Wolverton, C. J. P. R. M. *Accuracy of DFT computed oxygen-vacancy formation energies and high-throughput search of solar thermochemical water-splitting compounds* **2023**, *7* (6), No. 065403.
(170) Jia, T.; Popczun, E. J.; Lekse, J. W.; Duan, Y. Effective Ca2+-doping in Sr1-xCaxFeO3-δ oxygen carriers for chemical looping air separation: A theoretical and experimental investigation. *Appl. Energ* **2021**, *281*, No. 116040.
(171) Merkle, R.; Mastrikov, Y. A.; Kotomin, E. A.; Kuklja, M. M.; Maier, J. First Principles Calculations of Oxygen Vacancy Formation and Migration in Ba1−xSrxCo1−yFeyO3−δPerovskites. *J. Electrochem. Soc.* **2011**, *159* (2), B219−B226.
(172) Maiti, D.; Daza, Y. A.; Yung, M. M.; Kuhn, J. N.; Bhethanabotla, V. R. Oxygen vacancy formation characteristics in the bulk and across different surface terminations of La(1−x)SrxFe(1−y)CoyO(3−δ) perovskite oxides for CO2 conversion. *Journal of Materials Chemistry A* **2016**, *4* (14), 5137−5148.
(173) Jin, F.; Xu, C.; Yu, H.; Xia, X.; Ye, F.; Li, X.; Du, X.; Yang, Y. CaCo0.05Mn0.95O3-delta: A Promising Perovskite Solid Solution for Solar Thermochemical Energy Storage. *ACS Appl. Mater. Interfaces* **2021**, *13* (3), 3856−3866.
(174) Das, T.; Nicholas, J. D.; Qi, Y. Polaron size and shape effects on oxygen vacancy interactions in lanthanum strontium ferrite. *Journal of Materials Chemistry A* **2017**, *5* (47), 25031−25043.
(175) Vieten, J.; Bulfin, B.; Huck, P.; Horton, M.; Guban, D.; Zhu, L. Y.; Lu, Y. J.; Persson, K. A.; Roeb, M.; Sattler, C. Materials design of perovskite solid solutions for thermochemical applications. *Energy Environ. Sci.* **2019**, *12* (4), 1369−1384.
(176) Wang, X. J.; Gao, Y. F.; Krzystowczyk, E.; Iftikhar, S.; Dou, J.; Cai, R. X.; Wang, H. Y.; Ruan, C. Y.; Ye, S.; Li, F. X. High-throughput oxygen chemical potential engineering of perovskite oxides for chemical looping applications. *Energy Environ. Sci.* **2022**, *15* (4), 1512−1528.
(177) Ritzmann, A. M.; Pavone, M.; Muñoz-García, A. B.; Keith, J. A.; Carter, E. A. Ab initio DFT+U analysis of oxygen transport in LaCoO3: the effect of Co3+ magnetic states. *J. Mater. Chem. A* **2014**, *2* (21), 8060−8074.
(178) Mizusaki, J.; Mima, Y.; Yamauchi, S.; Fueki, K.; Tagawa, H. Nonstoichiometry of the perovskite-type oxides La1−xSrxCoO3−δ. *J. Solid State Chem.* **1989**, *80* (1), 102−111.
(179) Qian, X.; He, J.; Mastronardo, E.; Baldassarri, B.; Wolverton, C.; Haile, S. M. Favorable Redox Thermodynamics of SrTi0.5Mn0.5O3−δ in Solar Thermochemical Water Splitting. *Chem. Mater.* **2020**, *32* (21), 9335−9346.
(180) Ermanoski, I.; Miller, J. E.; Allendorf, M. D. Efficiency maximization in solar-thermochemical fuel production: challenging the concept of isothermal water splitting. *Phys. Chem. Chem. Phys.* **2014**, *16* (18), 8418−27.
(181) Bulfin, B.; Call, F.; Lange, M.; Lübben, O.; Sattler, C.; Pitz-Paal, R.; Shvets, I. V. Thermodynamics of CeO_2 Thermochemical Fuel Production. *Energy Fuels* **2015**, *29* (2), 1001−1009.
(182) Zhai, S.; Rojas, J.; Ahlborg, N.; Lim, K.; Toney, M. F.; Jin, H. Y.; Chueh, W. C.; Majumdar, A. The use of poly-cation oxides to lower the temperature of two-step thermochemical water splitting. *Energy Environ. Sci.* **2018**, *11* (8), 2172−2178.
(183) Gild, J.; Samiee, M.; Braun, J. L.; Harrington, T.; Vega, H.; Hopkins, P. E.; Vecchio, K.; Luo, J. High-entropy fluorite oxides. *J. Eur. Ceram Soc.* **2018**, *38* (10), 3578−3584.
(184) Wright, A. J.; Wang, Q. Y.; Hu, C. Z.; Yeh, Y. T.; Chen, R. K.; Luo, J. Single-phase duodenary high-entropy fluorite/pyrochlore oxides with an order-disorder transition. *Acta Mater.* **2021**, *211*, No. 116858.
(185) Wright, A. J.; Wang, Q. Y.; Yeh, Y. T.; Zhang, D. W.; Everett, M.; Neuefeind, J.; Chen, R. K.; Luo, J. Short-range order and origin of the low thermal conductivity in compositionally complex rare-earth niobates and tantalates. *Acta Mater.* **2022**, *235*, No. 118056.
(186) Qin, M. D.; Vega, H.; Zhang, D. W.; Adapa, S.; Wright, A. J.; Chen, R. K.; Luo, J. 21-Component compositionally complex ceramics: Discovery of ultrahigh-entropy weberite and fergusonite phases and a pyrochlore-weberite transition. *J. Adv. Ceram.* **2022**, *11* (4), 641−655.
(187) Zhang, D. W.; Chen, Y.; Vega, H.; Feng, T. S.; Yu, D. J.; Everett, M.; Neuefeind, J.; An, K.; Chen, R. K.; Luo, J. Long- and short-range orders in 10-component compositionally complex ceramics. *Adv. Powder Mater.* **2023**, *2* (2), No. 100098.

https://doi.org/10.1021/acscatal.4c03357
ACS Catal. 2024, 14, 14974−15013